University of California
Santa Barbara

Quantum Defects from First Principles

A dissertation submitted in partial satisfaction
of the requirements for the degree

Doctor of Philosophy
in
Physics

by

Mark E. Turiansky

Committee in charge:

Professor Chris G. Van de Walle, Co-Chair
Professor Cenke Xu, Co-Chair
Professor Ania C. Bleszynski Jayich

June 2022

The Dissertation of Mark E. Turiansky is approved.

Professor Ania C. Bleszynski Jayich

Professor Cenke Xu, Committee Co-Chair

Professor Chris G. Van de Walle, Committee Co-Chair

June 2022

Quantum Defects from First Principles

To my parents and my cat, Gideon.

Acknowledgements

As I look back on the last five years, there are a number of people who have influenced my development as both a scientist and a person. Without their contributions, this work would not be possible, and for that, I am deeply grateful.

First is my advisor, Prof. Chris G. Van de Walle. Chris is an inspiring scientist and a wonderful mentor. I remember how fearful I was when I first joined the group: I was surrounded by fiercely intelligent people who exhibited expertise worthy of envy. It is with Chris' coaching that I can confidently say that I have overcome that fear and can join the rank of experts trained under his watch. Chris has taught me to think critically about problems, to always ask questions, and to strive for excellence. He taught me the value of clear communication and gave me many opportunities to grow as an academic. With his guidance, I have been able to delve deeply into a wide variety of research problems and truly *understand* the microscopic mechanisms behind them. I would not be the scientist I am today without Chris, and I will carry what I have learned with me in my future endeavors.

I would also like to acknowledge the other members of my advising committee, Prof. Ania C. Bleszynski Jayich and Prof. Cenke Xu. Their questions and comments have been incredibly insightful and have helped to guide me along in my studies. I greatly appreciate their contributions to my growth as a scientist.

My Ph.D. would not be possible without the support of funding agencies. I acknowledge support from the National Science Foundation through the MRSEC Seed Program DMR-1720256 and "Enabling Quantum Leap: Convergent Accelerated Discovery Foundries for Quantum Materials Science, Engineering and Information" (Q-AMASE-i) DMR-1906325. In particular, my Fellowship from the Quantum Foundry has enabled me to explore the rich field of quantum information science. My work

would not be possible without the computational resources provided by the CNSI Center for Scientific Computing (CNS-1725797), NERSC (DE-AC02-05CH11231), and XSEDE (ACI-1548562).

It has been a wonderful privilege to work with Prof. Audrius Alkauskas. Audrius is a world-class researcher, who has been like a second advisor to me. I always look forward to Audrius' visits to UCSB as they give me an opportunity to pick Audrius' mind and hear some of his insights. I am always in awe of Audrius' extensive knowledge and attention to detail.

Professor Xie Zhang is perhaps my most productive collaborator but, more importantly, an excellent friend. I miss the many conversations we shared while officemates, but I am delighted to see you thriving as a professor. I look forward to many more collaborations.

I would also like to thank the other VdW group members, both current and former, who have contributed to my success. Dr. Darshana Wickramaratne was a wonderful mentor during our (albeit short) overlap at UCSB. He and Dr. Jimmy-Xuan Shen helped me to build a strong foundational knowledge during my first year. I am very thankful to have interacted with Prof. Cyrus E. Dreyer, Dr. John L. Lyons, Dr. Fangzhou Zhao, Dr. Sai Mu, Dr. Mengen Wang, Yubi Chen, Dr. Joel Varley, Prof. Emmanouil Kioupakis, Prof. Hartwin Peelaers, Dr. Andrew J. E. Rowberg, Dr. Nicholas Adamski, Dr. Michael W. Swift, Prof. Wennie Wang, Dr. Yongjin Shin, Siavash Karbasizadeh, Dr. Baiyu Zhang, Dr. Stephanie Mack, Dr. Leigh Weston, Dr. Zhen Zhu, Dr. Youngho Kang, Prof. Santosh KC, Azzedin Jackson, and Haochen Wang. I would also like to acknowledge the various visitors to the VdW group, Dr. Ymir Kalmann Frodason, Dr. Kamil Czelej, and Dr. Christopher Broderick.

I am grateful to have collaborated with Prof. Lee C. Bassett and Raj N. Patel: your

experiments have helped to inspire my work, and I appreciate the care with which you approach your measurements. I would also like to acknowledge Prof. Georg Kresse and Manuel Engel; without their coding skills and expertise, much of this work would not be possible.

I am forever indebted to my many friends at UCSB, who helped make my time more enjoyable. In particular, I have greatly enjoyed spending countless hours in the mountains with my climbing partners, Josh Straub and Remi Boros. Thank you for helping me stay sane through the stresses of graduate school. I also appreciate enriching interactions with the "stonks crew", Will Schultz and Aaron Kennon.

Last but not least, thank you to my family. I am extremely grateful for my parents, Lois Turiansky and Eugene Turiansky, who supported me and pushed me to grow as an individual; I wouldn't be the person that I am today without your help. I greatly appreciate my step-parents, my brother, grandparents, aunts, uncles, and cousins, who all helped me to feel loved and supported. And thank you to my cat, Gideon, the best cat that I could have asked for.

Curriculum Vitæ
Mark E. Turiansky

Education

Jun 2022	Ph.D. in Physics (Expected), *University of California, Santa Barbara.*
Sep 2020	M.A. in Physics, *University of California, Santa Barbara.*
May 2017	B.S. in Computer Science, *University of Florida.*
May 2017	B.S. in Physics, *University of Florida.*

Honors and Awards

Mar 2022	Dow Materials Institute / Materials Research Laboratory Travel Award
Mar 2022	UCSB Academic Senate Doctoral Student Travel Grant
Mar 2022	APS Division of Materials Physics Ovshinsky Student Travel Award
Mar 2021	APS Division of Computational Physics Travel Award
Mar 2020	Dow Materials Institute / Materials Research Laboratory Travel Award
Jan 2020	UCSB Quantum Foundry Graduate Fellowship
Mar 2019	APS Division of MAterials Physics Ovshinsky Student Travel Award Honorable Mention
Mar 2019	Dow Materials Institute / Materials Research Laboratory Travel Award
Sep 2017	UF Center for Condensed Matter Sciences Fellowship

Publications

1. X. Zhang, **M. E. Turiansky**, J.-X. Shen, and C. G. Van de Walle, "Defect Tolerance in Halide Perovskites: A First-Principles Perspective", J. Appl. Phys. **131**, 090901 (2022). [doi: 10.1063/5.0083686]

2. **M. E. Turiansky**, D. Wickramaratne, J. L. Lyons, and C. G. Van de Walle, "Prospects for *n*-type Conductivity in Cubic Boron Nitride", Appl. Phys. Lett. **119**, 162105 (2021). [doi: 10.1063/5.0069970]
3. X. Zhang, **M. E. Turiansky**, and C. G. Van de Walle, "All-Inorganic Halide Perovskites as Candidates for Efficient Solar Cells", Cell Rep. Phys. Sci. **2**, 100604 (2021). [doi: 10.1016/j.xcrp.2021.100604]
4. **M. E. Turiansky**, A. Alkauskas, M. Engel, G. Kresse, D. Wickramaratne, J.-X. Shen, C. E. Dreyer, and C. G. Van de Walle, "Nonrad: Computing Nonradiative Capture Coefficients from First Principles", Comput. Phys. Commun. **267**, 108056 (2021). [doi: 10.1016/j.cpc.2021.108056]
5. X. Zhang, J.-X. Shen, **M. E. Turiansky**, and C. G. Van de Walle, "Minimizing Hydrogen Vacancies to Enable Highly Efficient Hybrid Perovskites", Nat. Mater. **20**, 971 (2021). [doi: 10.1038/s41563-021-00986-5]
6. J.-X. Shen, **M. E. Turiansky**, D. Wickramaratne, and C. G. Van de Walle, "Thermodynamics of Boron Incorporation in BGaN", Phys. Rev. Materials **5**, L030401 (2021). [doi: 10.1103/PhysRevMaterials.5.L030401]
7. **M. E. Turiansky** and C. G. Van de Walle, "Boron Dangling Bonds in a Monolayer of Hexagonal Boron Nitride", J. Appl. Phys. **129**, 064301 (2021). [doi: 10.1063/5.0040780]
8. **M. E. Turiansky** and C. G. Van de Walle, "Impact of Dangling Bonds on Properties of h-BN", 2D Mater. **8**, 024002 (2021). [doi: 10.1088/2053-1583/abe4bb]
9. **M. E. Turiansky**, A. Alkauskas, and C. G. Van de Walle, "Spinning up Quantum Defects in 2D Materials", Nat. Mater. **19**, 487 (2020). [doi: 10.1038/s41563-020-0668-x]
10. X. Zhang, **M. E. Turiansky**, J.-X. Shen, and C. G. Van de Walle, "Iodine Interstitials as a Cause of Nonradiative Recombination in Hybrid Perovskites", Phys. Rev. B **101**, 140101 (2020). [doi: 10.1103/PhysRevB.101.140101]
11. X. Zhang, **M. E. Turiansky**, and C. G. Van de Walle, "Correctly Assessing Defect Tolerance in Halide Perovskites", J. Phys. Chem. C **124**, 6022 (2020). [doi: 10.1021/acs.jpcc.0c01324]
12. X. Zhang, J.-X. Shen, **M. E. Turiansky**, and C. G. Van de Walle, "Hidden Role of Bi Incorporation in Nonradiative Recombination in Methylammonium Lead Iodide", J. Mater. Chem. A **8**, 12964 (2020). [doi: 10.1039/D0TA04968A]
13. **M. E. Turiansky**, A. Alkauskas, L. C. Bassett, and C. G. Van de Walle, "Dangling Bonds in Hexagonal Boron Nitride as Single-Photon Emitters", Phys. Rev. Lett. **123**, 127401 (2019). [doi: 10.1103/PhysRevLett.123.127401]

14. **M. E. Turiansky**, J.-X. Shen, D. Wickramaratne, and C. G. Van de Walle, "First-Principles Study of Bandgap Bowing in BGaN Alloys", J. Appl. Phys. **126**, 095706 (2019). [doi: 10.1063/1.5111414]
15. R. K. Das, S. V. Vasilyeva, R. M. Pulido, I. Pucher, M. E. Turiansky, and A. G. Rinzler, "A Pt-free, activated carbon nanotube cathode, PEM Water Splitting Electrolyzer", Meet. Abstr. **MA2016-01**, 1423 (2016). [doi: 10.1149/MA2016-01/29/1423]

Unpublished

1. R. N. Patel, D. A. Hopper, J. A. Gusdorff, **M. E. Turiansky**, T.-Y. Huang, R. E. K. Fishman, B. Porat, C. G. Van de Walle, and L. C. Bassett, "Probing the Optical Dynamics of Quantum Emitters in Hexagonal Boron Nitride", arXiv:2201.08881 (2022). [doi: 10.48550/arXiv.2201.08881]
2. Y. Chen, **M. E. Turiansky**, and C. G. Van de Walle, "First-Principles Study of Quantum Defect Candidates in Beryllium Oxide", *in preparation*.
3. S. Mu, **M. E. Turiansky**, M. W. Swift, and C. G. Van de Walle, "Shallow Donors in β-Ga_2O_3 from First Principles", *in preparation*.
4. F. Zhao, **M. E. Turiansky**, and C. G. Van de Walle, "Impurity Auger from First Principles", *in preparation*.
5. **M. E. Turiansky**, A. Alkauskas, and C. G. Van de Walle, "The Sommerfeld Parameter in One and Two Dimensions", *in preparation*.
6. **M. E. Turiansky** and C. G. Van de Walle, "Quantum Defects and Photoluminescent Centers in Cubic Boron Nitride", *in preparation*.
7. **M. E. Turiansky**, X. Zhang, and C. G. Van de Walle, "Proper Treatment and Pitfalls of Anharmonic Nonradiative Rate Evaluations", *in preparation*.
8. **M. E. Turiansky**, X. Zhang, and C. G. Van de Walle, "Developing Intuition for Nonradiative Capture in the Presence of Multiple Transition Levels", *in preparation*.

Invited Talks

Apr 2022	Stony Brook Condensed Matter Seminar, Online "Defects in boron nitride from first principles"
Jul 2021	31^{st} International Conference on Defects in Semiconductors, Online "Single-photon emitters in hexagonal boron nitride"
Mar 2021	American Physical Society March Meeting, Online "Boron dangling bonds as single photon emitters in hexagonal boron nitride"

Contributed Talks

Mar 2022	American Physical Society March Meeting, Chicago, IL "Prospects for *n*-type conductivity in cubic boron nitride"
Mar 2021	American Physical Society March Meeting, Online "Computing nonradiative capture coefficients from first principles"
Feb 2021	UCSB Nitrides Seminar, Santa Barbara, CA "Understanding boron nitride with computational techniques"
Nov 2020	Materials Research Society Spring/Fall Meeting, Online "Dangling bonds in hexagonal boron nitride for quantum information science"
Mar 2020	American Physical Society March Meeting, Denver, CO "Boron dangling bonds as single photon emitters in hexagonal boron nitride"
Jul 2019	30^{th} International Conference on Defects in Semiconductors, Seattle, WA "First-principles calculations of defects and single-photon emitters in hexagonal boron nitride"
Mar 2019	American Physical Society March Meeting, Boston, MA "Incorporation of boron in gallium nitride"
Jul 2018	UCSB Materials Research Science and Engineering Center Summer Symposium, Santa Barbara, CA "Point defects in boron nitride for quantum information science"

Conference Posters

May 2022	Materials Research Outreach Program Symposium, Santa Barbara, CA "Quantum defects and doping in boron nitride polymorphs"
Jan 2021	Materials Research Outreach Program Symposium, Santa Barbara, CA "Exploring properties of boron nitride for quantum information science"
Jan 2020	Materials Research Outreach Program Symposium, Santa Barbara, CA "Boron dangling bonds in hexagonal boron nitride for quantum information science"
Jan 2019	Materials Research Outreach Program Symposium, Santa Barbara, CA

	"Point defects in hexagonal boron nitride for quantum information science"
Nov 2018	Solid State Lighting & Energy Electronics Center Review, Santa Barbara, CA "Energetics and electronic structure of BGaN alloys"
Aug 2018	Gordon Research Conference: Defects in Semiconductors, New London, NH "Incorporation of boron in gallium nitride"

Abstract

Quantum Defects from First Principles

by

Mark E. Turiansky

Point defects in semiconductors or insulators are a promising platform to realize quantum information science, composed of quantum computing, quantum communication, and quantum metrology. These so-called quantum defects are particularly appealing because they are fixed in a controlled solid-state environment, hold the promise of room temperature operation, and will benefit from mature semiconductor fabrication techniques for integration and scaling. First-principles calculations based on density functional theory have been indispensable for the study of point defects: such calculations provide crucial microscopic insight that may be inaccessible in experiments. In this dissertation, we develop and apply first-principles methodologies to treat quantum defects.

Nonradiative transitions are integral to the control and operation of quantum defects. Indeed, nonradiative transitions dissipate energy through vibrations and thus can impact the quantum efficiency of a given quantum defect. We developed the `Nonrad` code, which implements a quantum-mechanical formalism to evaluate the nonradiative transition rate from first principles. We also put into effect several important modifications that are essential for attaining accurate rates.

Identifying novel quantum defects is of vital importance for their widespread utilization in quantum information science. Boron nitride is an ultra-wide-band-gap material with excellent thermal and chemical stability, making it a promising host for

quantum defects and for applications in electronic devices. Control over conductivity is essential to utilize boron nitride in the proposed applications. In cubic boron nitride, we assess potential dopants and their ability to produce *n*-type conductivity.

In hexagonal boron nitride, bright single-photon emitters have been observed in the visible spectrum; however the microscopic origin of the emission has eluded researchers. Here we propose boron dangling bonds as the origin of the emission and provide a thorough characterization of their properties. We find that boron dangling bonds possess an optical transition with minimal coupling to phonons; we also calculate the magnetic-field dependence and show it to be in agreement with experiments. In a monolayer, we find that the boron dangling bond will behave similarly to when it is embedded in bulk material. Furthermore, we demonstrate the importance of out-of-plane distortions on the dangling bond, a result that has implications for other quantum defects in two-dimensional materials. Finally, in a fruitful collaboration with the experimental group of Prof. Lee Bassett at the University of Pennsylvania, we elucidated the optical dynamics of boron dangling bonds.

In total, this work advances the study of quantum defects through the development and application of first-principles techniques.

Contents

List of Figures

Chapter 1

Introduction

Harnessing the power of quantum mechanics has been heralded as an enabler for a variety of technologies. The first quantum revolution provided us with an understanding of the materials and devices that underpin modern society: transistors for the computers we have in our pockets, light-emitting diodes for efficient light production that has drastically cut global energy costs, and photovoltaics for harvesting sunlight, which will be essential if humanity is to avoid a climate catastrophe.

All of these technologies rely on an understanding of quantum mechanics. The fact that a particle such as an electron may also act as a wave (*wave-particle duality*) enables us to understand chemical bonding. Wave-particle duality also explains how electrons tunnel through a barrier, a process fundamental to many electronic devices. The need for an improved understanding and control of quantum-mechanical effects continues to grow as we push devices to nanometer length scales.

In parallel, we are witnessing a second quantum revolution [1, 2], where we utilize single quantum states to *create* new technologies. Much of the promise of the second quantum revolution is embodied by the field of quantum information science, com-

posed of quantum computing, quantum communication, and quantum metrology. Quantum computing takes advantage of the exponential scaling of the Hilbert space to perform exceedingly complex calculations at unprecedented speeds [3]. Quantum communication uses the fact that observation of a quantum system leads to wavefunction collapse; secure communication channels exploit this property to ensure no one is listening in [4, 5]. Lastly, quantum metrology builds upon the fact that quantum states are inherently sensitive to their environment and, with their small size, enable sensing at the nanoscale [6]. Interestingly, the inherent sensitivity that makes quantum states suitable for metrology renders realizing quantum computation difficult.

Quantum metrology is the most advanced incarnation of quantum information science, already at the stage of commercialization. On the other hand, the feasibility of large-scale quantum computing has yet to be demonstrated. It is an open question whether the errors inherent in performing quantum computations can be controlled and overcome [7]. Quantum computing is at a nascent stage similar to where classical computing was in the 1940s and 50s; current quantum computers are large, bulky machines designed to control just a few units of information. There is no doubt that classical computers have revolutionized our lives, and there is considerable hope that quantum computers may one day do the same.

At the center of all of this is the *qubit*, a two-state quantum system that is the basic unit of quantum information. A major focus of the field is on improving existing qubits and designing new ones with better properties. A particularly promising platform is based on point defects embedded in a semiconductor or insulator [8]. In this dissertation, I use "point defect" to refer to both intrinsic defects, such as single-atom vacancies, and extrinsic impurities. Point defects, in contrast to extended defects, consist of one or a few atoms and can be understood as a molecule fixed in the lattice.

From this perspective, point defects are extremely attractive [8, 9]: there is no need for complicated ion traps to hold the qubit in place, and each defect is exposed to a controlled environment defined by the host lattice. Point-defect-based qubits hold the promise of room-temperature operation, in contrast to most other qubit incarnations that require extremely low temperatures. A point-defect-based technology also benefits from mature semiconductor fabrication techniques, which will facilitate scaling and integration.

Point defects that are useful for quantum applications are referred to as "quantum defects", and those that are interfaced optically fall into two categories (that are not mutually exclusive) [10]: *single-photon emitters*, which emit a photon in a well-defined quantum state to be used as the qubit; and *spin centers*, which use the ground-state electronic spin as the qubit. The prototype quantum defect is the NV center in diamond (a nitrogen atom next to a carbon vacancy) [11], which has been used to demonstrate feats of sensing [12–14], quantum networking [15], and long-range entanglement [16, 17].

The NV center has many limitations, however. Its optical interface is extremely lossy with 97.6% of the photons produced not capable of transmitting quantum information due to coupling to phonons [18]. Diamond is also a difficult material to work with [19], exemplified by the many years of failed attempts at integrating diamond into electronic devices. On top of this, the diamond surface is extremely "noisy", introducing sources of decoherence that limit the sensitivity and coherence time of the NV center [20, 21]. While an understanding of the various transitions and quantum states comprising the NV center has been built [11], a fully first-principles description is still lacking. This problem goes beyond the NV center in diamond: the ability not only to characterize but to *predict* the properties of quantum defects from first princi-

ples would greatly accelerate the design of better qubits.

We thus identify two outstanding issues in the field: (i) the need for first-principles methodologies to describe quantum defects and (ii) the prediction of novel quantum defects with superior properties. In this dissertation, I address both these issues with first-principles calculations based on density functional theory. Density functional theory has become an indispensable tool for providing atomistic insight into quantum-mechanical processes in materials. The foundations of density functional theory and their application to quantum defects are discussed in Chapter 2. First I describe an open-source code I developed for calculating nonradiative transitions to address issue (i). Nonradiative transitions are fundamental to the understanding of quantum defects, dictating the efficiency and operation of a given qubit. Second I apply these methodologies to novel host materials, in particular cubic and hexagonal boron nitride, to uncover new quantum defects and address issue (ii). For cubic boron nitride, I first elucidate the role of impurities in attaining controlled doping. In hexagonal boron nitride, single-photon emitters have been observed that are ultra-bright, stable, and have minimal coupling to phonons, making them extremely appealing. However the microscopic origin of these emitters is intensely debated. I propose a specific defect, the boron dangling bond, as the microscopic origin and utilize the developed first-principles methodologies to build a coherent understanding of the experimental results. In the following sections, I describe in detail the improvements to the nonradiative transition methodology and my efforts in characterizing novel quantum defects.

1.1 Computing Nonradiative Rates from First-Principles

Semiconductors and insulators are defined by the presence of a band gap, a window of energy where no electron states exist. Point defects break the symmetry of the crystal and can introduce states in the band gap. The level structure that is possible from these states can be extremely rich, as shown in Fig. 1.1. A variety of transitions between the levels are available; some of these are radiative, i.e., they emit light (photons), and others are nonradiative, i.e., they dissipate energy in the form of heat (phonons). Evaluating the transition rates is crucial to characterize a given quantum defect, for example to determine the quantum efficiency.

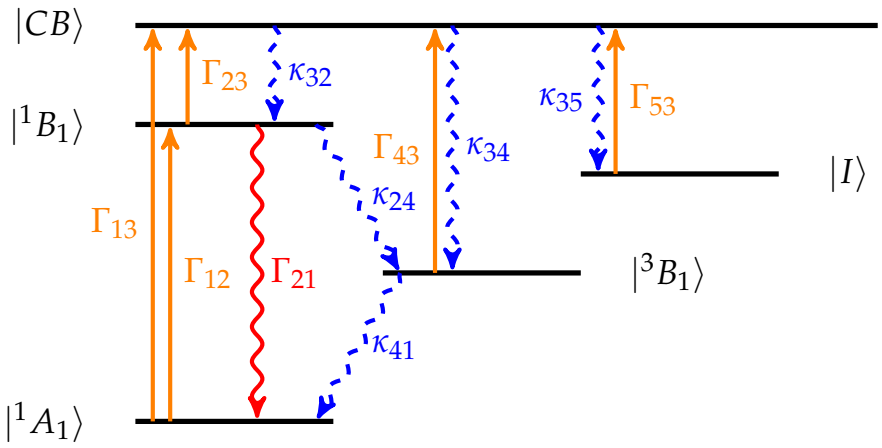

Figure 1.1: Most general level diagram for the boron dangling bond, a quantum defect in hexagonal boron nitride. Black lines indicate quantum states and are labeled by the irreducible representation of the C_{2v} point group that the state transforms as. $|CB\rangle$ is the conduction band and $|I\rangle$ is a general, nearby impurity. Orange arrows indicate absorption or photoionization transitions. Red wavy arrows indicate radiative transitions. Blue dashed arrows indicate nonradiative transitions.

I developed the `Nonrad` code to implement a first-principles approach for the evaluation of nonradiative transition rates [22], which is discussed in Chapter 3. This implementation is based on a quantum-mechanical description of the process utilizing Fermi's golden rule within the static coupling approximation [23]. I present an

approach for evaluating electron-phonon coupling within the projector augmented-wave formalism. This formalism is regarded as the most accurate method within pseudopotential theory because it retains the full all-electron wavefunction; however, this accuracy comes at the expense of considerable complexity, which I comprehensively address in my formalism. I also critically evaluate the common procedure of replacing Dirac delta functions with Gaussians to account for the variety of broadening mechanisms that are present in real crystals. This approach is widely used not only in the evaluation of nonradiative transition rates, but also in a variety of other calculations, from scattering rates to absorption spectra. I found, however, that this procedure can introduce inaccuracies in the resulting transition rates, and I therefore developed an alternative scheme based on interpolation.

An additional issue I had to address relates to the fact that nonradiative transitions often occur at charged defects, which attract or repel free carriers due to the Coulomb potential. This interaction impacts the nonradiative transition rate and is described by the "Sommerfeld parameter". An analytic approximation of this parameter is commonly used, which I found to be inadequate in some cases; I therefore propose to replace the approximation with a rigorous numerical evaluation.

These developments greatly improve the accuracy and reliability with which nonradiative transition rates can be evaluated from first principles. The `Nonrad` code has been made publicly available [24], making the calculation of nonradiative rates accessible to a wide community of researchers. Beyond the field of quantum defects, nonradiative transitions have important implications for the operation of electronic and optoelectronic devices. For example, a first-principles understanding of defects in the halide perovskites will be essential to push the limits of photovoltaic efficiency [25–29].

1.2 Novel Quantum Defects

Identifying novel host materials for quantum defects is an outstanding challenge of vital importance to quantum information science. Boron nitride is an excellent candidate material due to its ultrawide band gap, as well as chemical and thermal stability. Boron nitride can crystallize in a variety of crystal structures (polymorphs). The cubic form, which is the III-V compound analogue to diamond, is a natural starting place for the design of novel quantum defects. However, to utilize cubic boron nitride as a host for quantum defects, as well as for other electronic or optoelectronic applications, control of its conductivity is required. The conductivity of semiconductors is governed by the addition of small amounts of "dopant" impurities. I performed a thorough investigation of *n*-type dopants in cubic boron nitride and identified O_N and Si_B as promising dopants [30]. Compensation from boron vacancies poses a problem, and I outline an approach to control the growth kinetics to overcome this issue. Based on my comprehensive survey, I propose complexes between dopants and vacancies, such as V_B-O_N and V_B-Si_B, as potential quantum defects. The details of this study are discussed in Chapter 4.

To utilize a quantum defect for quantum metrology, it is necessary to generate the defect as close to the sensing target as possible. In a three-dimensional material such as diamond, this necessitates placing the defect close to the surface. Unfortunately the surface is a major source of decoherence due to broken bonds and other surface defects. Two-dimensional materials, in which the bonding character avoids the formation of electrically active surface states, have been proposed as an alternative to avoid noisy surfaces. In a two-dimensional material, the defect can even be placed in a single monolayer, free from the surface defects that plague three-dimensional

materials. Hexagonal boron nitride is a leading candidate material and ultra-bright single-photon emitters have been observed by a number of experimental groups. One class of emitters is found in the visible spectrum near 2 eV. They have minimal coupling to phonons and are stable up to 800 K. Furthermore, experiments have found that the emitters respond to a magnetic field, which is necessary to act as a spin qubit or for spin-based sensing.

The microscopic origin of these single-photon emitters has eluded researchers. This is largely because the emitters are notoriously heterogeneous, exhibiting a range of properties with seemingly contradictory observations. Overcoming this heterogeneity is clearly essential to enable applications in quantum information science; the crucial first step is to identify the chemical and structural nature of the emitter, which I have addressed by performing first-principles calculations. Based on my hybrid functional density functional theory calculations, I propose boron dangling bonds (broken bonds resulting from a defect within the layer, depicted in Fig. 1.2) as the likely microscopic origin [31]. Dangling bonds and their properties are discussed in Chapter 5. The observed single-photon emission is attributed to an optical transition where an electron is excited from a doubly-occupied boron dangling bond to a localized B p_z state; this gives rise to a fundamental transition (the "zero-phonon line") at 2.06 eV and emission with a Huang-Rhys factor (the parameter that characterizes the coupling to phonons) of 2.3, in good agreement with the experimental values. A unique feature of the dangling-bond model is that it allows photoionization to occur due to the proximity of the defect state to the conduction band. The photoionization process provides an explanation for the experimental observation that the alignment of the absorptive and emissive dipole depends on the excitation energy. The dangling-bond model also agrees with the observed magnetic-field dependence, predicting a singlet

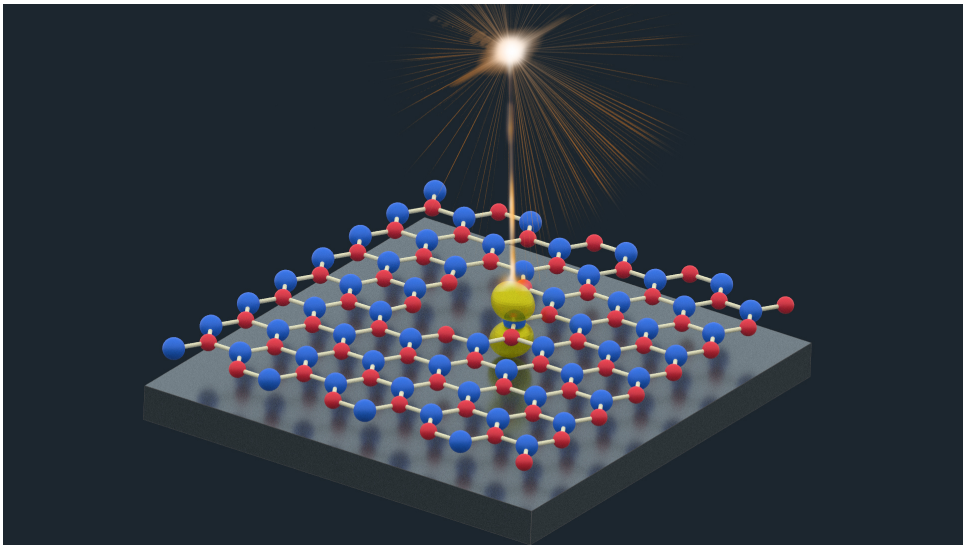

Figure 1.2: An artistic depiction of the boron dangling bond embedded in hexagonal boron nitride emitting a single photon.

ground state and a metastable triplet state.

The above calculations focused on the dangling bond in samples consisting of multiple layers of hexagonal boron nitride (effectively the same as bulk), consistent with what is used in the majority of experiments. However, as noted above, it is desirable for applications to position the quantum defect in a single monolayer. I therefore also investigated the dangling bond in a single monolayer [32] and found that most of the properties, such as the zero-phonon line and coupling to phonons, are largely unchanged from their bulk values. One exception is the triplet-state geometry, which slightly differs and hence may influence the magnetic-field dependence. An important aspect of these monolayer calculations is that charged defects in reduced dimensions need to be very carefully treated; my work has addressed how to correctly handle the compensating background charge in periodic boundary conditions. These results and a discussion of charged defects in reduced dimensions are presented in Chapter 6.

A major feature of two-dimensional materials that is commonly disregarded is

the fact that they exist in three dimensions: relevant physics from the bending and twisting of the two-dimensional plane is often overlooked. I explicitly investigate the effects of an out-of-plane distortion on the quantum defect [33] in Chapter 7. I accomplish this by deforming a plane neighboring the dangling bond, and studying the resulting relaxation of the defect. The zero-phonon line and coupling to phonons shift as a result, demonstrating that the dangling bond is sensitive to the local environment. I propose this is the major source of the heterogeneity observed in experiments.

My work on quantum defects in hexagonal boron nitride culminated in a joint theoretical and experimental effort to characterize the full optical dynamics of the single-photon emitters [34]. Our experimental collaborators in the group of Prof. L. Bassett (U. Pennsylvania) utilized photon emission correlation spectroscopy to extract the level structure and transition pathways through the levels. The general level diagram for the dangling-bond defect (shown in Fig. 1.1) is in very good agreement with the experimental results. The calculated radiative rate is close to the experimental value; for nonradiative transitions, I utilized the developments in the `Nonrad` code. I calculated the nonradiative transition rate for capture of an electron in the conduction band directly into the excited state and compare to capture into the ground state. Capture into the excited state is favored by several orders of magnitude, and the calculated rate is in agreement with the value extracted from experiment. This result confirms our prediction of the role of photoionization. The overall agreement of the calculated rates with experiment, including for photoionized electrons, provides strong support for the attribution of the 2 eV single-photon emission to the boron dangling bond. A detailed overview of the experiments and our interpretation in the presence of my first-principles calculations of the dangling bond are presented in Chapter 8.

1.3 Summary

Quantum defects are a leading platform to power the second quantum revolution. I developed the `Nonrad` code and improved the methodology for treating nonradiative transitions from first principles, thus supplying an essential tool for a fully first-principles treatment of quantum defects. I then applied our methodologies to defects in cubic and hexagonal boron nitride to address the need for novel quantum defects. In cubic boron nitride, I predicted which dopants could be effective donors, and proposed several potential quantum defects. For hexagonal boron nitride, I proposed boron dangling bonds as the microscopic origin of the 2 eV single-photon emission. I extensively characterized the level structure of this quantum defect, finding very favorable agreement with experiments. Overall, this work constitutes a significant step forward in the methodology and design of quantum defects. The insights developed here will not only benefit the technologies of the second quantum revolution but also impact the first quantum revolution: enhanced understanding and control of nonradiative processes will enable better electronic and optoelectronic devices.

Chapter 2

Theoretical Background

2.1 The Many-Body Problem

The study of quantum defects from first principles begins with a firm grounding in the quantum-mechanical foundations. A natural starting place is with the time-dependent Schrödinger equation in Dirac notation,

$$i\hbar\frac{d}{dt}\left|\Psi(t)\right\rangle = \hat{H}\left|\Psi(t)\right\rangle \ , \tag{2.1}$$

where $\hbar$ is the reduced Planck's constant and $|\Psi(t)\rangle$ is the many-body state of our system of interest. In the position representation, the many-body wavefunction is given by $\Psi(\mathbf{r}_1, \mathbf{r}_2, \ldots; t) = \langle \mathbf{r}_1, \mathbf{r}_2, \ldots | \Psi(t)\rangle$. We see that the many-body wavefunction is a function of the positions of each of the electrons and is therefore an unwieldy object to utilize, as we will discuss later. The Hamiltonian $\hat{H} = \hat{T} + \hat{V}$ contains contributions of both the kinetic energy $\hat{T}$ and potential energy $\hat{V}$, which in general may depend on both space and time.

Practical calculations typically utilize a time-independent potential. (The effects of time-dependent quantities are usually studied perturbatively, as described in Sec. 2.6.2.)

In this case, separation of variables allows us to write $|\Psi(t)\rangle = e^{-iEt/\hbar}|\Psi\rangle$. E is then the eigenenergy of the time-independent Schrödinger equation,

$$\hat{H}|\Psi\rangle = E|\Psi\rangle \ , \tag{2.2}$$

which has the form of an eigenvalue problem.

Here the system of interest is a collection of atomic nuclei and electrons. We may write down the Hamiltonian for this system (in SI units) as [35]

$$\begin{aligned}\hat{H} = &-\frac{\hbar^2}{2m_e}\sum_i \hat{\nabla}_i^2 + \frac{1}{2}\sum_{i\neq j}\frac{1}{4\pi\epsilon_0}\frac{e^2}{|\hat{\mathbf{r}}_i - \hat{\mathbf{r}}_j|} - \sum_{i,I}\frac{1}{4\pi\epsilon_0}\frac{Z_I e^2}{|\hat{\mathbf{r}}_i - \mathbf{R}_I|} \\ &-\sum_I \frac{\hbar^2}{2M_I}\nabla_I^2 + \frac{1}{2}\sum_{I\neq J}\frac{1}{4\pi\epsilon_0}\frac{Z_I Z_J e^2}{|\mathbf{R}_I - \mathbf{R}_J|} \ ,\end{aligned} \tag{2.3}$$

where lowercase subscripts label electrons and uppercase subscripts label nuclei. m_e is the electron mass, e is the fundamental charge, and ϵ_0 is the vacuum permittivity. M_I is the atomic mass and Z_I is the atomic charge of the Ith nuclei.

Atomic nuclei are much heavier than the electrons ($M_I \gg m_e$). In Eq. 2.3, we may therefore assume that the kinetic energy of the nuclei is negligible. This assumption is known as the Born-Oppenheimer or adiabatic approximation [36]. The interaction between nuclei (the fifth term of Eq. 2.3) is treated as a classical electrostatic interaction, which contributes an energy E_{II} but is not germane to the description of the electrons. The remaining terms in Eq. 2.3 may be identified as

$$\hat{H} = \hat{T} + \hat{V}_{\text{int}} + \hat{V}_{\text{ext}} + E_{II} \ , \tag{2.4}$$

where the kinetic energy for the electrons is

$$\hat{T} = -\frac{\hbar^2}{2m_e}\sum_i \hat{\nabla}_i^2 \ , \tag{2.5}$$

the electron-electron interaction is

$$\hat{V}_{\text{int}} = \frac{1}{2}\frac{1}{4\pi\epsilon_0}\sum_{i\neq j}\frac{e^2}{|\hat{\mathbf{r}}_i - \hat{\mathbf{r}}_j|} \,. \tag{2.6}$$

and the external potential felt by the electrons provided by the nuclei is,

$$\hat{V}_{\text{ext}} = -\frac{1}{4\pi\epsilon_0}\sum_{i,I}\frac{Z_I e^2}{|\hat{\mathbf{r}}_i - \mathbf{R}_I|} \,, \tag{2.7}$$

Thus the Hamiltonian describes electrons quantum-mechanically in the external potential of the nuclei, which are fixed in place from the point of view of the electrons.

It is the electron-electron interaction $\hat{V}_{\text{int}}$ that poses a problem for practical calculations. Without it, the Hamiltonian only contains one-electron terms, and we would have a system of non-interacting, *independent* electrons. Such a system may be decoupled with each electron treated individually, and the wavefunction could be easily factorized. The electron-electron interaction is a two-electron operator, which allows pairs of electrons to "communicate" with one another and introduces *correlations* between electrons. *Exchange* is a well-defined form of correlation and is a manifestation of the Pauli exclusion principle: two or more electrons, which are fermions, cannot occupy the same quantum state. Understanding and treating electronic correlation is one of the outstanding problems in condensed matter physics [35, 37, 38].

This problem is most clearly illustrated by examining the many-body wavefunction Ψ. Consider solving Eq. 2.2 directly for the Hamiltonian in Eq. 2.3 using a grid-based method. With a coarse grid of just 10 points per spatial coordinate, the many-body wavefunction would require 10^{3N_e} grid points to represent, where N_e is the number of electrons. Already by the cobalt atom ($N_e = 27$), we will have more grid points than there are atoms in the universe ($\approx 10^{80}$) [39]. Therefore, just storing the wavefunction—let alone *solving* for it—would be intractable.

Instead, imagine we had a system of non-interacting, independent electrons (e.g., neglecting V_{int} in Eq. 2.3). In this case, our electrons no longer "communicate" and can be solved individually. Each electron's wavefunction is represented with 10^3 grid points, and our total system requires just $N_e \times 10^3$ grid points. In other words, we have turned our *exponential* problem into a *linear* one. This is one of the foundational ideas of the Kohn-Sham approach [40], utilizing an independent system to provide insight into the interacting system. The Kohn-Sham approach, which is grounded in density functional theory [41], has become the workhorse computational method for practical first-principles calculations. It has been widely used to study defects [42–44], alloys [45, 46], and a variety of other systems [35].

To define this independent system, we first need to shift our focus away from the many-body wavefunction. Instead, we concentrate on the electron density $n(\mathbf{r})$:

$$n(\mathbf{r}) = \sum_i \langle \Psi | \delta(\hat{\mathbf{r}} - \hat{\mathbf{r}}_i) | \Psi \rangle \ . \tag{2.8}$$

The electron density is a simple function of the spatial coordinates. (It would require only 10^3 grid points to represent in the above example!) In the following section, we show the importance of the electron density through the Hohenberg-Kohn theorems.

2.2 Hohenberg-Kohn Theorems

Pierre Hohenberg and Walter Kohn laid the foundations of density functional theory in 1964 [41]. Their work is summarized by two theorems, which demonstrate the importance of the ground-state density. The proofs of these theorems are disarmingly simple.[1]

[1] The proof is left as an exercise for the reader.

The first theorem is as follows:

Theorem 1 *For any system of interacting particles in an external potential V_{ext}, the potential V_{ext} is uniquely determined (up to a constant) by the ground-state density n_0.*

In other words, there is a one-to-one mapping between the external potential V_{ext} and the ground-state density n_0. Since the external potential is determined from the ground-state density, the Hamiltonian of the system is also determined. And since the Hamiltonian is determined, the many-body wavefunctions for all excited and ground states are determined. Therefore, *all properties of the system* are determined by the ground-state density. This clearly highlights the importance of the ground-state density. However, we are still left with a many-body problem that needs to be solved, since we only know how to obtain the ground-state density from the many-body wavefunction (Eq. 2.8).

The second theorem addresses this problem by providing an alternative way to obtain the ground-state density.

Theorem 2 *A universal functional for the energy $E[n]$ can be defined in terms of the density n, which is valid for any V_{ext}. For a given V_{ext}, the exact ground-state energy is obtained by minimizing the functional, and the density that minimizes the functional is the exact ground-state density n_0.*

The energy functional $E[n]$ in Theorem 2 is given by

$$E[n] = T[n] + E_{\text{int}}[n] + \int d^3r\, V_{\text{ext}}(\mathbf{r})n(\mathbf{r}) + E_{II}\ , \tag{2.9}$$

which is analogous to Eq. 2.4. Such a functional is universal because the kinetic energy $T[n]$ and interaction energy $E_{\text{int}}[n]$ are defined the same for all electron systems. The explicit form of the kinetic and interaction energy functionals, however, is unknown.

If they were known, we could minimize Eq. 2.9 with respect to variations in the electron density n to obtain the ground-state energy and density. Following Theorem 1, all properties of the system would then be determined.

The work of Hohenberg and Kohn constitutes a major shift in focus towards the ground-state density as the fundamental quantity. Still, these theorems do not enable practical calculations on their own because there are many unknowns. Most notably, we don't know how to derive all properties of the system from the density alone. To overcome this, we return to the notion from Sec. 2.1 that an independent-particle system is easier to solve.

2.3 Kohn-Sham Equations

In 1965, Walter Kohn and Lu Jeu Sham provided an *ansatz* that the ground-state density of the interacting system is equivalent to that of a well-chosen non-interacting, independent-particle system [40]. For this independent-particle system, the effect of interactions is included through the exchange-correlation functional $E_{\mathrm{xc}}[n]$. In this way, we define the energy functional for the auxiliary Kohn-Sham system as

$$E_{\mathrm{KS}} = T_s[n] + E_{\mathrm{Har}}[n] + E_{\mathrm{xc}}[n] + \int d^3r\, V_{\mathrm{ext}}(\mathbf{r}) n(\mathbf{r}) + E_{II} \,. \tag{2.10}$$

The independent-particle kinetic energy T_s is given by

$$T_s = \frac{\hbar^2}{2m_e} \sum_{\sigma,i} \int d^3r\, |\nabla \psi_i^\sigma(\mathbf{r})|^2 \,, \tag{2.11}$$

where ψ_i^σ is the wavefunction solution to the one-electron Schrödinger for the auxiliary Kohn-Sham system (given below in Eq. 2.14). σ labels the electron spin. The Hartree interaction energy E_{Har} is given by

$$E_{\mathrm{Har}}[n] = \frac{1}{2} \frac{1}{4\pi\epsilon_0} \int d^3r\, d^3r'\, \frac{n(\mathbf{r}) n(\mathbf{r}')}{|\mathbf{r} - \mathbf{r}'|} \,, \tag{2.12}$$

which is a classical Coulomb interaction of the electron density.

The exchange-correlation functional $E_{\text{xc}}[n]$ is defined by comparing Eq. 2.10 to Eq. 2.9. We therefore obtain that

$$E_{\text{xc}}[n] = (T[n] - T_s[n]) + (E_{\text{int}}[n] - E_{\text{Har}}[n]) \, . \tag{2.13}$$

The first term is the difference between the full interacting system's kinetic energy and the independent-particle kinetic energy. The second term is the difference between the interaction energy, which includes all quantum-mechanical effects, and the Hartree interaction, which is classical. In this way, the mapping between the full interacting system and the auxiliary Kohn-Sham system is *exact*. As noted in Sec. 2.2 however, the functional form of T and E_{int} is unknown, so we must make an approximation for E_{xc}. [2] These approximations are discussed in depth in the following section.

But first, we derive the Kohn-Sham equations by taking a functional derivative of E_{KS} (Eq. 2.10) with respect to $\psi_i^{\sigma *}$. The independent-particle wavefunctions ψ_i^σ are subject to orthonormality ($\langle \psi_i^\sigma | \psi_j^{\sigma'} \rangle = \delta_{ij}\delta_{\sigma\sigma'}$). We arrive at the Kohn-Sham equations,

$$\hat{H}_{\text{KS}}^\sigma \, |\psi_i^\sigma\rangle = \varepsilon_i^\sigma \, |\psi_i^\sigma\rangle \ , \tag{2.14}$$

where ε_i^σ are the eigenvalues. The Kohn-Sham Hamiltonian H_{KS} is given by

$$\hat{H}_{\text{KS}}^\sigma = -\frac{\hbar^2}{2m_e}\hat{\nabla}_i^2 + \frac{\delta E_{\text{xc}}}{\delta n^\sigma} + \frac{\delta E_{\text{Har}}}{\delta n^\sigma} + \hat{V}_{\text{ext}} \, , \tag{2.15}$$

where δ indicates a functional derivative and n^σ is the electron density for spin σ. In practical calculations, Eq. 2.14 is solved numerically. The electron density for the independent-particle system is then obtained by

$$n(\mathbf{r}) = \sum_{i,\sigma} |\psi_i^\sigma(\mathbf{r})|^2 \, . \tag{2.16}$$

[2] Another way to understand the Kohn-Sham formalism is as a carefully chosen mean-field approximation.

Notably, the Kohn-Sham equations need to be solved self-consistently due to the fact that the potentials depend on the electron density, which is derived from the wave-functions. Via the Kohn-Sham ansatz, the above density is equivalent to that of the interacting system's density. Following Hohenberg and Kohn, all properties of the system are therefore determined.

2.4 Exchange-Correlation Functionals

Integral to the application of density functional theory is the choice of the exchange-correlation functional. Ideally, we would make the choice that maximizes the accuracy of our calculation, but this is usually not feasible computationally. Thus there is a compromise to be made, which balances computation time and accuracy. The lowest level approximation for the exchange-correlation functional is that of the local density approximation (LDA), provided by Kohn and Sham [40]. In the LDA, the exchange-correlation functional is written as

$$E_{\mathrm{xc}}[n] = \int d^3r\, n(\mathbf{r})\epsilon_{\mathrm{xc}}([n], \mathbf{r}) \,, \tag{2.17}$$

where ϵ_{xc} is the energy per electron at the point $\mathbf{r}$ and depends only on the density in the vicinity of this point. (In other words, it is *local*.) Since the exchange-correlation functional must be universal, the form of ϵ_{xc} can be obtained from the homogeneous electron gas.

The power of the LDA lies in its simplicity (largely in the fact that it is cheap computationally). The LDA enabled practical calculations and is still used today, particularly for structural properties. A natural way to improve the LDA is to include

information on the *gradient* of the density [40],

$$E_{\mathrm{xc}}[n] = \int d^3r\, n(\mathbf{r})\epsilon_{\mathrm{xc}}([n, \nabla n], \mathbf{r}) \,. \tag{2.18}$$

Such an assumption for the exchange-correlation functional is known as the generalized gradient approximation (GGA). The most well-known and widely used GGA was developed by Perdew, Burke, and Ernzerhof (PBE) [47]. In this way, we step up the "rungs of the ladder of exchange-correlation approximations" shown in Fig. 2.1. Hybrid functionals are an important rung because they enable quantitative calculations of quantum defects and are discussed in the following section.

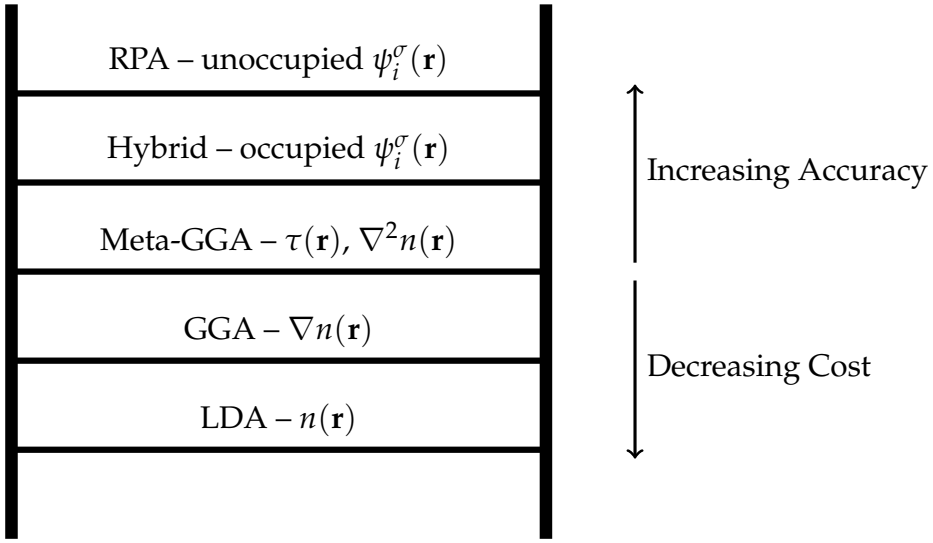

Figure 2.1: The "ladder" of exchange-correlation approximations from the LDA to the random-phase approximation (RPA). $\tau(\mathbf{r})$ is the kinetic energy density and $\tau(\mathbf{r}) \propto |\nabla n(\mathbf{r})|^2/n(\mathbf{r})$. Adapted from Ref. [48].

2.4.1 Hybrid Functionals

A particularly important approximation for the exchange-correlation functional is known as the hybrid functional. Hybrid functionals include a fraction of exact ex-

change within Hartree-Fock theory [49]. The term "hybrid" is used because Hartree-Fock exchange is orbital dependent and not strictly a functional of the density. Hybrid functionals are widely employed, as they enable accurate evaluation of energetics and atomic geometries of a variety of systems. Most importantly, hybrid functionals overcome the well-known band-gap problem of local and semi-local functionals [50–52], which is intimately tied to the description of charge localization [53].

In the most general hybrid functional, the Coulomb interaction is split into a short-range (SR) and long-range (LR) component using the identity [52, 54],

$$\frac{1}{r} = \underbrace{\frac{\mathrm{erfc}(\mu r)}{r}}_{\mathrm{SR}} + \underbrace{\frac{\mathrm{erf}(\mu r)}{r}}_{\mathrm{LR}}, \tag{2.19}$$

where μ is the screening parameter that defines the range separation. Next, we introduce two mixing parameters, which specify the fraction of Hartree-Fock exchange to be included: one is the short-range mixing parameter α_s, and the other is the long-range mixing parameter α_l. Therefore, the exchange-correlation functional for the most general hybrid functional $E_{\mathrm{xc}}^{\mathrm{hyb}}$ is given by

$$\begin{aligned} E_{\mathrm{xc}}^{\mathrm{hyb}}(\alpha_s, \alpha_l; \mu) = \alpha_s E_{\mathrm{x}}^{\mathrm{SR,HF}}(\mu) + (1-\alpha_s) E_{\mathrm{x}}^{\mathrm{SR,PBE}}(\mu) \\ + \alpha_l E_{\mathrm{x}}^{\mathrm{LR,HF}}(\mu) + (1-\alpha_l) E_{\mathrm{x}}^{\mathrm{LR,PBE}}(\mu) + E_{\mathrm{c}}^{\mathrm{PBE}}, \end{aligned} \tag{2.20}$$

where E_{x} is the long-range or short-range exchange contribution calculated at the Hartree-Fock (HF) or PBE level, following the decomposition in Eq. 2.19. $E_{\mathrm{c}}^{\mathrm{PBE}}$ is the correlation energy calculated at the PBE level.

In Eq. 2.20, three parameters must be determined. It has been shown that the long-range mixing parameter α_l is inversely related to the electronic dielectric constant ϵ_∞ (i.e., $\alpha_l = \epsilon_\infty^{-1}$) [55]. The screening parameter μ can be approximated through Thomas-

Fermi screening [56]:

$$\mu = \frac{8}{3b(1-\epsilon_\infty^{-1})}\left(\frac{3N_{\text{val}}}{\Omega\pi}\right)^{1/3}, \tag{2.21}$$

where $b = 1.563$ is an empirical parameter [57], N_{val} is the number of valence electrons, and Ω is the cell volume. The short-range mixing parameter α_s may be taken to be 0.25, based on the arguments of Perdew, Burke, and Ernzerhof [58]; on the other hand, α_s may be taken to be 1, in connection with the Coulomb-hole static-exchange approximation from many-body perturbation theory [59]. Alternatively, any one of these parameters may be tuned to enforce the generalized Koopmans' condition [60] on a localized state [61, 62].

The above arguments demonstrate that the parametrization of the hybrid functional is material-dependent. As a result, utilizing these methods to determine the parameters can significantly improve the predictive capability of the hybrid functional, compared to a naive material-independent parametrization. Indeed these methods predict band gaps in good agreement with the experimental value [56, 61], although the "best" method is not clear. In many cases, it has become common practice to instead choose the parameters that reproduce the experimental band gap.

In this dissertation, I utilize the hybrid functional parameterization of Heyd, Scuseria, and Ernzerhof (HSE) [63, 64]. The HSE functional is widely used for solid-state systems due to its excellent accuracy and computational expediency, thanks to the exclusion of long-range exact exchange. The exchange-correlation energy for the HSE functional is given by $E_{\text{xc}}^{\text{HSE}}(\alpha;\mu) = E_{\text{xc}}^{\text{hyb}}(\alpha,0;\mu)$. Motivated by physical arguments, the original parameterization utilized $\alpha = 0.25$ and $\mu = 0.2$ Å^{-1}. Here, we keep the screening parameter the same, but tune the mixing parameter α to match the computational band gap to the experimental band gap. In specific cases, we also verified that this choice results in Koopmans' condition being obeyed.

2.5 Projector Augmented Wave Pseudopotentials

For solid-state systems that are typically simulated with periodic boundary conditions, a plane-wave basis is natural. However the use of plane waves is potentially problematic from a numerical point of view. The Coulomb potential diverges at each nucleus in the system, and as a result, introduces rapid oscillations of the wavefunction near the nucleus. These oscillations require high-frequency plane waves to accurately describe; this would render calculations with a plane-wave basis extremely expensive computationally.

To overcome this issue, the notion of "pseudopotentials" has been introduced. We can distinguish between two types of electrons: *core* electrons, which are strongly localized near the nucleus; and *valence* electrons, which may be more delocalized and participate in bonding. It is the valence electrons that are most relevant for describing the properties of the system. We therefore construct a pseudopotential in which the core electrons are removed and the valence electrons feel an effective ionic potential.

The projector augmented wave (PAW) method [65] has become increasingly popular. PAW pseudopotentials are defined by a linear transformation in which the core electrons are "frozen in". As a result, the full all-electron wavefunction is still accessible. For this reason, PAW pseudopotentials are widely regarded as one of the most accurate pseudopotential methods. The main drawback to PAW pseudopotentials is the complexity for implementation, since the core wavefunctions are represented on a radial grid.

The PAW linear transformation $\hat{\mathcal{T}}$ is given by [65, 66]

$$|\psi\rangle = \hat{\mathcal{T}}\,|\tilde{\psi}\rangle \ , \tag{2.22}$$

where ψ is the all-electron wavefunction that solves Eq. 2.14 (with the indices are

dropped for notational convenience) and $\tilde{\psi}$ is the pseudo-wavefunction. The transformation is chosen such that $\tilde{\psi}$ is smooth and can be represented on a modest plane-wave basis,

$$|\tilde{\psi}\rangle = \frac{1}{\sqrt{\Omega}} \sum_{|\mathbf{q}|<\mathbf{q}_{\text{cut}}} c_{\mathbf{q}} |\mathbf{q}\rangle \ , \tag{2.23}$$

where Ω is the volume of the simulation cell, $\mathbf{q}$ is a reciprocal-space wavevector, q_{cut} is the cutoff for the plane-wave basis, and $c_{\mathbf{q}}$ is the Fourier component.

As noted above, the wavefunction oscillates close to the nucleus. We introduce the notion of a PAW sphere, which is a small volume surrounding the nucleus, and the operator $\hat{\mathcal{T}}^{(I)}$, which is non-zero only in the PAW sphere centered on the Ith nucleus. Therefore, we may write

$$\hat{\mathcal{T}} = \hat{\mathbf{1}} + \sum_I \hat{\mathcal{T}}^{(I)} \ . \tag{2.24}$$

Next we introduce a complete set of partial waves $\phi_n^{(I)}$ and their smooth counterparts $\tilde{\phi}_n^{(I)}$. The partial wave is the rapidly oscillating component of the all-electron wavefunction that we want to replace with its smooth counterpart to obtain the pseudo-wavefunction. Lastly, we introduce the projector function $p_m^{(I)}$, which maps the pseudo-wavefunction onto the partial waves. The projector must satisfy the completeness relation

$$\sum_n |\tilde{\phi}_n^{(I)}\rangle \langle p_n^{(I)}| = \hat{\mathbf{1}} \tag{2.25}$$

and orthogonality

$$\langle p_m^{(I)} | \tilde{\phi}_m^{(I)} \rangle = \delta_{m,n} \ , \tag{2.26}$$

inside the PAW sphere. It is important to note that Eq. 2.25 is only satisfied approximately in typical implementations because a finite number of projectors are used [67]. Ensuring that an appropriate number of projectors are included is important for the accuracy of the PAW transformation.

We may write the PAW transformation as

$$\hat{\mathcal{T}} = \hat{\mathbf{1}} + \sum_I \hat{\mathcal{T}}^{(I)} = \hat{\mathbf{1}} + \sum_{I,n} \left(|\phi_n^{(I)}\rangle - |\tilde{\phi}_n^{(I)}\rangle \right) \langle p_n^{(I)}| \ . \tag{2.27}$$

For $\hat{\mathcal{T}}^{(I)}$ to be non-zero only inside the PAW sphere, we require that $\phi_n^{(I)} = \tilde{\phi}_n^{(I)}$ outside the PAW sphere. With this transformation, instead of solving Eq. 2.14, we now solve a generalized eigenvalue problem in the pseudo-wavefunctions,

$$\hat{\tilde{H}}_{\mathrm{KS}}^{\sigma} |\tilde{\psi}_i^{\sigma}\rangle = \varepsilon_i^{\sigma} \hat{S} |\tilde{\psi}_i^{\sigma}\rangle \ , \tag{2.28}$$

where $\hat{\tilde{H}}_{\mathrm{KS}}^{\sigma} = \hat{\mathcal{T}}^{\dagger} \hat{H}_{\mathrm{KS}}^{\sigma} \hat{\mathcal{T}}$ and the overlap matrix $\hat{S} = \hat{\mathcal{T}}^{\dagger} \hat{\mathcal{T}}$.

The expectation value of a general operator $\hat{O}$ is given by

$$\langle \hat{O} \rangle = \sum_{i,\sigma} f_i^{\sigma} \langle \psi_i^{\sigma} | \hat{O} | \psi_i^{\sigma} \rangle \ , \tag{2.29}$$

where f_i^{σ} is the occupation factor and the other term in the sum is the one-electron expectation value. If we assume the operator is also local, the one-electron expectation value (again dropping the indices for notational convenience) is expressed as

$$\begin{aligned} \langle \psi | \hat{O} | \psi \rangle &= \langle \tilde{\psi} | \mathcal{T}^{\dagger} \hat{O} \mathcal{T} | \tilde{\psi} \rangle \\ &= \langle \tilde{\psi} | \hat{O} | \tilde{\psi} \rangle + \sum_{m,n,I} \left(\langle \phi_m^{(I)} | \hat{O} | \phi_n^{(I)} \rangle - \langle \tilde{\phi}_m^{(I)} | \hat{O} | \tilde{\phi}_n^{(I)} \rangle \right) \langle \tilde{\psi} | p_m^{(I)} \rangle \langle p_n^{(I)} | \tilde{\psi} \rangle \ . \end{aligned} \tag{2.30}$$

Thus we see that the expectation value must be evaluated in the pseudo-wavefunction basis, the partial-wave basis, and the smooth partial-wave basis. In this way, the expectation value of the operator includes the pseudo-wavefunction contribution (the first term) and a correction from the core (the second term). Non-local operators require careful treatment because they introduce cross-terms between PAW spheres; this issue is discussed in Refs. [65, 66]. The overlap operator $\hat{S}$ is the special case of Eq. 2.30 with $\hat{O} = \hat{\mathbf{1}}$.

2.6 Point Defects

The previous sections have developed the formalism regarding general density functional theory calculations. Here we turn our attention to the treatment of point defect calculations within this framework, highlighting the details that are important for quantum defects.

2.6.1 Formalism

Crystalline solid-state systems are best simulated within periodic boundary conditions. Point defects, on the other hand, break the translational symmetry and thus have no periodicity. Various approaches have been developed to overcome this disparity [68, 69]. The most widely used is the supercell approach, which I employ in this dissertation. Within this approach, a point defect is embedded in a large supercell, a simulation cell that is some multiple of the unit cell, and modeled within periodic boundary conditions. The construction of a supercell is depicted in Fig. 2.2. Care is taken to minimize periodic interactions between images of the defect or to explicitly correct for them.

The supercell formalism was carefully reviewed by Freysoldt *et al.* [42]. The central quantity of interest is the defect formation energy E^f and is given by

$$E^f[X^q] = E_{\text{tot}}[X^q] - E_{\text{tot}}[\text{Bulk}] - \sum_i n_i \mu_i + q(E_{\text{VBM}} + E_F) + \Delta_q \ , \tag{2.31}$$

where $E_{\text{tot}}[X^q]$ is the total energy of the supercell containing the defect X in charge state q and $E_{\text{tot}}[\text{Bulk}]$ is the total energy of the pristine supercell. E_{VBM} is the energy of the valence-band maximum and E_F is the Fermi level. Δ_q is a correction term that accounts for the effects that arise from the use of a charged finite-size supercell [70, 71].

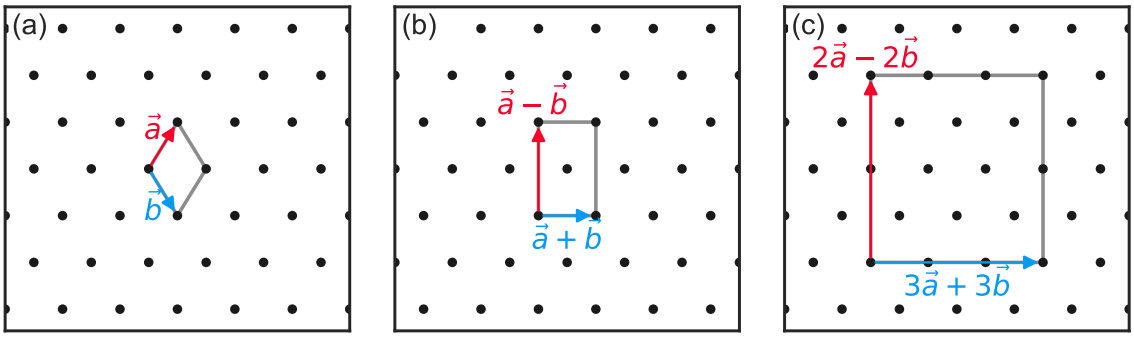

Figure 2.2: The construction of a supercell where the (a) unit cell is first transformed to an (b) orthogonal basis before (c) scaling to a supercell. This construction results in (approximately) isotropic defect interactions. Black dots are lattice points. The arrows correspond to the lattice vectors from which the lattice points are generated. Grey lines indicate the simulation cell. The lattice vectors in (a) correspond to the in-plane lattice vectors of a hexagonal crystal.

Charged interactions in a two-dimensional material require extra care to treat and are discussed in Chapter 6. The chemical potential μ_i accounts for the addition ($n_i > 0$) or removal ($n_i < 0$) of species in forming the defect. We determine the chemical potentials by considering the growth conditions and potential limiting phases that may form.

The thermodynamic transition level is the Fermi-level position where the defect changes its charge state; it is an electronic property of the defect and is given by

$$\varepsilon(q/q') = \frac{E^f[X^q; E_F = 0] - E^f[X^{q'}; E_F = 0]}{q' - q} , \tag{2.32}$$

where $E^f[X^q; E_F = 0]$ is the formation energy at the valence-band maximum ($E_F = 0$). Using Eq. 2.31, Eq. 2.32 can be rewritten as

$$\varepsilon(q/q') = \frac{(E_{\text{tot}}[X^q] + \Delta_q) - (E_{\text{tot}}[X^{q'}] + \Delta_{q'})}{q' - q} - E_{\text{VBM}} . \tag{2.33}$$

We see that the thermodynamic transition level does not depend on the chemical potentials nor the energy of the bulk. This demonstrates that the thermodynamic transi-

tion level is an electronic property of the defect itself.

Excited states of a point defect are particularly important for the study of quantum defects: such excited states give rise to a rich level structure (e.g., see Fig. 1.1) with a variety of possible transitions. We utilize the constrained-occupation ΔSCF method [72] to study excited states. The evaluation of the rates of possible transitions is discussed in the following section.

2.6.2 Transitions Involving Defects

The above formalism lays the foundation for the study of point defects; in particular, it enables us to study the electronic structure of a given defect. In the study of quantum defects, we are not only interested in the electronic structure but also how the system can transition between the electronic states. The rate at which photons are emitted is essential to characterizing a single-photon emitter. Similarly, the dynamics in a magnetic field are integral to the operation of a spin center. Thus a description of the time-dependent quantities of a point defect is imperative. The density-functional-theory formalism utilized so far is time-independent but provides a basis for perturbation theory. Fermi's golden rule [73, 74] is then utilized to evaluate the transition rate.

Below, we briefly discuss the possible transitions that are relevant for the understanding of quantum defects. We can distinguish between two types of transitions: *bound-to-bound* transitions, which are sometimes referred to as internal transitions and occur between localized defect orbitals; and *free-to-bound* transitions, which occur between a localized defect orbital and a delocalized bulk state. Both an excitation and de-excitation process is possible for each transition type. For internal transitions, there is a natural symmetry between excitation and de-excitation; the same cannot be said

for free-to-bound transitions, which involve delocalized bulk states. The de-excitation process for free-to-bound transitions is referred to as *capture*, and the excitation process is referred to as *emission*. Capture processes are described with a capture coefficient C in units of $\mathrm{cm}^3\ \mathrm{s}^{-1}$. The rate at which electrons (holes) are captured at the defect is Cn (Cp) where n (p) is the density of free electrons (holes).

Radiative Capture

Radiative capture is a capture process in which a photon is emitted and a carrier is trapped at a defect site. The expression for the radiative capture coefficient is given by

$$C_{\mathrm{Rad}} = f\eta_{sp} V \frac{e^2 n_r}{3m_e^2 \epsilon_0 \pi c^3 \hbar^4} |p_{if}|^2 E_{\mathrm{opt}} \ , \tag{2.34}$$

where f is the Sommerfeld parameter [75], V is the supercell volume, n_r is the index of refraction, p_{if} is the momentum matrix element between the defect and band-edge wavefunction, and E_{opt} is the energy of the optical transition. η_{sp} is a factor that accounts for the spin selection rules. If the total spin of the defect is initially a singlet and, after capturing a carrier, is a doublet, then $\eta_{sp} = 1$. Similarly, $\eta_{sp} = 0.5$ for a transition from a doublet to a singlet or from a triplet to a doublet. A first-principles approach for evaluating the radiative capture coefficient was studied by Dreyer *et al.* [76]. Typical radiative capture coefficients are $\approx 10^{-14} - 10^{-13}\ \mathrm{cm}^3\ \mathrm{s}^{-1}$.

Photoionization

Photoionization is an emission process where a photon is absorbed, placing a carrier in a bulk band state. The photoionization rate is given by [77]:

$$\Gamma_{\mathrm{PI}} = n_\nu v_\nu \, \sigma_{\mathrm{PI}}(\hbar\omega_\nu) \ , \tag{2.35}$$

where n_ν is the density of photons with phase velocity v_ν and frequency ω_ν. Thus the photoionization rate depends on the details of the light excitation in a given measurement. The photoionization cross section $\sigma_{\mathrm{PI}}(\hbar\omega)$ however is intrinsic to the defect; it is treated with Fermi's golden rule and is given by

$$\sigma_{\mathrm{PI}}(\hbar\omega) = \frac{4\pi^2\alpha}{n_r}\hbar\omega \sum_j |\mu_{ij}|^2 \delta(\hbar\omega - \varepsilon_{ij}) \,, \tag{2.36}$$

where α is the fine-structure constant and $\varepsilon_{ij} = \varepsilon_j - \varepsilon_i$ is the energy difference of the transition. i labels the defect state and j runs over the bulk bands of interest. μ_{ij} is the transition dipole moment and is related to the momentum matrix element by $p_{ij} = (im_e\varepsilon_{ij}/\hbar)\mu_{ij}$. (A factor of $1/3$ sometimes appears in Eq. 2.36 when assuming either the photons or defects are randomly oriented with respect to one another.) A first-principles evaluation of the photoionization cross section was provided by Razinkovas *et al.* [78]. Importantly, they included the effect of coupling to phonons via a convolution of the cross section with the electron-phonon spectral function.

Nonradiative Capture via Multiphonon Emission

Nonradiative capture via multiphonon emission is a capture process in which phonons are emitted and a carrier is trapped at a defect site. Semiclassically, the nonradiative capture process can be understood as a thermally activated process where the system must first overcome a barrier, followed by the emission of phonons. Alkauskas *et al.* provided a formalism to evaluate the nonradiative capture coefficient from first principles [23]. In it, a single-mode approximation is employed, and the capture coefficient is evaluated based on quantum-mechanical principles. The nonradiative capture coefficient is given by

$$C_{\mathrm{NR}} = f\frac{2\pi}{\hbar} g V W_{if}^2 \sum_m w_m \sum_n |\langle\chi_{im}|\hat{Q} - Q_0|\chi_{fn}\rangle|^2 \delta(\Delta E + m\hbar\Omega_i - n\hbar\Omega_f) \,. \tag{2.37}$$

g is the configurational degeneracy, f is a scaling factor to account for charge interactions in a periodic cell, V is the volume of the supercell, and w_m is the thermal occupation factor for the mth vibrational mode of the initial state. $\Omega_{i/f}$ are the phonon frequencies of the initial (i) and final (f) state derived from the configuration coordinate diagram, and Q_0 is the geometry for the perturbative expansion. ΔE is the energy difference between the initial and final state, and W_{if} is the electron-phonon coupling matrix element. Nonradiative capture coefficients can span many orders of magnitude ($\approx 10^{-14} - 10^{-4}$ cm^3 s^{-1}) [79] and as a result, often dominate over radiative capture.

Evaluating the nonradiative capture coefficient is the subject of Chapter 3. In Chapter 3, I discuss the development of a python code `Nonrad` [22, 24], which implements the above equation. I also discuss several improvements to the methodology.

Thermal Emission

Thermal emission is a nonradiative emission process in which an electron or hole from a defect state is thermally excited into the bulk bands. Under thermodynamic equilibrium, the rate of thermal emission should be proportional to the rate of nonradiative capture [79–81]. (We implicitly assume that nonradiative capture dominates.) The thermal emission rate is expressed as

$$\Gamma_{\text{Em}} = \frac{C_{\text{NR}} N_s}{g_v} \exp\left(-\frac{\Delta E_i}{k_B T}\right) , \tag{2.38}$$

where N_s is the density of states of the valence or conduction band, g_v is the valley degeneracy, and ΔE_i is the ionization energy of the defect. The exponential term in Eq. 2.38 strongly suppresses thermal emission from defect states deep in the band gap. Since thermal emission would destroy the quantum state, having defect states far from the band edges is a desired property for quantum defects [9].

Defect Auger

Defect Auger [3] is another type of nonradiative capture process. However, unlike a multiphonon emission process, defect Auger gives the excess energy to a second free carrier through the screened Coulomb interaction. In this way, defect Auger depends on the carrier density squared and can become more important than capture via multiphonon emission at higher carrier densities. Four distinct defect Auger processes can be identified (Fig. 2.3). The Auger coefficient for each of these processes is given by

$$T_1 = \frac{2\pi}{\hbar}\frac{1}{n^2}\sum_{\mathbf{1,2,4}} f_{\mathbf{1}} f_{\mathbf{2}}(1-f_{\mathbf{4}})|M_{\mathbf{12}d\mathbf{4}}|^2\delta(\varepsilon_{\mathbf{1}}+\varepsilon_{\mathbf{2}}-\varepsilon_d-\varepsilon_{\mathbf{4}})\,, \tag{2.39}$$

$$T_2 = \frac{2\pi}{\hbar}\frac{1}{p^2}\sum_{\mathbf{1,2,4}} (1-f_{\mathbf{1}})(1-f_{\mathbf{2}})f_{\mathbf{4}}|M_{\mathbf{12}d\mathbf{4}}|^2\delta(\varepsilon_{\mathbf{1}}+\varepsilon_{\mathbf{2}}-\varepsilon_d-\varepsilon_{\mathbf{4}})\,, \tag{2.40}$$

$$T_3 = \frac{2\pi}{\hbar}\frac{1}{np}\sum_{\mathbf{1,2,4}} f_{\mathbf{1}}(1-f_{\mathbf{2}})(1-f_{\mathbf{4}})|M_{\mathbf{1}d\mathbf{24}}|^2\delta(\varepsilon_{\mathbf{1}}+\varepsilon_d-\varepsilon_{\mathbf{2}}-\varepsilon_{\mathbf{4}})\,, \tag{2.41}$$

$$T_4 = \frac{2\pi}{\hbar}\frac{1}{np}\sum_{\mathbf{1,2,4}} f_{\mathbf{1}}(1-f_{\mathbf{2}})f_{\mathbf{4}}|M_{\mathbf{2}d\mathbf{41}}|^2\delta(\varepsilon_{\mathbf{2}}+\varepsilon_d-\varepsilon_{\mathbf{4}}-\varepsilon_{\mathbf{1}})\,, \tag{2.42}$$

where $M_{ijkl} = \langle ij|\hat{W}|kl\rangle - \langle ij|\hat{W}|lk\rangle$ and $\hat{W}$ is the screened Coulomb interaction. d labels the defect state, and the bold integers are a composite index for the band index and spin of the bulk bands. $f_{\mathbf{i}}$ is the Fermi occupation factor for state $\mathbf{i}$. A first-principles evaluation of the defect Auger process is being developed [82].

Radiative Internal Transition

A radiative internal transition occurs between two localized defect orbitals and emits a photon in the process. The rate is given by a Fermi's golden rule expression based on the spontaneous emission process. The radiative transition rate is expressed

[3] Defect Auger is also commonly referred to as Impurity Auger.

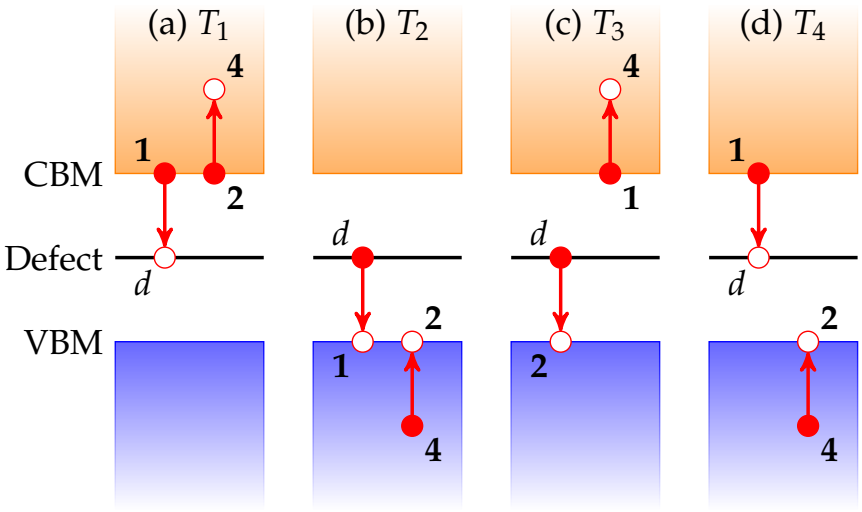

Figure 2.3: Schematic diagram for the defect Auger (a) T_1, (b) T_2, (c) T_3, and (d) T_4 processes. The conduction band is shown in orange, and the valence band is shown in blue. The conduction-band minimum (CBM) and valence-band maximum (VBM) are labeled. A single defect state is shown by a black line in the band gap. Occupied states are depicted with filled red circles, and unoccupied states are shown with unfilled circles.

as [76, 79]

$$\Gamma_{\text{Rad}} = \frac{n_r E_{\text{ZPL}}^3 \mu^2}{3\pi\epsilon_0 c^3 \hbar^4} , \tag{2.43}$$

where n_r is the index of refraction, E_{ZPL} is the zero-phonon line energy, and μ is the transition dipole moment. The transition rate is straightforward to evaluate from first principles and is applied to the boron dangling-bond defect in h-BN in Chapter 7.

Absorptive Internal Transition

In an absorptive internal transition, a photon excites an electron between two localized defect orbitals. Similar to photoionization, the rate for an absorptive internal transition is [77]

$$\Gamma_{\text{Abs}} = n_\nu v_\nu \, \sigma_{\text{Abs}}(\hbar\omega_\nu) . \tag{2.44}$$

where $\sigma_{\text{Abs}}(\hbar\omega)$ is the absorption cross section and is given by [77, 78]

$$\sigma(\hbar\omega) = g\frac{4\pi^2\alpha}{n_r}\hbar\omega\,|\mu|^2\delta(\hbar\omega - E_{\text{ZPL}})\,, \tag{2.45}$$

where g is the orbital degeneracy. The absorption cross section was evaluated by Razinkovas *et al.* for the NV center in diamond [78].

Nonradiative Internal Transition

Nonradiative internal transitions are similar to nonradiative capture but occur between two localized defect orbitals. The expression for the nonradiative transition rate takes a similar form to the that of the capture coefficient [23, 79]:

$$\Gamma_{\text{NR}} = \frac{2\pi}{\hbar}gW_{if}^2\sum_m w_m\sum_n |\langle\chi_{im}|\hat{Q} - Q_0|\chi_{fn}\rangle|^2\delta(\Delta E + m\hbar\Omega_i - n\hbar\Omega_f)\,. \tag{2.46}$$

However, an important difference is the absence of the volume V in the expression. As a result, input parameters that would lead to a negligible capture coefficient can lead to a sizable internal transition rate. (In other words, relatively weak electron-phonon coupling can still lead to an internal transition rate that cannot be ignored.) A first-principles evaluation of Eq. 2.46 can be performed with the `Nonrad` code [22, 24]; however, the applicability of the single-mode approximation for nonradiative internal transitions has not been assessed. The single-mode approximation works best when electron-phonon coupling is strong [83], which is not always the case for nonradiative internal transitions. Furthermore, coupling to a symmetric phonon mode, which the single-mode approximation corresponds to, may be forbidden by symmetry for nonradiative internal transitions.

Intersystem Crossing

The transitions considered to this point were those in which the total spin of the defect is conserved. Intersystem crossing is an internal transition that is nonradiative and involves a change in the total spin of the defect. In contrast to the nonradiative internal transition, spin-orbit coupling mediates the transition. The intersystem crossing rate is given by [79]

$$\Gamma_{\mathrm{ISC}} = \frac{2\pi}{\hbar} \sum_{m,n} w_m \left|\hat{h}_{\mathrm{SOC}}\right|^2 \left|\langle \chi_m | \chi_n \rangle\right|^2 \delta(m\hbar\Omega_i - n\hbar\Omega_f + \Delta E) \,, \tag{2.47}$$

where $\hat{h}_{\mathrm{SOC}}$ is the spin-orbit coupling matrix element. A first-principles evaluation of the intersystem crossing rate has been applied [84, 85]; Thiering *et al.* calculated the intersystem crossing rates for the NV center in diamond, but relied on empirical parameters to match experiment [84]. In Ref. [85], a first-principles approach was applied transition-metal defects in h-BN, but mixed computational methods were necessary. Similar to nonradiative internal transitions, the single-mode approximation has not been assessed.

Optical Dynamics

Given the first-principles evaluation of the above transition rates, the temporal response of the quantum defect to optical excitation can be determined. The optical dynamics depend sensitively on the interplay of the possible transitions and their relative magnitudes. We can solve for the full quantum dynamics using the Lindblad master equation approach [86]; however a semiclassical approximation is sufficient for the behavior of quantum defects. In the semiclassical approach, the individual transitions are treated quantum-mechanically, while the dynamics are treated with a

classical master equation [87–89],

$$\frac{d}{dt}\mathbf{P} = \mathbf{R} \cdot \mathbf{P} \,, \tag{2.48}$$

where $\mathbf{P}(t) = \{p_0(t), p_1(t), \dots\}$ is the vector of time-dependent state populations $p_i(t)$, and $\mathbf{R}$ is the rate matrix that describes the possible transitions. $\mathbf{P}$ has length N, and $\mathbf{R}$ has size $N \times N$, where N is the number of quantum states being considered. R_{ij} is the transition rate from state j to state i, and the diagonal matrix elements $R_{ii} = -\sum_j R_{ji}$ to conserve probability.

Equation 2.48 may then be solved numerically for the initial condition given by $\mathbf{P}(0) = \{1, 0, \dots\}$, where we've assumed the first state is the ground state. The solution gives us the population of each state as a function of time. In typical experiments, the second-order photon autocorrelation function $g^{(2)}(\tau)$ is measured. Assuming we have seen a photon, $g^{(2)}(\tau)$ would be given by the normalized population of the emissive state. Thus, we may calculate

$$g^{(2)}(\tau) = \frac{p_n(\tau)}{p_n(\infty)} \,, \tag{2.49}$$

where n is the index of the emissive quantum state and the population is normalized at infinity.

A first-principles evaluation of the optical dynamics is predicated on the ability to predict each transition from first principles. As highlighted above, this is in principle possible, although some approximations and assumptions are still necessary. The optical dynamics of single-photon emitters in hexagonal boron nitride are investigated in Chapter 8, supplemented by experimental information.

Chapter 3

Nonrad: Computing Nonradiative Capture Coefficients from First Principles

3.1 Introduction

In semiconducting or insulating material, any injected or excited carriers that do not leave the material eventually decay through radiative or nonradiative recombination. Point defects provide a path for nonradiative transitions, with important implications for device performance. In optoelectronic devices, point defects allow carriers to recombine nonradiatively through the Shockley-Read-Hall (SRH) process [90]. SRH recombination limits the efficiency of light-emitting diodes, lasers, and photovoltaic cells, transferring the excitation energy into lattice vibrations or, in other words, heat. Similarly, point defects may act as charge traps or recombination centers in electronic devices such as transistors, degrading performance. For quantum

defects, nonradiative transitions enable manipulations of the spin and determine the quantum efficiency of their optical interfaces. Control of nonradiative recombination is of paramount importance for enhancing the performance of devices.

Many authors have contributed to the theoretical foundations of nonradiative processes in solids [91–95], dating back several decades. The work of Henry and Lang [94] was particularly influential; it used a semi-classical description and empirical parameters to ascertain the temperature dependence of the nonradiative rates. While these early works were limited in predictive power, they provided the foundations for a full treatment of the capture process. Indeed, their limitation was largely due to the fact that they did not take into account the specific electronic and vibronic structure of a given point defect.

First-principles calculations based on state-of-the-art hybrid density functional theory provide an accurate description of the electronic structure of point defects [42] and a rigorous framework for incorporating atomistic insight into the nonradiative capture process. The first-principles approach for point defects was discussed in Sec. 2.6. A formalism for computing nonradiative capture rates from first principles was developed by Alkauskas *et al.* [23]: nonradiative recombination rates are computed quantum-mechanically using Fermi's golden rule within the static-coupling approximation. While the formalism is general, the full multidimensional treatment is computationally extremely expensive. Alkauskas *et al.* demonstrated that a one-dimensional approximation based on a single phonon mode (known as the accepting mode [95]) yields very good results, particularly for defects with strong electron-phonon coupling. Good agreement was demonstrated both with experiment [23, 96] and with multidimensional calculations [97, 98].

Here, we present `Nonrad` [24], an open-source Python implementation for the

computation of nonradiative capture coefficients based on the formalism of Alkauskas *et al*. `Nonrad` relies on standard Python libraries such as NumPy [99] and SciPy [100] to perform calculations of the nonradiative capture coefficients, as well as Pymatgen [101] to interface with common first-principles codes. In addition, `Nonrad` provides various utilities for preparing and parsing configuration coordinate diagrams. These utilities facilitate the process of generating input files for these calculations. Phonon integrals are evaluated using an analytic formula for the overlap between two displaced harmonic oscillator wavefunctions or by direct numerical integration of the analytic wavefunctions.

In addition to the implementation of the approach described in Ref. [23], the present work includes three important extensions of the methodology: (i) a method for evaluating electron-phonon matrix elements within the projector augmented wave (PAW) formalism [65], (ii) an interpolation scheme to obtain a smooth spectral function, and (iii) numerical evaluation of the Sommerfeld parameters. The interpolation scheme of extension (ii) is an alternative to replacing the Dirac delta functions with Gaussians, which mimics broadening effects on the energy conservation condition; our scheme provides consistent lineshapes without any tuning parameters. In extension (iii), we remove the approximation associated with using an analytic form for the Sommerfeld parameter. We show that this approximation is valid only over a limited range of temperatures, and instead numerically evaluate the integral form of the Sommerfeld parameter. In total, `Nonrad` provides a powerful and easy-to-use interface for the evaluation of nonradiative capture coefficients and will enable researchers to reliably investigate nonradiative capture in a range of materials.

3.2 Implementation

3.2.1 Basic Theory

Calculations of nonradiative capture begin with accurate modeling of the point defect using the standard methodology [42] in which charged point defects are studied within a supercell and finite-size corrections are included [70] (discussed in Sec. 2.6). The nonradiative capture coefficient C describes capture of a carrier at the band edge onto the defect and is given by Eq. 2.37. The summations in Eq. 2.37 are over the quantum numbers of the special phonon mode known as the accepting mode [95]. This mode corresponds to the mass-weighted configuration coordinate Q used to construct the configuration coordinate diagram in Fig. 3.1. We define ΔQ as the difference in the equilibrium geometries of the initial and final state along this configuration coordinate; it is given by

$$(\Delta Q)^2 = \sum_I M_I |\mathbf{R}_{I,i} - \mathbf{R}_{I,f}|^2 \,, \tag{3.1}$$

where I labels the atomic sites, M_I is the atomic mass of site I, and $\mathbf{R}_{I,i/g}$ are the coordinates of the Ith site in the initial (i) or final (f) state. Such diagrams describe the change in energy as the atomic coordinates change for a given charge state of a defect. In Eq. 2.37, Q_0 is the atomic configuration used as the starting point for the perturbative expansion. This can be chosen to correspond to the equilibrium geometry of either the initial or the final state, as will be discussed in Sec. 3.3.4.

In this Chapter, we focus on the case where the initial state corresponds to a delocalized band-edge state. In this case, V is the volume of the supercell used for the simulation. The `Nonrad` code, however, is equally applicable to the case where the initial state is a localized excited state of the defect. In that case, V and the scaling

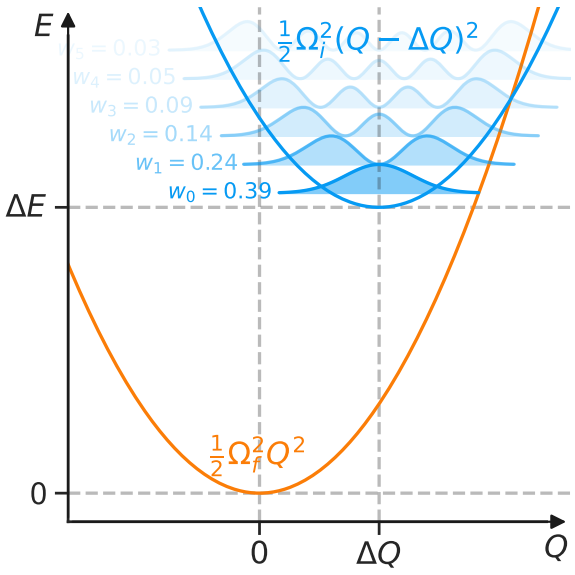

Figure 3.1: A schematic configuration coordinate diagram. The blue parabola corresponds to the initial state with a phonon frequency Ω_i centered at the equilibrium geometry, defined to be $Q = \Delta Q$. The orange parabola corresponds to the final state with frequency Ω_f and equilibrium geometry $Q = 0$. For the initial state, harmonic oscillator probability densities are shown, offset by the energy of the state. The opacity of the probability densities correspond to the thermal occupation of each state w_m at a temperature $k_B T = 2\hbar\Omega_i$.

function f (discussed below) should both be set equal to 1, and a rate is obtained (in units of s^{-1}) as opposed to a capture coefficient (in units of $cm^3 s^{-1}$).

The phonon matrix elements $\langle \chi_{im} | \hat{Q} - Q_0 | \chi_{fn} \rangle$ are evaluated within the `Nonrad` code by writing them in terms of wavefunction overlaps through the ladder operators $\hat{Q} = \sqrt{\hbar/2\Omega}(\hat{a}^\dagger + \hat{a})$, where $\hat{a}^\dagger$ and $\hat{a}$ are the raising and lowering operators. The resulting overlaps are calculated using either the analytic formula of Zapol [102] or by direct numerical integration of the harmonic oscillator wavefunctions, which is the default. These two approaches produce numerically identical results, but differ in their computational cost. For small vibronic quantum numbers, the analytic formula is faster, while numerical integration becomes faster in the opposite limit.

The scaling function f in Eq. 2.37 accounts for two contributions: (i) the Coulombic interaction between the defect and delocalized carrier if the defect is charged, and (ii) the perturbation of the band-edge wavefunction due to the interaction with the charged defect level in a finite-size supercell. In previous works, a more general form of the scaling function was defined (see Eq. 14 in Ref. [23]); the more general form reduces to those described below for typical simulation conditions. Contribution (i) has been described in the literature and is known as the Sommerfeld parameter [75]. The Sommerfeld parameter may be calculated using the `sommerfeld_parameter` function available in the `Nonrad` code. We examine the accuracy of the commonly used analytic form of the Sommerfeld parameter in Sec. 3.2.4. The effect of contribution (ii) can be estimated by comparing the band-edge wavefunction in the supercell to a homogeneous distribution, where the integrated radial charge density goes as $(4/3)\pi R^3/V$. If we define α as the ratio of the integrated radial distribution of the band-edge charge density to the homogeneous case, then the resulting scaling of the capture coefficient is α^{-1}. The procedure for calculating this contribution is encapsulated in the `charged_supercell_scaling` function in the `Nonrad` code. The final scaling function is the product of contributions (i) and (ii), and we set it to 1 for capture of a carrier in the neutral charge state with the electron-phonon matrix element evaluated in a neutral cell.

The electron-phonon matrix element W_{if} needs to be computed from first principles. The PAW pseudopotential formalism has become a prominent framework for computation because it provides a large reduction in computational complexity while still retaining an effective full-potential wavefunction, albeit with the core electrons frozen. To compute matrix elements within the PAW formalism, the contribution from the overlap operator needs to be accounted for. In Sec. 3.2.2, we present a linear re-

sponse theory for evaluating the electron-phonon matrix elements within the PAW formalism. Finally, we examine the common practice of replacing the energy-conserving delta functions in Eq. 2.37 with Gaussians and show that it may introduce significant errors in the resulting capture coefficients. We propose an alternative scheme in Sec. 3.2.3.

3.2.2 PAW Formalism

We presented an overview of the PAW formalism in Sec. 2.5; here we derive the electron-phonon coupling matrix element within this formalism. We begin by writing the matrix element in terms of the pseudo-wavefunctions:

$$W_{if} = \langle \psi_i | \partial_Q \hat{H} | \psi_f \rangle \approx \langle \tilde{\psi}_i | \partial_Q \hat{\tilde{H}} - \epsilon_f \partial_Q \hat{\tilde{S}} | \tilde{\psi}_f \rangle \ , \tag{3.2}$$

where ψ_j is the single-particle wavefunction and $\hat{H}$ is the full-potential Kohn-Sham Hamiltonian. $\hat{\tilde{H}}$ is the Kohn-Sham Hamiltonian for the pseudo-wavefunctions after applying the PAW transformation, $\hat{\tilde{S}}$ is the overlap matrix arising from the non-orthogonality of the pseudo-wavefunctions, and ϵ_j is the energy eigenvalue corresponding to the pseudo-wavefunction $\tilde{\psi}_j$. $\tilde{\psi}_i$ and $\tilde{\psi}_f$ are taken from the same calculation (the static approximation, Ref. [23]). The right-hand side of the equation is obtained by first performing the PAW transformation ($\hat{\mathcal{T}} \tilde{\psi}_j = \psi_j$), then using the PAW completeness relation, and finally taking derivatives. This results in an approximation, where the term $\langle \tilde{\psi}_i | \hat{\mathcal{T}}^\dagger \partial_Q \hat{\mathcal{T}} | \tilde{\psi}_f \rangle$ is assumed to be negligible. Chaput and coworkers [103] recently suggested an alternative approach, which first takes the derivative on the left-hand side, then performs the PAW transformation, and finally uses the completeness relation. The relation between these two approaches is discussed elsewhere [104].

Equation 3.2 is unwieldy to evaluate directly, and a more tractable form may be derived from linear response theory. The effective Kohn-Sham equation for the pseudo-wavefunctions,

$$(\hat{\tilde{H}} - \epsilon_f \hat{\tilde{S}})\,|\tilde{\psi}_f\rangle = 0\,, \tag{3.3}$$

is expanded to linear order in the perturbation:

$$\left[(\hat{\tilde{H}} + \partial_Q \hat{\tilde{H}}) - (\epsilon_f + \partial_Q \epsilon_f)(\hat{\tilde{S}} + \partial_Q \hat{\tilde{S}})\right]|\tilde{\psi}_f + \partial_Q \tilde{\psi}_f\rangle = 0\,. \tag{3.4}$$

Collecting terms that are linear in the perturbation and equating them to 0 gives

$$(\hat{\tilde{H}} - \epsilon_f \hat{\tilde{S}})\,|\partial_Q \tilde{\psi}_f\rangle = -(\partial_Q \hat{\tilde{H}} - \epsilon_f \partial_Q \hat{\tilde{S}})\,|\tilde{\psi}_f\rangle + (\partial_Q \epsilon_f)\hat{\tilde{S}}\,|\tilde{\psi}_f\rangle\ . \tag{3.5}$$

Finally, we multiply by $\langle\tilde{\psi}_i|$, obtaining

$$\langle\tilde{\psi}_i|\hat{\tilde{H}} - \epsilon_f \hat{\tilde{S}}|\partial_Q \tilde{\psi}_f\rangle = -\langle\tilde{\psi}_i|\partial_Q \hat{\tilde{H}} - \epsilon_f \partial_Q \hat{\tilde{S}}|\tilde{\psi}_f\rangle + (\partial_Q \epsilon_f)\langle\tilde{\psi}_i|\hat{\tilde{S}}|\tilde{\psi}_f\rangle \tag{3.6}$$

or

$$(\epsilon_f - \epsilon_i)\langle\tilde{\psi}_i|\hat{\tilde{S}}|\partial_Q \tilde{\psi}_f\rangle = \langle\tilde{\psi}_i|\partial_Q \hat{\tilde{H}} - \epsilon_f \partial_Q \hat{\tilde{S}}|\tilde{\psi}_f\rangle\ , \tag{3.7}$$

where we have used Eq. 3.3 and the orthogonality relation $\langle\tilde{\psi}_i|\hat{\tilde{S}}|\tilde{\psi}_j\rangle = \delta_{ij}$. We can now plug this into Eq. 3.2 to arrive at the final form for the electron-phonon matrix element:

$$W_{if} = (\epsilon_f - \epsilon_i)\langle\tilde{\psi}_i|\hat{\tilde{S}}|\partial_Q \tilde{\psi}_f\rangle\ . \tag{3.8}$$

In practice, Eq. 3.8 is evaluated by computing the slope of $\langle\tilde{\psi}_i(0)|\hat{\tilde{S}}(0)|\tilde{\psi}_f(Q)\rangle$ as a function of Q. This evaluation is in the spirit of finite differences, for which an arbitrary phase factor may present itself. However, the matrix element only enters as a modulus squared, for which we can focus on the magnitude of the matrix element, without the need to specifically address the phase factor.

Other methods for evaluating the electron-phonon coupling within the PAW formalism have been described in the literature, for instance in Refs. [103] and [104] and in Appendix C of Ref. [105]; however, they rely on computing structure factors resulting from the displacement of the PAW spheres or implementing the more involved Eq. 3.2. The method described here is straightforward, very efficient and has been implemented in the VASP code version 5.4.4, as well as version 6.

3.2.3 Broadening of the Delta Functions

The delta functions in Eq. 2.37 impose energy conservation on the vibronic transitions. In reality, the delta functions are too restrictive: various mechanisms act to broaden the energies of the transitions, producing a continuous spectral function. In solids the dominant sources of broadening are random internal fields and the finite lifetime of the states involved in the transition, which leads to energy uncertainty [79]. To simulate this broadening, the delta functions are typically replaced with Gaussians, whose width is characterized by a smearing parameter. Within the one-dimensional approximation, the broadening is relatively large because it needs to reflect the contributions from many phonon modes; unfortunately, this renders the results highly sensitive to the choice of the smearing parameter. This effect was examined in the case of luminescence lineshapes within the single-phonon-mode approximation [106]. In the context of nonradiative capture, this effect can be understood by examining the vibrational lineshape function, defined as [95]:

$$G_m(\omega) = \sum_n |\langle \chi_{im} | \hat{Q} - Q_0 | \chi_{fn} \rangle|^2 \delta(\omega + m\Omega_i - n\Omega_f) \ . \tag{3.9}$$

When we replace the delta function in Eq. 3.9 with a Gaussian, we are left with conflicting requirements for the choice of the smearing parameter σ. On the one hand,

if σ is too small, the lineshape function will not be smooth and will perform barely better than the delta functions. Too large a value for σ, on the other hand, results in the "tails" of the Gaussians from various transitions adding up and creating an artificial enhancement of the function at high and low energies. These effects are illustrated in Fig. 3.2, where the lineshape function for the lowest transition $G_0(\omega)$ is shown for various choices of σ. In Fig. 3.2, we have assumed that the phonon frequencies are identical in the initial and final state ($\Omega_i = \Omega_f = \Omega$), and that the Huang-Rhys factor S, a dimensionless parameter quantifying the electron-phonon coupling strength, is an integer. Under these assumptions, the lineshape function can be obtained from the Pekarian function [107]:

$$G_0(\omega) = \sum_n \frac{e^{-S} S^n}{n!} \delta(\omega - n\Omega) \, . \tag{3.10}$$

To obtain a continuous function, we treat n as a continuous variable. We use the identity $n! = \Gamma(n+1)$, replace the summation over n with an integral, and integrate to obtain

$$G_0(\omega) = \frac{e^{-S} S^{\omega/\Omega}}{\Gamma(\omega/\Omega + 1)} \, . \tag{3.11}$$

This function is shown for comparison in Fig. 3.2.

Our solution is to use cubic spline interpolation to produce a smooth lineshape function, $g_m(\omega)$. In practice, the function $g_m(\omega)$ is obtained by interpolating the data points given by $\left(n\Omega_f - m\Omega_i, |\langle \chi_{im} | \hat{Q} - Q_0 | \chi_{fn} \rangle|^2\right)$. The use of cubic splines ensures the smoothness of g_m and removes the need for a smearing parameter. To ensure consistency between the interpolated function and the true lineshape, we normalize g_m such that

$$\int d\omega \, g_m(\omega) = \int d\omega \, G_m(\omega) = \sum_n |\langle \chi_{im} | \hat{Q} - Q_0 | \chi_{fn} \rangle|^2 \, . \tag{3.12}$$

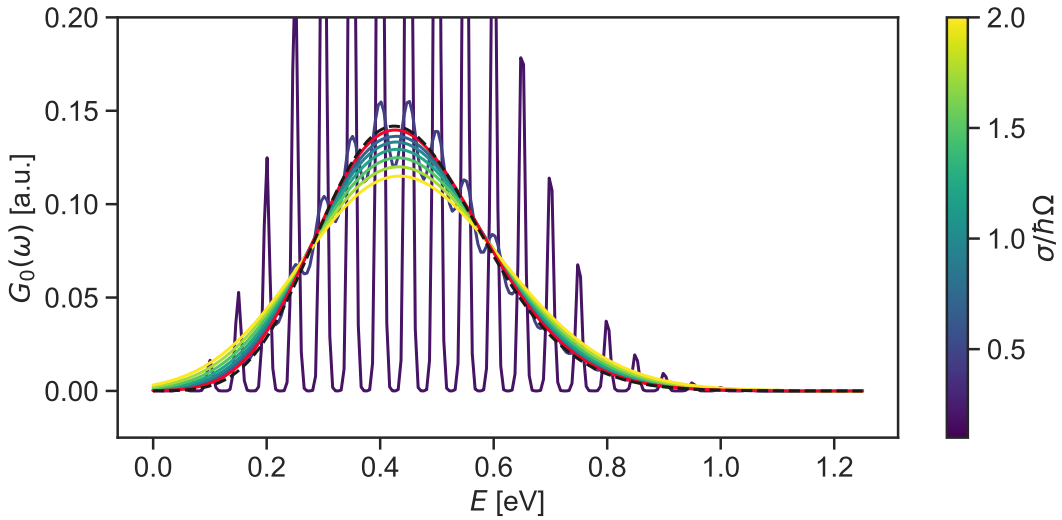

Figure 3.2: The lineshape function G_0 for $\hbar\Omega = 0.05$ eV and with Huang-Rhys factor $S = 8$. In the figure, the black, dashed line comes from the analytic form of the lineshape function (Eq. 3.11) from the Pekarian function [107]. The red line corresponds to the lineshape function resulting from our proposed interpolation scheme. The remaining lines are generated using Gaussians for the delta functions, with the color corresponding to the smearing parameter σ. If the smearing parameter is too small, the lineshape function is not sufficiently smooth. For too large a smearing parameter, the tails of the Gaussians add up, which can be seen in the low- and high-energy portions of the lineshape function.

The proposed interpolation scheme provides a reliable representation of the lineshape function, reproducing Eq. 3.11 for the conditions stated above (see Fig. 3.2).

The method for treating the delta functions impacts not only the lineshape function but also the nonradiative capture coefficient. A comparison of the capture coefficient obtained with Gaussian smearing and with the new interpolation scheme is shown in Fig. 3.3. From the figure, it is clear that use of the interpolation scheme prevents erroneous values in the capture coefficient.

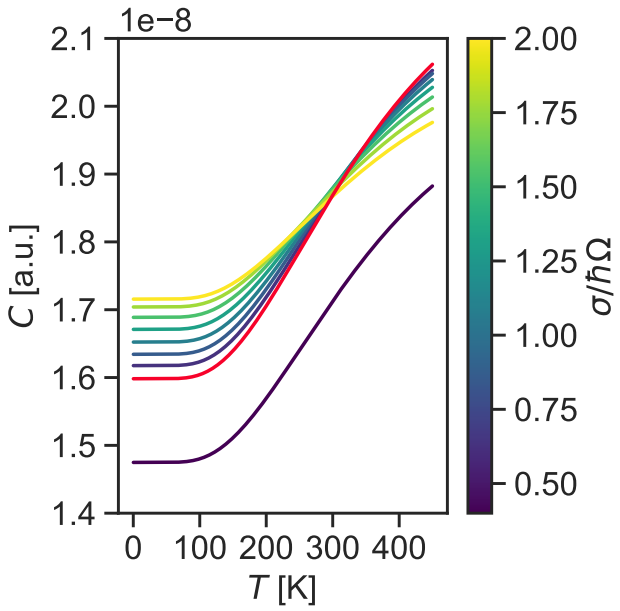

Figure 3.3: Capture coefficient for the case of $\hbar\Omega = 0.05$ eV and with Huang-Rhys factor $S = 8$. The red line corresponds to the capture coefficient determined using the proposed interpolation scheme. The remaining lines are generated using Gaussians to replace the delta functions in Eq. 2.37, with the color corresponding to the smearing parameter σ. Large deviations are seen for the Gaussian scheme.

3.2.4 Sommerfeld Parameter

The Sommerfeld parameter describes the enhancement or suppression of a delocalized wavefunction near a charge. When a carrier is captured by a charged defect, the Sommerfeld parameter must be included to scale the capture coefficient correctly. Typically, an analytic form for the Sommerfeld parameter is used, given by [75]:

$$s(T) = \begin{cases} \frac{4}{\sqrt{\pi}}\left[\frac{Z^2\theta_b}{T}\right]^{1/2} & Z < 0 \\ \frac{8}{\sqrt{3}}\left[\frac{Z^2\theta_b}{T}\right]^{2/3} \exp\left(-3\left[\frac{Z^2\theta_b}{T}\right]^{1/3}\right) & Z > 0 \end{cases}, \tag{3.13}$$

where $\theta_b = m_b e^4/32k_B\epsilon_0^2\hbar^2$ is a temperature parameter, e is the fundamental charge, m_b is the band effective mass, ϵ_0 is the static dielectric constant, k_B is the Boltzmann constant, and Z is the ratio of the defect charge to the carrier charge ($Z > 0$ corre-

sponds to a repulsive center).

In deriving Eq. 3.13, the Sommerfeld parameter is first obtained as a function of momentum and written as

$$s(\boldsymbol{k}) = -\frac{2\pi Z}{a_b|\boldsymbol{k}|}\frac{1}{1-e^{2\pi Z/a_b|\boldsymbol{k}|}}\,, \tag{3.14}$$

where $a_b = 4\pi\epsilon_0\hbar^2/m_b e^2$ is an effective Bohr radius. Temperature averaging is then performed to give

$$s(T) = \frac{\int_0^\infty d|\boldsymbol{k}|\,4\pi|\boldsymbol{k}|^2\,s(\boldsymbol{k})e^{-\hbar^2|\boldsymbol{k}|^2/2m_b k_B T}}{\int_0^\infty d|\boldsymbol{k}|\,4\pi|\boldsymbol{k}|^2\,e^{-\hbar^2|\boldsymbol{k}|^2/2m_b k_B T}}\,. \tag{3.15}$$

At this point, an approximation is necessary to obtain the analytic form given in Eq. 3.13. It is assumed that $|\boldsymbol{k}| \ll 2\pi|Z|/a_b$, allowing to write $s(\boldsymbol{k})$ in Eq. 3.14 as

$$s(\boldsymbol{k}) \approx \frac{2\pi|Z|}{a_b|\boldsymbol{k}|}\begin{cases} 1 & Z<0 \\ e^{-2\pi Z/a_b|\boldsymbol{k}|} & Z>0 \end{cases}\,. \tag{3.16}$$

The integrals in Eq. 3.15 may then be evaluated analytically to give the form of $s(T)$ in Eq. 3.13.

While the analytic form is simple to work with, the assumptions made in its derivation may not be valid for the temperatures where it is applied. Instead of making the approximation above, Eq. 3.15 can be evaluated numerically to give a more exact value for the Sommerfeld parameter. A comparison of the analytic form and direct numerical evaluation of the Sommerfeld parameter for the example of electron capture at a defect in GaN is shown in Fig. 3.4. In the case of a repulsive interaction, the analytic form leads to errors exceeding 15% at high temperature; even at room temperature, an error of 7.7% is made. For attractive interactions, the errors are less severe, only surpassing 2% at high temperatures. For the implementation in `Nonrad`, direct nu-

merical integration of the Sommerfeld parameter is utilized, with the analytic form provided for comparison.

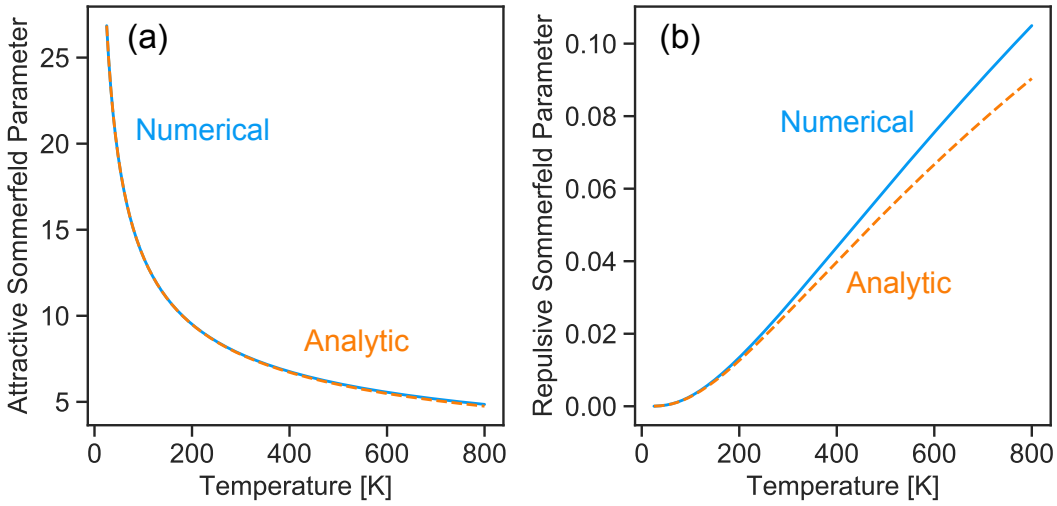

Figure 3.4: The Sommerfeld parameter in the (a) attractive and (b) repulsive cases with the parameters of GaN ($m_b = 0.18$ and $\epsilon_0 = 8.9$). Blue solid lines correspond to the numerical integration of Eq. 3.15, and orange dashed lines correspond to the analytic form of Eq. 3.13. Significant deviations are apparent for the repulsive case.

3.3 Numerical Example

In this section, we provide an example calculation of the nonradiative capture rate for a well-studied defect system: a carbon atom substituting on a nitrogen site (C_N) in GaN. We show how the utilities provided by `Nonrad` can simplify the procedure. This information is also available as a Jupyter notebook [108] distributed with the `Nonrad` code.[1] While the example here is performed with the VASP code [109], we emphasize that the final evaluation of the capture coefficient relies only on the derived

[1] Accessible at https://github.com/mturiansky/nonrad/blob/master/notebooks/tutorial.ipynb

parameters that may be obtained from any first-principles code that implements a method to obtain the electron-phonon coupling.

3.3.1 Computational Details

Calculations of the capture coefficient are sensitive to the quality of the input parameters; therefore, highly accurate first-principles methods should be employed (summarized in Chapter 2). In this dissertation, we utilize density functional theory as implemented in version 5.4.4 of the VASP code [109] with the hybrid functional of Heyd, Scuseria, and Ernzerhof (HSE) [64]. For the present study, the HSE mixing parameter of 0.31 is chosen to yield a band gap ($E_g = 3.54$ eV) and lattice parameters ($a = 3.20$ Å and $c = 5.19$ Å) in agreement with the experimental values [110, 111]. Calculations are performed within the PAW formalism [65] with an energy cutoff of 400 eV. Ga d states are included in the core. The atomic configurations are relaxed until forces are below 5 meV/Å. A 96-atom supercell is used to simulate the defect: the 4-atom primitive cell is transformed to an 8-atom orthorhombic cell, and then a $3 \times 2 \times 2$ multiple of this orthorhombic cell produces the 96-atom supercell. A single special $\mathbf{k}$ point is used for the Brillouin-zone sampling [112] to obtain the atomic structure. Electron-phonon matrix elements are evaluated at the Γ point. With these choices, we find that in the neutral charge state the structure is distorted along one of the planar bonds; the C-Ga bond lengths are 1.97 Å (axial) and 2.03 Å, 2.00 Å, and 1.98 Å, compared to the N-Ga bulk values of 1.96 Å (axial) and 1.95 Å (planar). In the negative charge state, atomic displacements correspond to a breathing relaxation, with C-Ga bond lengths of 1.94 Å (axial) and 1.93 Å (planar).

Carrier capture involves the capture of a single carrier at a time, and therefore, will inevitably involve a magnetic defect configuration. As such, it is necessary to

include the effects of spin polarization in the defect calculation. For C_N, the negative charge state is non-magnetic, and the neutral charge state is magnetic with a doublet configuration.

3.3.2 Energetics

The formalism for performing point-defect calculations and extracting the relevant energetics was described in Sec. 2.6. The formation energy and transition level for the C_N defect in GaN are shown in Fig. 3.5(a). We find a $\varepsilon(0/-)$ value of 1.06 eV; this value differs slightly from previous work (1.02 eV) due to minor differences in the finite-size correction [23].

In this tutorial example, we will calculate the hole capture rate; for hole capture, the energy difference between the initial and the final state corresponds to the thermodynamic transition level, i.e., $\Delta E = \varepsilon(0/-)$. If we were considering electron capture, the energy difference should be taken with respect to the conduction-band minimum, i.e., $\Delta E = E_g - \varepsilon(0/-)$, where E_g is the band gap. ΔE is one input parameter to the `Nonrad` code.

3.3.3 Configuration Coordinate Diagram

The configuration coordinate diagram (CCD) in Fig. 3.5(b) not only provides a convenient illustration of the nonradiative capture process but also allows us to derive important input parameters for the `Nonrad` code. The CCD is prepared by linearly interpolating between the equilibrium structures of the two charge states involved in the nonradiative transition. These interpolated structures can be generated using the `get_cc_structures` function provided by `Nonrad`. The energy of each inter-

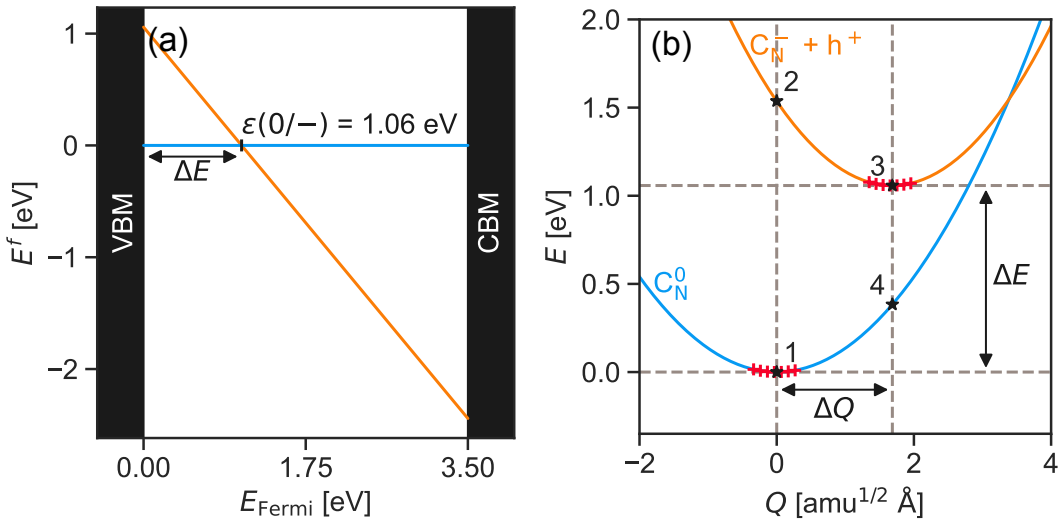

Figure 3.5: (a) Formation energy diagram and (b) configuration coordinate diagram for the C_N defect system. For the purposes of the plot, the formation energy of the neutral charge state is set to zero. In both figures, the blue line corresponds to the neutral charge state and the orange line to the negative charge state. The red crosses in (b) correspond to actual calculations at interpolated geometries. The coordinate corresponding to the equilibrium geometry of the final state has been set to zero. Points 1-4 in (b) label possible configurations for computing the electron-phonon coupling.

polated structure in the two charge states is plotted as a function of the generalized configuration coordinate Q. As mentioned in Sec. 3.2.1, this coordinate Q corresponds to the special phonon mode used in the one-dimensional approximation. Based on the potential energy surfaces plotted along Q, we can extract the phonon frequencies in the initial and final states.

Figure 3.5(b) for C_N was prepared using the utilities provided by `Nonrad`. The initial state corresponds to the C_N defect in the negative charge state and a hole in the valence band, and the final state corresponds to the defect in the neutral charge state. From the CCD, we extract the separation between the equilibrium structures along the configuration coordinate ΔQ in units of $\sqrt{\text{amu}}$ Å, using the `get_dQ` function. Also, we find the phonon frequencies in the initial and final states, $\Omega_{\{i,f\}}$ in eV, using the

`get_PES_from_vaspruns` and `get_omega_from_PES` functions. For this system, we obtain the values $\Delta Q = 1.69$ $\sqrt{\text{amu}}$ Å, $\hbar\Omega_i = 0.0375$ eV, and $\hbar\Omega_f = 0.0336$ eV.

3.3.4 Electron-Phonon Coupling

Next we compute the electron-phonon coupling using the implementation in VASP. We need to determine the atomic configuration Q_0 and charge state of the defect that will be used for computing the electron-phonon matrix elements; this gives us four points to choose from, labeled 1-4 in Fig. 3.5(b). Points 1 and 2 correspond to the equilibrium geometry of the final state ($Q = 0$), while points 3 and 4 correspond to the geometry of the initial state ($Q = \Delta Q$). For evaluating the electron-phonon coupling, it is important to identify an equilibrium geometry with a clearly identifiable defect state in the band gap. For C_N, a Kohn-Sham state associated with the defect state into which the hole is being captured can be clearly identified in the calculations performed for the geometry of the neutral charge state; therefore the geometry of the final state is a good choice for Q_0. We still need to choose between points 1 and 2; these points differ in the charge of the supercell. Point 1 is most convenient to use because we already have the wavefunctions available at displaced geometries from the preparation of the CCD. Furthermore, point 1 corresponds to the neutral charge state and avoids the complications that come with the use of a charged supercell. If we were to choose the negative charge state (point 2), we would need to include contribution (ii) of the scaling function to account for the interaction between the defect and the band-edge wavefunctions, as discussed in Sec. 3.2.1. Assuming the methods are consistently applied, this choice does not affect the accuracy of the resulting capture coefficient and should be made to facilitate calculation.

To prepare the VASP calculation of the overlaps for the electron-phonon coupling,

the `KPOINTS` and `POTCAR` files from the calculation of point 1 are used. The `INCAR` file should now contain `LWSWQ = True` and `ALGO = None`. The `WAVECAR` files for each of the displaced geometries around point 1 are then copied to `WAVECAR.qqq` and VASP is executed once for each available `WAVECAR.qqq` file (the `POSCAR` and `WAVECAR` files must correspond to the undisplaced geometries at point 1, and VASP will read both `WAVECAR` files to calculate $\langle\tilde{\psi}_i(0)|\hat{\tilde{S}}(0)|\tilde{\psi}_f(Q)\rangle$). These calculations will prepare a series of `WSWQ` files, one for each displacement. The `Nonrad` code provides the `get_Wif_from_WSWQ` function to process these files. In GaN, the VBM contains three (nearly degenerate) bands; we mean-square average over the electron-phonon matrix elements with these bands. This procedure yields the electron-phonon matrix element $W_{if} = 0.050$ eV amu$^{-1/2}$ Å^{-1} for the C_N defect.

3.3.5 Capture Coefficient

With the input parameters extracted above, we are now ready to compute the capture coefficient. We need to specify the volume of the supercell, which is 1100 Å^3, and the configurational degeneracy of the final state g, which takes a value of 4 here because there are 4 (approximately) equivalent bond directions the defect state may relax to. The `get_C` function returns the *unscaled* capture coefficient, i.e., we still need to determine f in Eq. 2.37. For this defect system, the hole is captured by the negatively charged defect, so there will be a long-range Coulombic attraction that needs to be accounted for with the Sommerfeld parameter [contribution (i) of the scaling function]. If we had calculated the electron-phonon coupling in the negative charge state (point 2), we would also need to account for the perturbation of the band-edge wavefunction by the charged defect here [contribution (ii) of the scaling function]. The resulting hole capture coefficient C_p and cross section σ are shown in Fig. 3.6(a)

and Fig. 3.6(b), respectively. The capture cross section $\sigma = C_p / \langle v \rangle$, where $\langle v \rangle$ is the average thermal velocity, may be obtained using the `thermal_velocity` function provided by `Nonrad`.

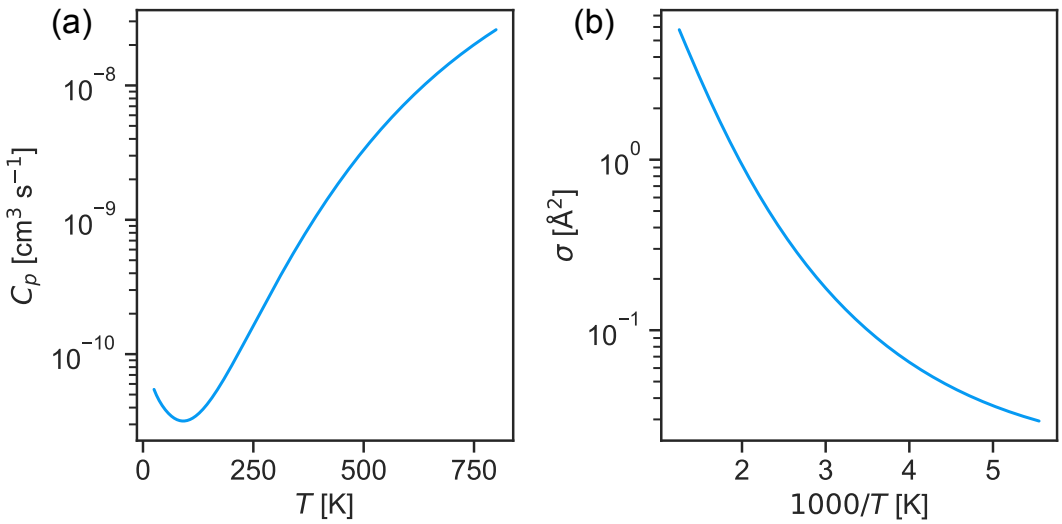

Figure 3.6: The nonradiative (a) capture coefficient C_p and (b) capture cross section σ for the C_N defect in GaN computed with the `Nonrad` code.

3.4 Summary

We have presented the `Nonrad` code [24] for the evaluation of nonradiative capture coefficients from first principles. `Nonrad` implements the methodology developed by Alkauskas *et al.* [23], which provides a quantum-mechanical description of the process of carrier capture at point defects. We also presented a straightforward and tractable method for computing electron-phonon coupling to linear order within the PAW formalism. Furthermore, we have shown that the process of replacing the Dirac delta functions by Gaussians can introduce significant errors; our proposed interpolation scheme provides reliable results, even at low temperatures. We also demonstrated

that the analytic form of the Sommerfeld parameter may be insufficiently accurate: instead, we implement direct numerical integration to avoid troublesome approximations. The `Nonrad` code provides a series of utilities, which facilitate the process of evaluating nonradiative capture coefficients. This work will enable researchers to perform reliable studies of nonradiative capture in a range of materials.

Permissions and Attributions

The content of Chapter 3 follows from work that has previously appeared in Computer Physics Communications (Ref. [22]). This work was performed in collaboration with Prof. Audrius Alkauskas, Manuel Engel, Prof. Georg Kresse, Dr. Darshana Wickramaratne, Dr. Jimmy-Xuan Shen, and Prof. Cyrus E. Dreyer. The derivation of Sec. 3.2.2 was initially provided by Manuel Engel and Prof. Georg Kresse.

Chapter 4

Prospects for *n*-Type Conductivity in Cubic Boron Nitride

4.1 Introduction

The combination of wide band gap, high breakdown field, high thermal conductivity, chemical stability, and attainable *n*-type and *p*-type doping has made cubic boron nitride (c-BN) a compelling candidate for applications ranging from power electronics to deep-ultraviolet optoelectronics, and as a host for single photon emitters [113–115]. Establishing control over the conductivity of c-BN is required to ensure that c-BN can be successfully deployed.

Experimental efforts to attain *n*-type doping in c-BN have relied on Si and S as candidate donors [116, 117]. Indeed, *n*-type doping with Si [116, 118] has led to electron concentrations up to 10^{18} cm^{-3} with an activation energy of 0.2 eV [118], while the use of S has been less successful, leading to material with carrier concentrations limited to 10^{14} cm^{-3} [117].

Impurities can also be incorporated unintentionally during the growth of c-BN, and it is unclear if they may be a source of conductivity. Carbon and oxygen have been reported to be unintentionally present during the growth of c-BN using molecular-beam epitaxy [119] and ion-beam-assisted deposition [118]. A range of other techniques have been employed to grow c-BN, as reviewed in Ref. [120] and may also lead to the unintentional incorporation of impurities. Lithium could also be incorporated, since lithiated BN is a common precursor for high-pressure, high-temperature growth [121]. Fluorine is another candidate, since thin-film growth of c-BN relies on fluorine for selective etching of the non-cubic phase [120]. Furthermore, there may be other donor dopants beyond those that have been explored to date. First-principles calculations provide a means to determine whether any of these impurities can in fact yield n-type conductivity in c-BN and to screen additional candidates.

Dopants that contribute to conductivity need to have high solubility under n-type conditions (quantified by a low formation energy), small ionization energies, and not be impacted by compensation, which would pin the Fermi level away from the conduction-band minimum (CBM). Compensation can be due to native point defects, such as boron vacancies that act as deep acceptors, or due to self-compensation. The latter can occur because of incorporation of the dopant on a competing site (e.g., Si_B acts as a donor but Si_N acts as a deep acceptor) or due to the formation of DX centers, which occur when a donor impurity undergoes a large lattice relaxation and captures two electrons, converting it to an acceptor [122].

Previous first-principles calculations have attempted to offer insight into these questions by investigating O, Si, Ge, S and C impurities [123–127] in c-BN. Si, Ge, and S were predicted to be shallow donors [125–127], while O and C lead to levels that are deep in the band gap [127]. These studies did not report any large lattice

relaxations that would be indicative of DX center formation. However, the accuracy of these previous studies is limited due to the reliance on functionals (such as the local density approximation or generalized gradient approximation) that underestimate the band gap [50], which can lead to errors in formation energies and thermodynamic transition levels [42]. In addition, such functionals fail to correctly describe charge localization [53], which can be essential for obtaining accurate atomic geometries, for instance in the case of DX centers.

In this Chapter, we use hybrid density functional theory (DFT) to address potential n-type dopants and compensating centers in c-BN. The hybrid functional overcomes the shortcomings of traditional functionals related to band-gap underestimation and charge localization. Donor doping in c-BN can be achieved by either substituting group-IV elements on the B site or group-VI elements on the N site. We examine a wide variety of donors: Si_B, Ge_B, C_B, S_N, Se_N and O_N, F_N and Li_i. Suitable n-type dopants have low formation energies under n-type conditions and small ionization energies (i.e., the positive charge state is stable over the majority of the band gap). We also assess compensation by native defects and self-compensation due to wrong-site incorporation or DX-center formation. Based on these criteria, we identify Si_B and O_N as potential n-type dopants. However, we find that boron vacancies act as deep acceptors. We discuss this result in the context of experimental growth methods and suggest that control of growth kinetics is necessary to enhance n-type conductivity in c-BN.

4.2 Methodology

We utilize the point-defect formalism for our calculations, which is summarized in Sec. 2.6. For the present study, the fraction of non-local Hartree-Fock exchange is set to 33%, and the energy cutoff for the plane-wave basis is set to 520 eV. These choices result in an indirect band gap of 6.26 eV and lattice parameter $a = 3.59$ Å, close to the experimental values of 6.36 eV [128] and $a = 3.62$ Å [129]. A plot of the band structure of c-BN can be found in Ref. [130]. The VBM at Γ is derived primarily from N p states while the CBM at X contains an equal admixture of B p states and N s states. The electron effective mass is anisotropic, with a value of 1.05 m_0 along X-Γ and 0.19 m_0 along X-K (with m_0 the free electron mass).

Defects and impurities are investigated in a 216-atom supercell, which is a $3 \times 3 \times 3$ multiple of the 8-atom conventional unit cell. Lattice parameters of the supercell are held fixed while the atomic coordinates are relaxed until forces are below 10 meV/Å. Brillouin-zone integration is performed with a single special point (1/4, 1/4, 1/4) [112]. Spin polarization is explicitly taken into account. Migration barriers are computed using the climbing-image nudged elastic band (NEB) method [131].

The formation energy E^f (Eq. 2.31) is the central quantity that determines the stability of native defects or impurities and their various charge states. The chemical potentials μ_i in Eq. 2.31 represent the abundance of the various species in actual growth or processing conditions [42]. We express the chemical potentials relative to the appropriate single-atom energy for a reference phase: $\mu_i = E_i + \Delta\mu_i$, where E_i is based on the energy of bulk B for μ_B and on the N_2 molecule for μ_N. Thermodynamic equilibrium then demands $\Delta\mu_\mathrm{B} + \Delta\mu_\mathrm{N} = \Delta H_f(\text{c-BN})$, where $\Delta H_f(\text{c-BN})$ is the formation enthalpy of cubic BN (calculated to be -2.79 eV). We define two extreme

limits that span the growth or processing conditions: (i) N-rich conditions are defined by $\Delta\mu_{\mathrm{N}} = 0$ and (ii) N-poor conditions are given by $\Delta\mu_{\mathrm{N}} = \Delta H_f(\text{c-BN})$. We will present results for these limiting conditions; results for intermediate conditions can be obtained from Eq. 2.31. For the chemical potentials of the impurities, we consider the secondary phases, specifically (with calculated ΔH_f values in parentheses): B_2S_3 (-2.43 eV), BSe_2 (-0.40 eV), B_2O_3 (-12.74 eV), BF_3 (-11.78 eV), Li_3BN_2 (-5.44 eV), $B_{13}C_2$ (-0.82 eV), Si_3N_4 (-9.12 eV), and Ge_3N_4 (-0.77 eV).

4.3 Results

We first examine the properties of Si, Ge, S, and Se, which are the main candidates for intentional doping of c-BN. The formation energies of these dopants incorporated on the B and N site are shown in Fig. 4.1. Due to the large size mismatch, $\mathrm{Ge_N}$ and $\mathrm{Se_B}$ are highly unfavorable and therefore not included here.

We find that $\mathrm{S_N}$, $\mathrm{Se_N}$ and $\mathrm{Ge_B}$ are stable only in the positive charge state over the entire range of the c-BN band gap, and therefore act as shallow donors. However, their formation energies are exceedingly high ($E^f > 5$ eV) under n-type conditions, rendering them unlikely to occur in appreciable concentrations in equilibrium. $\mathrm{S_B}$ is a deep triple donor with a high formation energy when the Fermi level is near the CBM.

For $\mathrm{Si_B}$, the formation energy is somewhat lower, but we find that the negative charge state is more stable for Fermi levels close to the CBM. In fact, $\mathrm{Si_B}$ forms a DX center, in which the $(+/0)$ charge-state transition level is above the $(0/-)$ level, leading to a negative U parameter [42] of -209 meV. Still, the $(+/-)$ transition level is only 0.11 eV below the CBM, which means that $\mathrm{Si_B}$ is a potential n-type dopant in c-BN. In the positive charge state, $\mathrm{Si_B}$ stays close to the substitutional site, and the neighboring

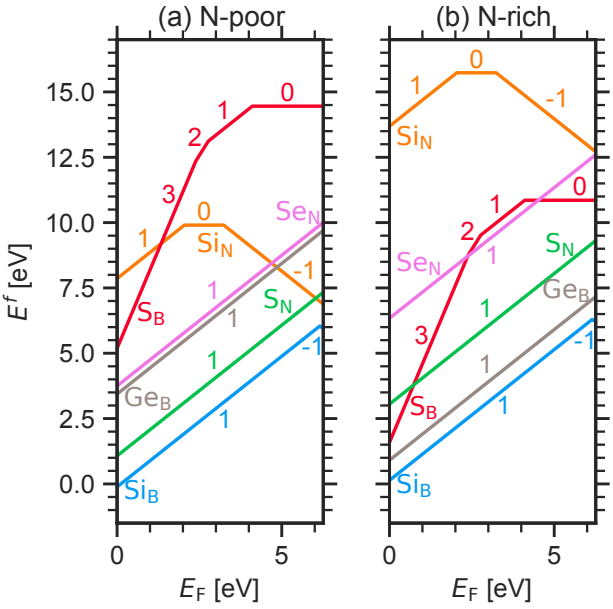

Figure 4.1: Formation energies for Si, Ge, S, and Se substitutional impurities for (a) N-poor and (b) N-rich conditions.

Si-N bonds expand by 8% compared to the equilibrium B-N bond length. In the negative charge state, two B atoms that are second-nearest neighbors to Si_B undergo a large lattice relaxation, forming a dimer [Fig. 4.2(a)]. This configuration corresponds to the "cation-cation bonded" DX state observed in GaAs [132]. Our calculated $(+/-)$ transition level is in reasonable agreement with the measured activation energy of 0.2 eV for Si-doped samples [118].

Next, we turn to impurities that may be incorporated unintentionally, including Li, F, C, and O. For Li and F [Fig. 4.3] we include configurations where the impurities are substituting either on the B or the N site, and also interstitials (Li_i and F_i), which are expected to be more favorable because of the small size of the impurities. Li_N and F_B are not included because the size mismatch makes them very unfavorable. Li_i is a shallow donor, but its formation energy is high under n-type conditions. Under

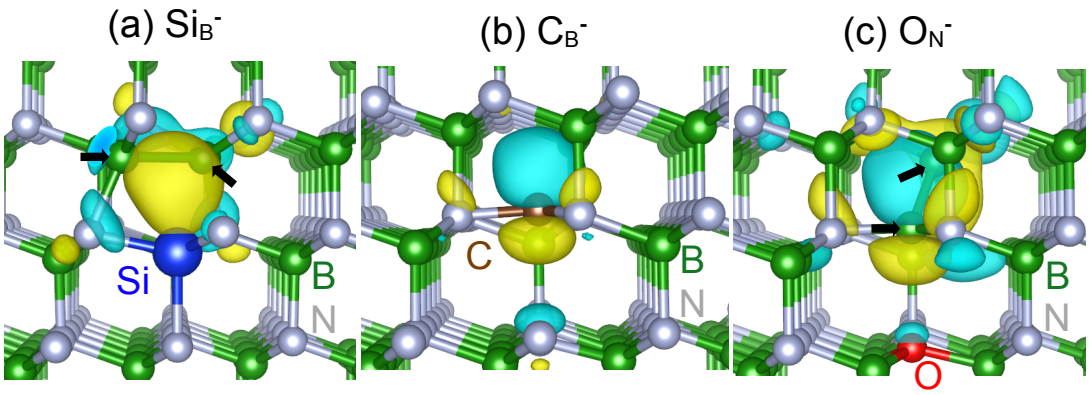

Figure 4.2: Atomic configuration of (a) Si_B^-, (b) C_B^-, (c) O_N^-. The charge density isosurface of the highest occupied molecular orbital for each impurity is shown. The isosurface corresponds to 10% of the maximal charge density and is colored by the sign of the wavefunction with blue and yellow indicating opposite signs. Pairs of black arrows point to boron atoms that have formed a dimer configuration.

those conditions, the formation energy of Li_B, which acts as a deep acceptor, is much lower. Li_B thus compensates and the Fermi level ends up far from the CBM. To avoid compensation by Li_B, Li_i could be introduced by diffusion; we compute a migration barrier for Li_i of only 1.86 eV. For F, we find F_N to be the most stable configuration, acting as a deep donor with a (+/0) level more than 1 eV below the CBM. Furthermore, its formation energy is high under n-type conditions.

The formation energies of C and O are illustrated in Fig. 4.4. C_B behaves as a DX center, but with a small magnitude of U. In the positive charge state, C_B exhibits only a small breathing relaxation, with the C–N bond lengths changing by 3.9%. In the negative charge state, a C–N bond is broken [Fig. 4.2(b)], and C_B is displaced by 0.64 Å from its substitutional site. Three C-N bonds with a bond length of 1.46 Å are formed with nearest-neighbor N atoms, and the fourth N neighbor is displaced outwards by 0.17 Å. This configuration is analogous to Si and O DX centers reported previously for AlN [133, 134], and similar to the so-called "trigonal broken-bond" DX center configuration previously described in GaAs [135]. We also find a localized state

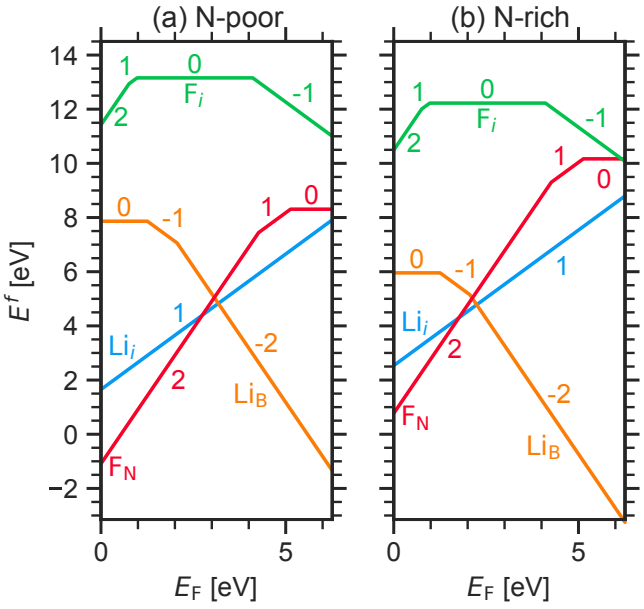

Figure 4.3: Formation energies for Li and F species under (a) N-poor and (b) N-rich conditions.

for the neutral charge state, with C_B again forming three C–N bonds with a bond length of 1.45 Å and the fourth N atom displaced outward by 0.18 Å. The neutral charge state is always higher in energy than either the positive or negative charge state, and hence C_B is a DX center with $U = -73$ meV and a (+/-) level at 0.64 eV below the CBM. This level is probably too deep to lead to any appreciable ionization at room temperature. An equally severe problem is that C_B is strongly self-compensated by C_N.

Oxygen is very close to being a DX center, but the neutral charge state of O_N is actually stable over a very narrow range of Fermi levels: we find the $(+/0)$ level at 0.43 eV and the $(0/-)$ level at 0.42 eV below the CBM. In the positive charge state, a breathing relaxation occurs where the bonds expand by 5.2%. In the neutral charge state, an O–B bond is effectively broken: one of the nearest-neighbor B atoms is moved

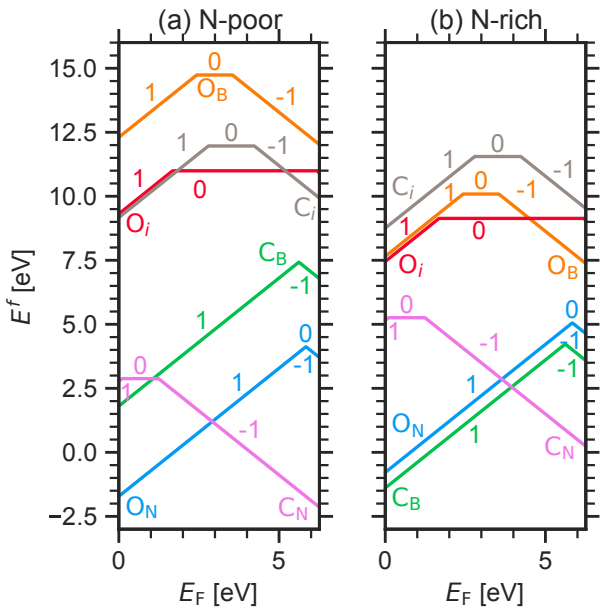

Figure 4.4: Formation energies for O and C impurities under (a) N-poor and (b) N-rich conditions.

outwards by 0.41 Å, while O forms B–O bonds with a bond length of 1.54 Å with the three remaining nearest-neighbor B atoms. In the negative charge state one of the B-O bonds is 40% longer than the equilibrium B-N bond length. In addition, two second-nearest neighbor B atoms move off site to form a dimer with a 1.63 Å bond, as illustrated in Fig. 4.2(c).

A striking difference between the acceptor state associated with C_B^- versus O_N^- is that in the case of O_N^-, the charge density of the occupied gap state is not centered on the O impurity. Instead, for O_N^- charge is localized around nearest-neighbor B and third-nearest-neighbor N atoms with respect to the O impurity. It is also distinct from behavior reported previously for the O_N *DX* center in AlN [133], for which charge localization on O was observed. Instead, the configuration of O_N^- is more similar to Si_B^- or the "cation-cation bonded" *DX* state in GaAs [132]. However, for O_N in c-BN

the dimer occurs next to a bulk N atom that is a second-nearest neighbor to O_N. (A similar structure was reported for Te_{As} DX centers in $Al_xGa_{1-x}As$ [132].)

Since the (+/0) and (0/−) levels of O_N are "only" 0.42-0.43 eV below the CBM, there is some likelihood of ionization. Assuming that oxygen exclusively incorporates on the N site, and based on a model of carrier statistics [136] that uses the effective density of states of the conduction band N_c=2×10^{19} cm^{-3} from Ref. [137], an O concentration of 10^{16} cm^{-3} leads to a carrier concentration around 10^{14} cm^{-3} at room temperature. This carrier concentration is in line with experimental observations of n-type conductivity in S-doped and unintentionally doped c-BN [117]. The (+/0) level of 0.42 eV below the CBM is also in agreement with the extracted activation energies of 0.32 eV for S-doped and 0.47 eV for unintentionally doped c-BN.

Based on our calculations, we have thus identified Si_B and O_N to be candidate donors as they have relatively low ionization energies, have lower formation energies than other impurities, and are not impacted by self-compensation due to substitution on a competing site. We still have to determine whether native point defects can either contribute to n-type conductivity or counteract the intended n-type doping.

We focus on vacancy defects, since previous studies [138, 139] have determined that other types of point defects are significantly higher in energy under n-type conditions. In Fig. 4.5 we show the formation energies of boron vacancies (V_B) and nitrogen vacancies (V_N) and compare them with the formation energies of the candidate donors, O_N and Si_B. We find that V_N is a deep donor that cannot contribute to n-type conductivity. V_B, on the other hand, acts as a deep acceptor and has a low formation energy under n-type conditions, even in a N-poor environment.

Therefore, in equilibrium conditions V_B will strongly compensate Si_B or O_N, pinning the Fermi level far below the CBM. Additionally, complex formation can occur

(see Fig. 4.5). The $(V_B–O_N)^{-2}$ complex has a binding energy of 4.38 eV (referenced to V_B^{-3} and O_N^+) and also acts as a deep acceptor. The $(V_B–Si_B)^{-2}$ complex behaves similarly with a binding energy of 2.89 eV.

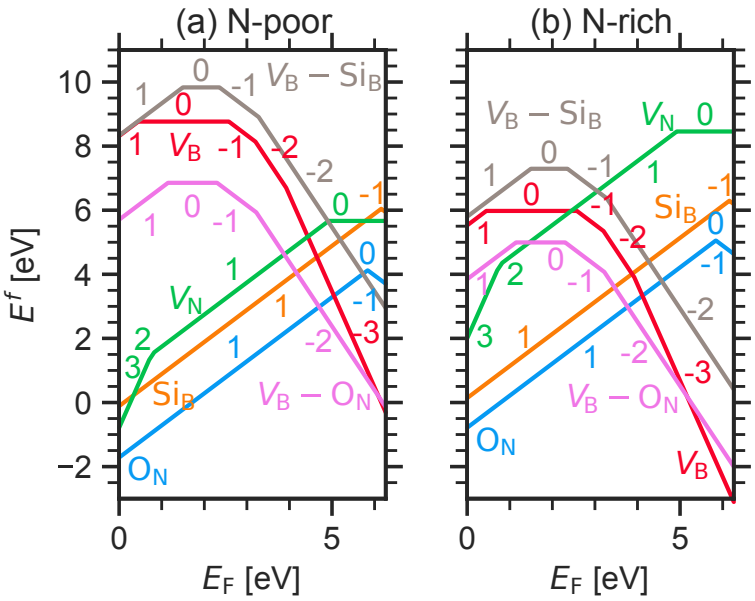

Figure 4.5: Formation energies for native vacancies, oxygen and silicon donors, and their complexes under (a) N-poor and (b) N-rich conditions.

Given that the boron vacancy is such a strong compensating center, the question remains as to how the experimentally observed [117, 118] n-type conductivity can be attained. We attribute this to dopant and defect incorporation being governed by non-equilibrium conditions during growth. Two key effects are of importance here: band bending and kinetics. It is likely that at the surface the Fermi level is pinned well below the CBM; this drastically raises the formation energy (and hence reduce the concentration) of compensating V_B, while increasing the incorporation of donors. Whether these non-equilibrium concentrations can be maintained as the material keeps growing (and the surface region becomes bulk) depends on the second

key effect, which is kinetics: a non-equilibrium concentration of dopants or defects may be "frozen in" if at the temperature of interest migration is suppressed.

To investigate this effect, we compute the migration barrier of V_B using NEB [131]. We obtain barriers of 3.68 eV for the -2 charge state and 3.61 eV for -3. The temperature where V_B becomes mobile is estimated using transition-state theory [140]:

$$\Gamma = \Gamma_0 e^{-E_b/k_B T} , \tag{4.1}$$

where Γ is the hopping rate, Γ_0 is a prefactor that is approximated as 10^{14} s^{-1} (on the order of phonon frequencies in c-BN), E_b is the migration barrier energy, and k_B is Boltzmann's constant. We then solve Eq. 4.1 for the temperature T where we would expect a given defect to become mobile (assuming $\Gamma = 1$ s^{-1}). The chosen parameters for our estimate are consistent with previous studies of boron nitride [138]. We find that the V_B becomes mobile above 1300 K.

In the high-pressure, high-temperature growth of c-BN, much higher temperatures are used, ranging from 1473 to 2273 K [121]; therefore, the concentration of V_B can be assumed to be in thermodynamic equilibrium. Thin-film growth, on the other hand, tends to use temperatures from room temperature up to 1200 K [118, 141]. For these temperatures, V_B is not mobile and would be "frozen-in" at lower concentrations than those corresponding to equilibrium in bulk n-type material. Band bending would then favor incorporation of the n-type dopants, and suppress formation of the compensating V_B.

Lastly, it is useful to point out that the vacancy complexes, V_B-O_N and V_B-Si_B, are potentially interesting quantum defects. Both complexes possess Kohn-Sham states within the band gap, which may allow for radiative internal transitions. Such transitions could be used for single-photon emission or to manipulate the spin state of

the complex. Indeed V_B-O_N and V_B-Si_B have a non-zero ground-state spin in the -1 charge state. The ground-state spin enables applications as a spin qubit. V_B-O_N has been previously proposed as an analogue to the diamond NV center [142].

4.4 Conclusions

In summary, our work provides a consistent understanding of n-type dopants in c-BN. Our survey of Si, Ge, S, Se, C, O, F, and Li highlighted the potential of Si_B and O_N as candidate donors as they have the lowest formation energies and are not impacted by self-compensation. Compensation by V_B, which acts as a deep acceptor, poses a challenge; however, we showed that since V_B has a large migration barrier, it may effectively be suppressed due to non-equilibrium conditions near the surface. Our work demonstrates that preparation of n-type c-BN will benefit from control of growth kinetics to enhance the incorporation of n-type dopants and limit the detrimental effect of V_B.

Permissions and Attributions

The content of Chapter 4 follows from work that has previously appeared in Applied Physics Letters (Ref. [30]). This work was performed in collaboration with Dr. Darshana Wickramaratne and Dr. John L. Lyons. Dr. Darshana Wickramaratne and Dr. John L. Lyons performed calculations of Ge and Se impurities.

Chapter 5

Dangling Bonds in Hexagonal Boron Nitride as Single-Photon Emitters

5.1 Introduction

Hexagonal boron nitride (h-BN) displays numerous desirable properties, such as a wide band gap [143] and excellent stability [144]; thanks to advances in growth techniques [145], h-BN has been incorporated into electronic and optoelectronic devices [146]. Several distinct single-photon emitters have been observed in h-BN; carbon dimers are the suspected origin of the emission near 4 eV [147]. Ultra-bright single-photon emission in the visible spectrum has also been reported [148]. The emission features strong zero-phonon lines (ZPLs) near 2 eV with modest coupling to phonon modes [149], rendering these sources extremely attractive for applications in quantum information science. However, in spite of extensive experimental efforts, the microscopic origin of these single-photon emitters (SPEs) has not been identified.

It has been found that the SPEs with ZPLs ranging from 1.6 to 2.2 eV can be created

with electron irradiation or with a high-temperature anneal [148], and ion implantation can be used to increase the formation probability of emitters [150]. Interestingly, h-BN samples grown with low pressure chemical vapor deposition (CVD) already have the emitters present, with ZPLs ranging from 2.10 to 2.18 eV [151]. Weak coupling to phonons is desirable for SPEs, since it concentrates intensity into a sharp zero-phonon line. The experimentally observed Huang-Rhys factor, a dimensionless parameter that characterizes the strength of electron-phonon coupling, is low for the SPEs in h-BN [149]. Furthermore, the emitters are linearly polarized [149, 150]. Some information about the spin state is also available: Exarhos *et al.* found that some emitters exhibit magnetic field dependence and suggested a singlet-to-triplet intersystem crossing model [88]. Coupling to magnetic fields is an important attribute since it enables spin qubits and spin-based sensing [8].

Theoretical studies have proposed a variety of different centers as potential candidates for the SPEs. A negatively charged boron vacancy (V_B) has been suggested to explain the emission [152]. However, this defect has recently been shown to have very broad luminescence with peak emission at 1.46 eV [153]; it is more consistent with the spin qubits observed in Ref. [154] rather than with the 2-eV emitters. Another proposal was for a complex between a nitrogen vacancy and a nitrogen antisite (V_N-N_B) [152, 155]; recent calculations demonstrate a large strain dependence that was suggested to explain the range of emission energies observed experimentally [156]. However, this center suffers from a lack of stability: for Fermi-level positions where the neutral V_N-N_B is stable, the V_B defect is lower in energy [152]. The V_N-N_B defect is therefore unlikely to be seen in experiment. A complex with carbon impurities, V_N-C_B, has also been proposed to explain the 2-eV emission [157]. Similar to other vacancy complexes, this defect has a high formation energy, and the neutral charge state (cor-

responding to the $S = 0$ spin state) is stable over only a narrow range of Fermi-level energies [158, 159], making it unlikely to be seen in experiment.

Here we propose that dangling bonds (DBs) are the source of the observed single-photon emission in h-BN. DBs are different and distinct from the many other sources proposed to date, and exhibit properties in excellent agreement with experimental observations. DBs are formed when the regular bonding arrangement in a crystalline material is disrupted; they can be found at surfaces, interfaces, grain boundaries, and in voids. Experimental support for the attribution of SPEs to dangling-bond-like defects comes from the observation that emitters are typically localized near crystal edges or grain boundaries [150, 160, 161]. While DBs may be sensitive to their local environment, they can be extremely stable and plentiful, e.g., they are the primary defect in Si/SiO_2 interfaces [162].

To our knowledge, our present study is the first to examine DBs in h-BN. We will demonstrate that DBs act as single-photon emitters with characteristics that are consistent with experimental observations. This new view of DBs, as quantum defects with controllable properties, may be extended to other systems for which single-photon emission has been observed without attribution. In addition, the information generated here is also valuable in the context of using h-BN in electronic devices, since the presence of DBs can seriously impact device performance [163, 164].

In this dissertation, we uncover the physics of DBs in h-BN through first-principles calculations. We focus on B DBs; we will show that N DBs do not possess the necessary level structure to give rise to 2-eV emission. It has been shown that h-BN flakes are predominantly N terminated [165–167]. Boron DBs will therefore be relatively rare (occurring, e.g., at corners or kinks [168]), in agreement with experimental observations. In the ground state, the B DB is doubly occupied. An internal transition can

occur where one of the electrons is excited into a localized p_z state on the B atom, as shown by the calculated configuration coordinate diagram in Fig. 5.1, which will be explained later. The properties of these transitions are in excellent agreement with the observed characteristics of the SPEs: luminescence occurs with a ZPL of 2.06 eV and a Huang-Rhys factor of 2.3. With regard to polarization, direct excitation into the p_z state leads to emissive dipoles aligned with absorption, but modest increases in the excitation energy lead to excitation into extended states and a consequent lack of dipole alignment, in good agreement with experimental observations of polarization [169]. The ground state of the doubly occupied B DB is a singlet, and the optical transitions described above are spin-conserving; however, we find that an intersystem crossing to a metastable triplet state exists [88]. All of these calculated properties indicate that doubly-occupied B DBs are the likely microscopic origin of the observed 2-eV SPEs.

5.2 Methodology

We utilize the point-defect formalism, described in Sec. 2.6, to study dangling bonds. For the present study, the energy cutoff for the plane-wave basis set is 520 eV. We use the hybrid functional of Heyd, Scuseria, and Ernzerhof [63, 64] with the Grimme-D3 scheme to correct for the van der Waals interactions [170]. This approach has been extensively tested, both in the context of the present study and as part of previous work on h-BN [138, 171]. The fraction of non-local Hartree-Fock exchange α is set to 0.40; this results in a band gap of 6.41 eV which is consistent with the experimentally observed gap [143] when zero-point renormalization due to electron-phonon interactions [172, 173] is taken into account. This value of the mixing parameter is also close to satisfying Koopmans' condition [61]. The resulting lattice parameters are

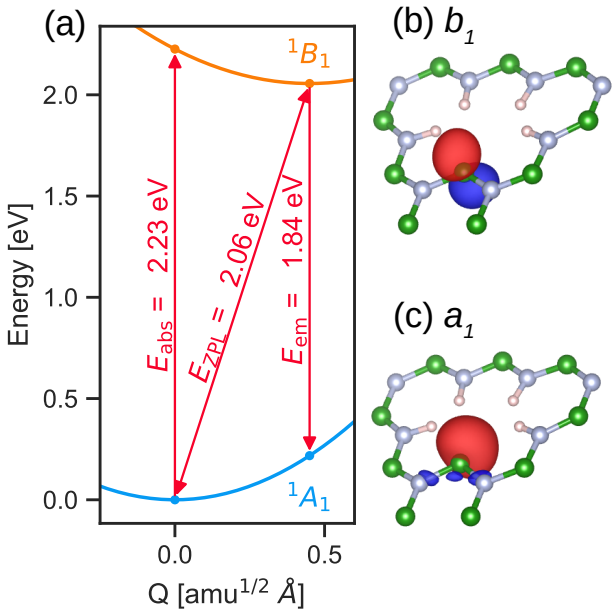

Figure 5.1: (a) Calculated configuration coordinate diagram for the ${}^1A_1 \rightarrow {}^1B_1$ internal transition of the doubly occupied B DB. (b) Charge density isosurface of the B p_z state that becomes localized upon excitation. (c) Charge density isosurface of the B DB state that the electron occupies in the ground state. The isosurfaces correspond to 10% of the maximal charge density and are colored by the sign of the wavefunction, with red and blue indicating opposite signs.

$a = 2.48$ Å and $c = 6.57$ Å, within 1.2% of the experimental values ($a = 2.50$ Å and $c = 6.65$ Å [174]). Defects are investigated in a 240-atom supercell, constructed by first building an orthorhombic cell ($a \times a\sqrt{3} \times c$) from two h-BN primitive cells and then scaling by $5 \times 3 \times 2$. The lattice vectors are held fixed, and atomic coordinates are relaxed until forces are below 0.01 eV/Å. Brillouin-zone sampling is performed using a single special $\mathbf{k}$ point $(1/4, 1/4, 1/4)$. Spin polarization is explicitly taken into account.

Removing a single host atom, i.e., forming a vacancy, creates three DBs; however, the close spacing of atoms surrounding the vacancy leads to strong interactions that significantly modify the electronic structure. As we will see, the properties of isolated

DBs are very different from those of vacancy centers. To simulate the properties of an isolated DB, we employ the geometry of Ref. [175]. For instance, to construct a B DB we remove a neighboring N atom, as well as two additional B atoms [see Fig. 5.2(a)]. This process creates a small void, containing the primary B DB that we wish to study, plus four secondary N DBs. In order to create a reference structure, all five DBs are passivated with hydrogen, and the atomic coordinates are relaxed allowing only in-plane degrees of freedom. In subsequent calculations, the B DB is studied by removing the hydrogen from the B-H bond, and relaxing atoms up to second-nearest neighbors, keeping all other atoms in the reference structure fixed. All relevant parameters are obtained as energy differences, in which the contributions from the fixed atoms in the reference structure cancel.

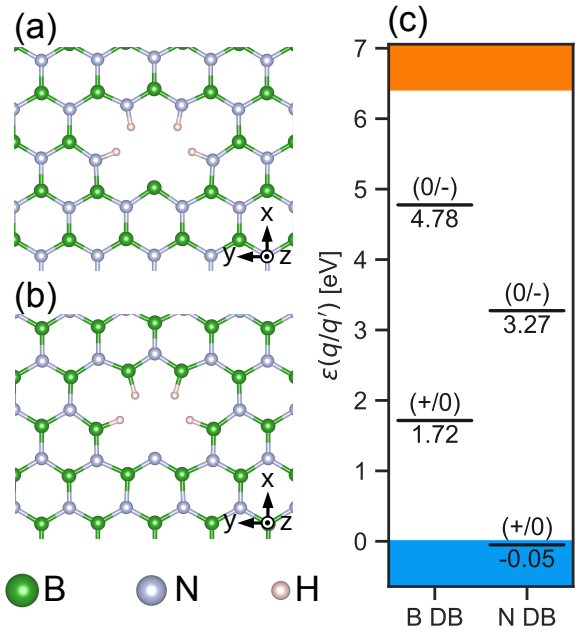

Figure 5.2: Equilibrium structures for the (a) boron and (b) nitrogen DBs. Boron atoms are shown in green, nitrogen in gray, and hydrogen in white. (c) Calculated thermodynamic transition levels for both DBs. The valence and conduction band are highlighted in blue and orange.

5.3 Results

Equilibrium structures for the B and N DBs are shown in Fig. 5.2(a) and (b). Our calculations indicate that in this idealized geometry the DBs have C_{2v} symmetry with the two-fold rotation axis pointing in-plane, along the DB. We choose a coordinate system with **x** pointing along the C_{2v} symmetry axis and adopt a convention where the B_1 irreducible representation transforms like the vector **z** (out of plane), and B_2 transforms like **y** (in plane). DBs may be occupied with zero, one, or two electrons, which in our calculations correspond to a positive, neutral, and negative charge state. The relative energies of these charge states depend on the Fermi level, and the Fermi-level positions where the transitions between different charge states occur are the thermodynamic transition levels, given in Eq. 2.33.

The computed thermodynamic levels for both the B and the N DBs are shown in Fig. 5.2(c). For the B DB, both the $(+/0)$ and $(0/-)$ thermodynamic levels are found within the band gap; therefore, the B DB may be unoccupied, singly occupied, or doubly occupied, depending on the Fermi-level position in the material. For the N DB, on the other hand, the $(+/0)$ level is slightly below the VBM, indicating that the N DB will never be completely unoccupied in equilibrium. Kohn-Sham (KS) states for the two types of DBs are shown in Fig. 5.3. In the neutral charge state, the occupied KS state associated with the N DB is below the VBM. In the negative charge state, the N DB is fully occupied and has a_1 symmetry [Fig. 5.3(a)]; interestingly, a KS state with b_1 symmetry associated with the p_z state on the N atom has become localized and has moved into the band gap. No spin-conserving excitations to localized defect states can occur for either the singly or doubly-occupied N DB, and hence this DB cannot give rise to strong optical emission.

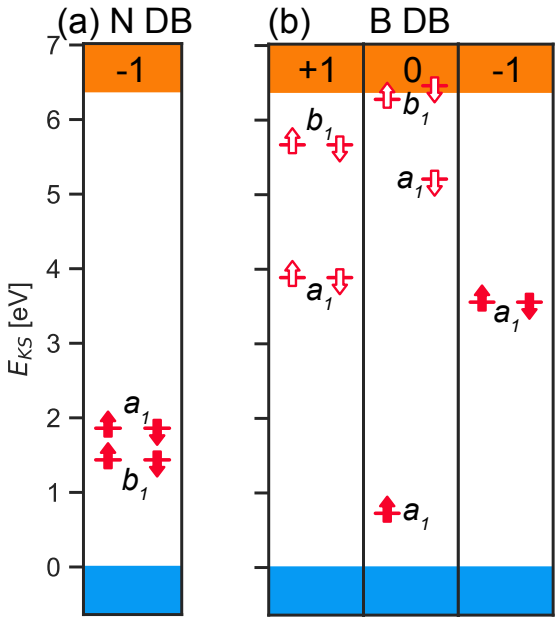

Figure 5.3: Schematic depiction of the KS states for (a) the N DB in the negative charge state, and (b) the B DB in the positive, neutral, and negative charge states. The valence and conduction band are highlighted in blue and orange. Solid arrows depict occupied states, and open arrows depict unoccupied states.

The KS states for the B DB in all three charge states are shown in Fig. 5.3(b). In the positive charge state, the B DB is unoccupied, and KS states associated with the B p_z state (with b_1 symmetry) are also in the gap. Upon addition of one electron to the DB, the B p_z KS state shifts higher in energy and occupies a position just below the conduction-band minimum (CBM). Therefore, the neutral charge state of the B DB has the possibility of an internal transition, where the electron in the B DB can be excited into the B p_z state. In the negative charge state, two electrons occupy the DB; the B p_z state moves above the CBM and becomes delocalized. While this may seem to rule out the possibility of an internal transition, we will see that upon excitation (which leaves the a_1 state half occupied) the B p_z state becomes localized.

To study internal transitions we employ the ΔSCF methodology [72] in which exci-

tation energies are computed as a total-energy difference between two calculations in which the occupations are constrained, each including full atomic relaxation. We employ configuration coordinate diagrams to schematically depict the coupling of these electronic transitions to lattice vibrations [8] and to compute the Huang-Rhys factors within the one-dimensional approximation [83]. The computed ZPL for the internal transition in the neutral charge state is 3.27 eV, with a Huang-Rhys factor of 7.9; this ZPL does not correspond to any observed single-photon emission.

In the negatively charged ground state, two electrons occupy the B DB in a singlet state, transforming like the A_1 irreducible representation of C_{2v}. We label the state $^1A_1$, where the superscript refers to the multiplicity $2S+1$ for a system of total spin S. We first consider the spin-conserving excitation of an electron from the DB to a B p_z state. The computed configuration coordinate diagram for this transition is shown in Fig. 5.1(a). Upon excitation the B p_z state becomes localized, transforming like the B_1 irreducible representation [shown in Fig. 5.1(b)]; we therefore label the excited state $^1B_1$. In the excited-state calculation, the KS state of the B p_z occurs just below the CBM, similar to the b_1 state in the neutral charge state. The ZPL for the $^1A_1 \rightarrow {}^1B_1$ transition is calculated to be 2.06 eV, in excellent agreement with the experimental reports [148, 151]. The Huang-Rhys factor for this transition is 2.3, on par with the range of experimental values reported in Ref. [149]. The B DB is therefore a good candidate for the SPE, provided it occurs in a negative charge state, requiring the Fermi level to be sufficiently high in the band gap. Such a position is plausible, given the likelihood of oxygen contamination of the samples [176]. Oxygen impurities act as donors and drive the Fermi level towards the CBM [138].

One might expect that the emissive and absorptive dipoles would be aligned, but it has been reported that this is not necessarily the case [149]. Jungwirth and Fuchs [169]

demonstrated that for resonant excitation the dipoles are aligned, but that misalignment occurs for higher excitation energies. The characteristics of B DBs nicely explain these observations. For excitations at or slightly above the resonant absorption energy [Fig. 5.1(a)], the alignment of the dipole is maintained. But because of the proximity of the b_1 state to the CBM, absorption at higher energy will place the electron in the conduction band, leading to a loss of polarization. The subsequent emission process, after the electron is captured into the excited state, then occurs with a polarization that is unrelated to the absorption dipole.

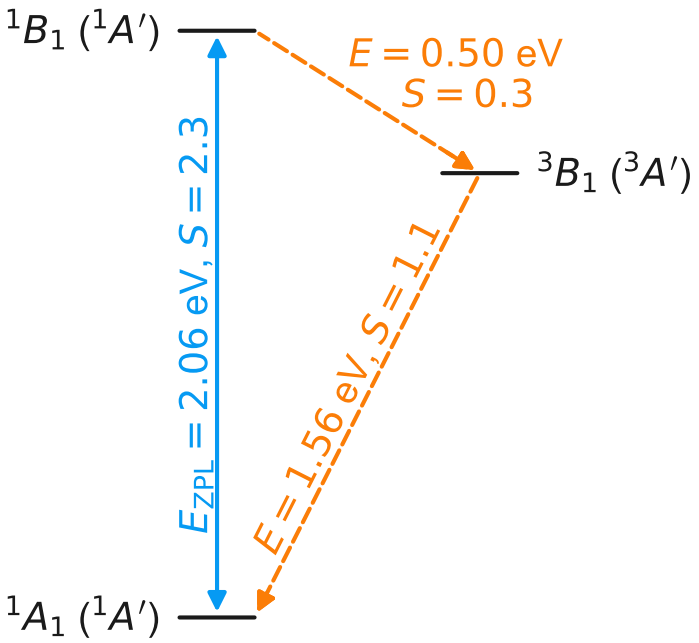

Figure 5.4: Intersystem crossing of the doubly-occupied B DB. The solid blue line indicates an optical transition, and dashed orange lines indicate nonradiative crossings between spin channels. Alternative labels under C_s symmetry are given in parenthesis. Each transition is labeled with the transition energy and the Huang-Rhys factor S.

Our model of the negatively-charged B DB also predicts the presence of a metastable shelving state. The intersystem crossing to the shelving state is shown in Fig. 5.4. In addition to the $^1B_1$ excited state that occurs within the spin-singlet manifold, we can

consider a $^3B_1$ triplet state where one electron occupies the DB and one occupies the B p_z state in a high-spin configuration. Our calculated level structure in Fig. 5.4 is similar to the singlet-to-triplet intersystem crossing proposed by Exarhos *et al.* [88] based on their study of the magnetic-field dependence of the SPEs, differing in the definition of B_1 and B_2 and the fact that they only considered diagrams with in-plane polarization.

Intersystem crossings depend on spin-orbit coupling to induce transitions. The spin-orbit coupling operator is given by $H_{SO} = \sum_i \boldsymbol{l}_i \cdot \boldsymbol{s}_i$, where i labels the electrons, $\boldsymbol{s}_i$ is the spin angular momentum operator, and the orbital angular momentum operator $\boldsymbol{l}_i$ is $(1/2m^2c^2)\boldsymbol{\nabla} V(\boldsymbol{r}_i) \times \boldsymbol{p}_j$, where V is the nuclear Coulomb potential [152]. Within C_{2v} symmetry, orbital angular momentum transforms like an axial vector with no A_1 component, and $B_1 \otimes B_1 = A_1$. Therefore, spin-orbit matrix elements between the $^1B_1$ and $^3B_1$ states are zero. In a lower symmetry, such as C_s, spin-orbit matrix elements between these states are non-zero and the intersystem crossing becomes allowed.

Indeed, such symmetry lowering should be expected for the dangling-bond defects proposed here. Given that these defects occur at the edge of flakes or near grain boundaries [150, 160, 161], the perfect C_{2v} symmetry as assumed in our idealized geometry will be broken. Local distortions and interactions will distort the DB out of plane and into a lower symmetry, such as C_s. This is in agreement with recent experiments that demonstrated Stark tuning of the SPEs in h-BN and suggested that an out-of-plane, permanent dipole is necessary to couple to the electric field [177]. The sensitivity of the properties of these DBs to the local environment explains why experimentally a range of SPEs with slightly different emission wavelengths are observed [148, 160, 161]. The identification of SPEs as DB defects actually allows us to propose an explanation for the mechanism by which nanopillars activate emitters in h-BN [178]: the induced curvature acts to bend the DBs out of plane.

Deviations from C_{2v} symmetry also account for the polarization of the optical transition. Selection rules for electric dipole transitions would indicate that the ${}^1A_1 \rightarrow {}^1B_1$ transition is allowed only for out-of-plane polarization, while experiments report in-plane polarization [149, 150]. With C_s symmetry, both the ground and excited state orbitals will transform like A', and in-plane polarized transitions are allowed.

5.4 Conclusions

In summary, our calculations provide valuable information about the physics of DBs in h-BN. Doubly-occupied B DBs exhibit many of the experimentally reported features of single-photon emission. With a singlet ground state, an electron can be excited from the DB to a B p_z state; this internal transition has a ZPL at 2.06 eV. The calculated electronic structure of the DB explains why alignment of the absorptive and emissive dipoles depends on the excitation energy [169]. The dangling-bond system exhibits an intersystem crossing to a metastable triplet state, in agreement with experiment [88]. The sensitivity of DBs to the local environment explains why SPEs with a range of wavelengths have been observed [148, 160, 161], but offers exciting prospects for controlling and manipulating SPEs now that the microscopic origin has been identified.

Permissions and Attributions

The content of Chapter 5 follows from work that has previously appeared in Physical Review Letters (Ref. [31]). This work was performed in collaboration with Prof. Audrius Alkauskas and Prof. Lee C. Bassett.

Chapter 6

Boron Dangling Bonds in a Monolayer of Hexagonal Boron Nitride

6.1 Introduction

In Chapter 5, we proposed boron dangling bonds (DBs) as the likely microscopic origin of the 2-eV single-photon emission in h-BN. Those calculations addressed the DB in a bulk crystal of h-BN, consistent with the thick flakes that are typically used in experiment. For applications, monolayers are being envisioned, and it is therefore important to examine the optical properties of the boron DB in a single monolayer. Indeed, a main drawback of the prototype nitrogen-vacancy center in diamond is the decoherence from defects on the diamond surface [20]. Quantum defects in two-dimensional (2D) materials may avoid these problems and enable extreme sensing, where the defect is brought atomically close to the sample.

Here we report first-principles calculations based on density functional theory (DFT) with a hybrid functional for boron DBs in a monolayer of h-BN. We find that

the optical transition has the same character as in bulk, and occurs at roughly the same energy (2.02 eV). The coupling to phonons is characterized by a Huang-Rhys factor of 2.4, again close to the value for the bulk defect. We also find that a metastable triplet state and thus an intersystem crossing (ISC) exists. While the properties of the B DB in a monolayer are quite similar to those for the DB in bulk h-BN, we provide details about both the singlet and triplet states that can affect the ISC rates.

6.2 Methodology

The computational methodology employed in the present study follows the details of Sec. 5.2. For consistency, the fraction of non-local Hartree-Fock exchange α is again set to 0.40. However as noted in Sec. 2.4.1, the value of α is related to the dielectric constant of the system [55], and the reduced dielectric environment of a monolayer might require a higher value of α. We have checked that our results are not sensitive to the value of α and all our qualitative conclusions are robust. α=0.40 results in an indirect (K $\rightarrow$ Γ) fundamental band gap of 6.31 eV. The direct optical gap is at K with a value of 7.06 eV. The supercell construction also follows Sec. 5.2, but only a single 60-atom layer is retained. A vacuum region of 20 Å is used to separate periodic images along the $\hat{z}$ direction.

Our boron DB is negatively charged; the treatment of charged defects in reduced dimensions requires special care in the handling of the compensating background charge. In plane-wave DFT, the divergent $\mathbf{G} = 0$ Fourier component of the electrostatic potential is set to zero. For a charged system, this corresponds to adding a homogeneous background charge, sometimes referred to as the jellium background. This procedure works very well in three-dimensional solids, as long as appropriate

correction terms are included to compensate for the interaction of the defect with the background in a finite cell [70]. Problems arise, however, in simulations of 2D materials that require a large vacuum region: the jellium background is present in the vacuum, which is unphysical. We contrast this with the actual physical situation, in which a charged defect in a monolayer would be compensated by oppositely charged dopants or defects associated with the same monolayer, rendering the system net neutral.

The unphysical nature of the standard treatment, in which a jellium background is present in the vacuum, is illustrated in Fig. 6.1. The conduction-band minimum of monolayer h-BN is a nearly-free electron (NFE) state at Γ. The NFE state has a large spatial extent above and below the h-BN plane. When a negatively charged defect is introduced into the system, the NFE state is attracted to the positively charged jellium background through the Coulomb interaction. The NFE state spreads out over the entire vacuum region and lowers in energy; as a result, a spurious reduction of the band gap by 1.0 eV is observed.

One method to correct for this effect would be to only apply a homogeneous background in the plane of the material, which requires modifying the underlying DFT implementation [179]. Here, we use a different approach, in the spirit of the virtual-crystal approximation [180]. The compensating background is applied by modifying the valence charge Z of the B and N atoms in the cell by an amount $\Delta Z = -q/N_{at}$, where q is the charge of the defect and N_{at} is the number of atoms that the compensating charge is spread over. The result of this procedure is shown in Fig. 6.1, where the charge distribution of the NFE state more closely resembles that of the pristine supercell, with only minor perturbations due to the presence of the defect. Furthermore, the band gap in the defect supercell now agrees with the primitive-cell value.

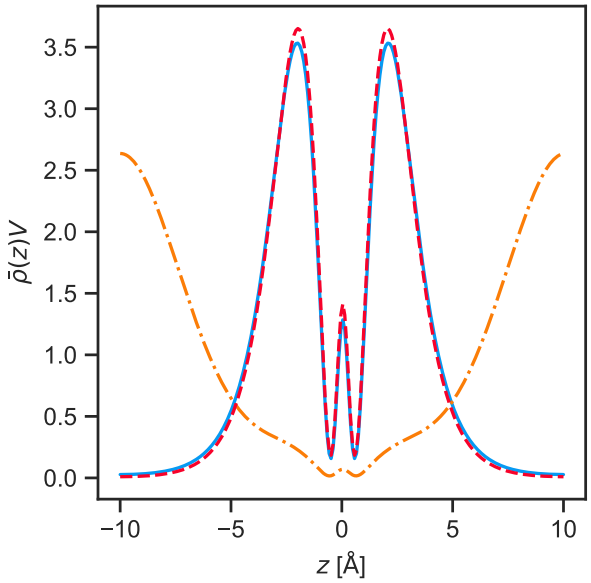

Figure 6.1: The planar-averaged charge density $\bar{\rho}(z)$ of the conduction-band minimum along the direction perpendicular to the h-BN monolayer. The h-BN plane is at $z = 0$, and V is the supercell volume. Results are shown for the pristine supercell (blue, solid), negatively charged dangling bond with a jellium background (orange, dashed-dotted), and negatively charged dangling bond with the compensating charge confined to the plane (red, dashed). The correct charge density of the conduction-band minimum is well reproduced when the compensating charge is confined to the h-BN plane. The minor difference between the blue and red curves arises from the perturbation imposed by the defect.

6.3 Results

The relaxed structure of the B DB is shown in Fig. 6.2(a) and Fig. 6.2(b). For our model, the B DB assumes C_{2v} symmetry in the monolayer; we emphasize that based on experimental conditions, it is likely that the B DB will attain a lower symmetry, like C_{1h}, due to out-of-plane distortions. This argument is motivated by the fact that the emitters tend to be found near flake edges or extended defects [150, 161]. Indeed, the sensitivity of the DB to its local environment explains why a wide range of emission energies have been observed in experiments [148].

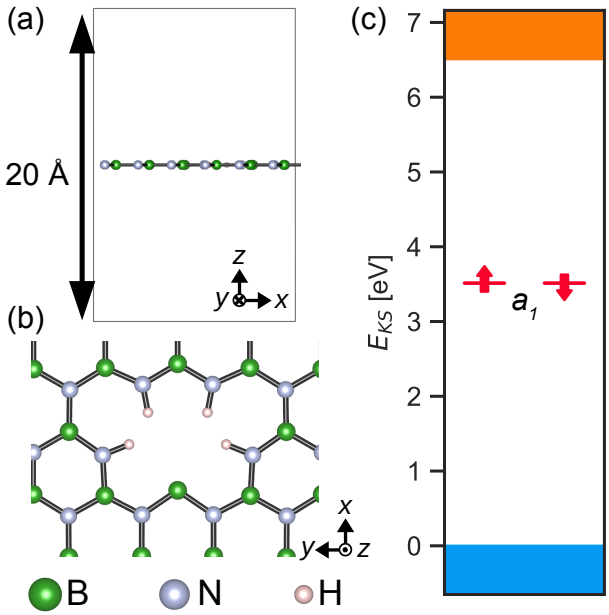

Figure 6.2: (a) Side and (b) top view of the relaxed structure for the boron DB. Boron atoms are shown in green, nitrogen in grey, and hydrogen in white. (c) The spin-degenerate Kohn-Sham state for the negatively charged B DB. The valence band is colored blue and the conduction band orange. Arrows depict occupied states.

We assume a coordinate system where the x axis is along the high-symmetry axis of the defect and the z axis is orthogonal to the h-BN plane. The coordinate axes are shown in Fig. 6.2. With these definitions, the irreducible representation A_1 of C_{2v} transforms like the vector **x**, B_1 like **z**, and B_2 like **y**.

We focus on the negative charge state of the defect, as this was found to host an internal transition corresponding to the 2-eV emission in bulk h-BN (see Sec. 5.3). A spin-degenerate Kohn-Sham state associated with the negatively charged B DB is located in the gap, as shown in Fig. 6.2(c). The charge-density isosurface for this state is shown in Fig. 6.3(a). This state transforms like the A_1 irreducible representation and is labeled as a_1.

We now explore, using the constrained DFT approach, whether an internal transi-

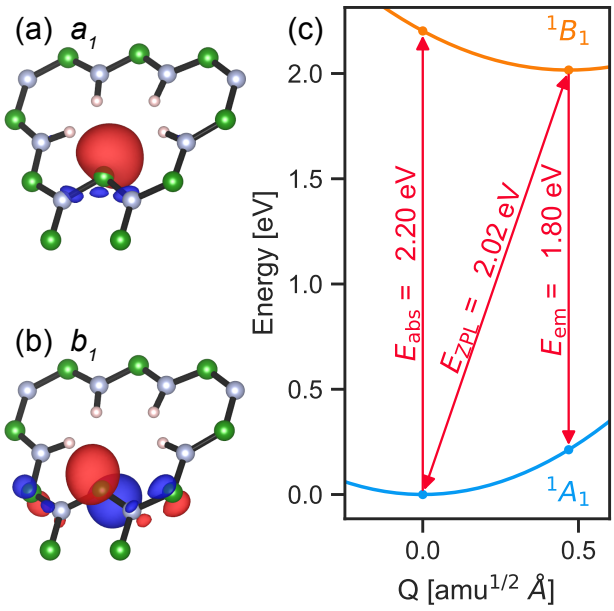

Figure 6.3: Charge-density isosurface for (a) the B DB and (b) the localized B p_z state. The isosurface corresponds to 10% of the maximal charge density. Boron atoms are shown in green, nitrogen in grey, and hydrogen in white. The isosurface is colored by the sign of the wavefunction, with red and blue indicating opposite signs. (c) The calculated configuration coordinate diagram for the $^1A_1 \rightarrow {}^1B_1$ transition.

tion can take place in the negatively charged B DB. We find that, upon excitation, an electron becomes localized in a p_z orbital, as shown in Fig. 6.3(b). This state transforms like the B_1 irreducible representation and is labeled as b_1.

In the ground state, two electrons occupy the B DB in a singlet state; this many-body state is labeled as $^1A_1$ where the superscript is the spin multiplicity $2S + 1$ for total spin S. The excited state has one electron in the B DB and one in the B p_z state, giving a many-body state of $^1B_1$. From our calculations, we find that the transition $^1A_1 \rightarrow {}^1B_1$ has an energy of 2.02 eV, which corresponds to the zero-phonon line. The relevant energetics after considering coupling to phonons are displayed as a configuration coordinate diagram in Fig. 6.3(c). We extract a Huang-Rhys parameter of 2.4.

These values for the transition energy and for the Huang-Rhys factor differ only

slightly from the case of a B DB in bulk h-BN (a zero-phonon line of 2.06 eV and Huang-Rhys factor of 2.3), and are actually within the computational error bar. The value of the Huang-Rhys parameter is related to the fraction of light going into the zero-phonon line compared to the phonon side band. Our extracted Huang-Rhys parameter compares favorably with experiment, albeit slightly larger than the reported values of 1-2 [149]; however, it has been suggested that experiments may underestimate the value due to the difficulty in distinguishing between photons from the zero-phonon line and those coupled to low-energy acoustic phonons [181]. Experimentally, it has been observed that the linewidth of the zero-phonon line broadens significantly in a monolayer compared to bulk flakes [155], but we do not attempt to capture this effect in our calculations.

The transition examined in Fig. 6.3 is spin-conserving. We can also examine the high-spin configuration of the excited state, where the electrons in the DB and in the p_z state have parallel spins, i.e., $S = 1$. We label this state $^3B_1$ and show its energetic position with respect to $^1A_1$ and $^1B_1$ in Fig. 6.4. The state $^3B_1$ is a metastable triplet state that is accessible through an ISC from the singlet states. The energies are again close to those calculated for the defect in bulk h-BN, but the Huang-Rhys factors are slightly different: for the monolayer, we have 0.2 and 1.5 for the upper and lower ISC, while for the bulk the values are 0.3 and 1.1 (see Sec. 5.3). The difference arises from small differences in the geometry of the triplet state: the triplet state in the monolayer is closer in geometry to the excited singlet state, compared to the bulk case. Further investigations of how this impacts the ISC rates could be fruitful. The presence of the metastable triplet state would manifest experimentally through a magnetic-field dependence in the photoluminescence spectrum. When one considers a lower symmetry, such as C_{1h} (also shown in Fig. 6.4), the level structure is consistent with the

experimental observations of magnetic-field dependence in bulk samples [88]. Such symmetry lowering is quite plausible in realistic samples, in which the emitters tend to be found near flake edges or near extended defects [150, 161]. Based on our calculations, we expect a similar dependence will be observed for monolayer samples.

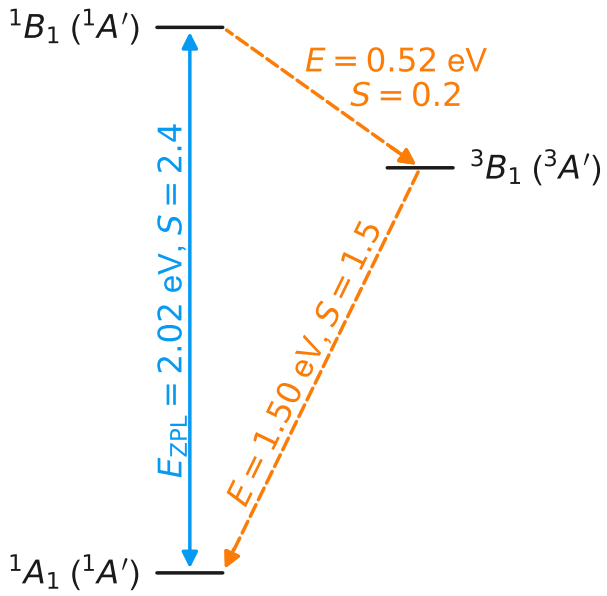

Figure 6.4: The many-body states of the negatively charged B DB. Each transition is labeled by an arrow with the energy and Huang-Rhys factor. The solid blue line corresponds to a spin-conserving optical transition. Orange dashed lines correspond to intersystem crossings between spin channels. The labels for our model when considering C_{1h} symmetry are given in parentheses.

6.4 Conclusions

In summary, we described comprehensive hybrid-functional calculations for the boron DB in monolayer h-BN. The handling of the compensating background charge was of key importance for correctly assessing the behaviour of defects in monolayer h-BN. An internal transition where an electron is excited from the doubly occupied

DB into a localized p_z state gives rise to optical emission at 2.02 eV. The coupling to phonon modes is characterized by a Huang-Rhys factor of 2.4. A metastable triplet state exists that enables an ISC and may give rise to a magnetic-field-dependent photoluminescence spectrum. While, overall, the properties of the B DB in the monolayer are similar to those in bulk h-BN, distinct differences exist that will impact the ISC rates. Our results provide essential information toward utilization of the B DB in monolayer h-BN for extreme sensing and quantum information applications.

Permissions and Attributions

The content of Chapter 6 follows from work that has previously appeared in the Journal of Applied Physics (Ref. [32]).

Chapter 7

Impact of Out-of-Plane Distortions on Dangling Bonds in Hexagonal Boron Nitride

7.1 Introduction

An important and commonly disregarded property of 2D materials is the fact that they exist in three dimensions: relevant physics from the bending and twisting of the 2D planes is often overlooked. In the boron DB model (developed in Chapter 5 and extended to a monolayer in Chapter 6), this is a key feature for interpreting the experimental results. Here we treat this effect with computational modeling and explicitly explore the effects of an out-of-plane displacement on the boron DB in h-BN with first-principles calculations. The deformation is modeled by bending a plane that neighbors the DB, inducing a displacement in the defect similar to what can happen experimentally. We describe the resulting structural changes and energetics of

the boron DB, as well as the impact on the radiative rate. We also discuss our results in the broader context of experimental observations on the 2-eV emitters. The present work strengthens the attribution of the 2-eV emitters to boron DBs, and more generally highlights the importance of considering out-of-plane displacements in 2D materials.

7.2 Methodology

We adopt the same approach as described in Sec. 5.2 for the present study. Changes in the electronic configuration of a system are usually accompanied by a change in the atomic coordinates: this is a manifestation of electron-phonon coupling. The Huang-Rhys parameter S quantifies the electron-phonon coupling for a given transition and allows for comparison with experiment. Within a single-mode approximation, the Huang-Rhys parameter can be defined as [23]

$$S = \frac{1}{2\hbar}(\Delta Q)^2 \Omega \,, \tag{7.1}$$

where Ω is the vibrational frequency of the ground state along the single mode. ΔQ is the mass-weighted difference in geometries, given by Eq. 3.1. (Here the initial state is the excited state, and the final state is the ground state.)

We will also study the radiative transition rate Γ_{Rad} or equivalently, the radiative lifetime $\tau_{\text{Rad}} = \Gamma_{\text{Rad}}^{-1}$. The equation for the radiative transition rate is given in Eq. 2.43. For the index of refraction n_r, we use the experimental value of 2.4 [182]. E_{ZPL} and μ are evaluated explicitly from first principles.

7.3 Results

7.3.1 Boron dangling bonds

An isolated DB is modeled using a small void, in which other DBs on the internal surface of the void are passivated by hydrogen, as detailed in Sec. 5.2. The in-plane structure of the boron DB has C_{2v} symmetry (see Sec. 5.3), as shown in Fig. 7.1(a). For our coordinate system, **x** points along the C_{2v} symmetry axis, and **z** is perpendicular to the h-BN plane. We adopt the convention where the B_1 irreducible representation of C_{2v} transforms like the vector **z**, and B_2 transforms like **y**.

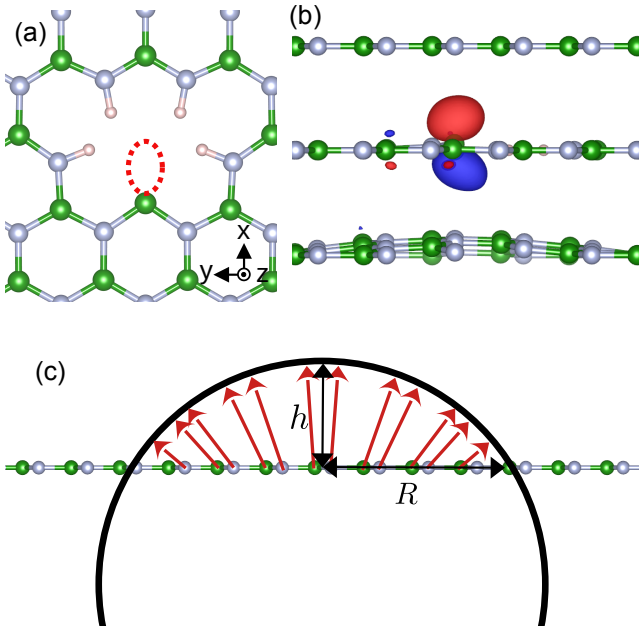

Figure 7.1: (a) The in-plane structure of the boron DB with the location of the DB shown as a dashed, red line. (b) Side view of the boron DB in the presence of the applied distortion, showing a 10% charge-density isosurface of the localized p_z state. The isosurfaces are colored by the sign of the wavefunction, with blue and red indicating opposite signs. (c) Mapping of the bubble geometry onto the h-BN plane (not to scale). Atoms are moved radially onto the surface of a sphere defined by the intersection radius R and height above the plane h. Boron atoms are shown in green, nitrogen in gray, and hydrogen in white.

Experimentally, the 2-eV emitters are usually found near flake edges, wrinkles, and extended defects [150, 160, 161]. All of these can be expected to induce out-of-plane displacements. Extended defects of this type are difficult to study from first principles because modeling them requires large supercells. Instead, we use an idealized distortion in which the h-BN plane adjacent to the DB is modified to mimic the presence of a "bubble" directly below the boron atom that hosts the DB [Fig. 7.1(b)]. Nanobubbles have actually been used experimentally to activate emitters in h-BN [183].

To construct the bubble, atoms from the neighboring h-BN plane are moved out of the plane to positions on the surface of a sphere [Fig. 7.1(c)]. This sphere is defined by a length R, which is the radius of the circle from the intersection of a sphere and the plane, and applied distortion h, which is the height above the h-BN plane that the bubble protrudes. For the purposes of our study, R is fixed to 5.5 Å, and h will take on values of 0.2, 0.5, and 1.0 Å.

7.3.2 Effect of distortions

We now examine how the applied distortion in the plane adjacent to the boron DB influences the properties of the DB. First, we confirm that the applied distortion indeed results in an out-of-plane displacement for the DB. In Fig. 7.2(a), we show the displacement of the B atom that hosts the DB, referenced to its nominal position in the plane. The displacement varies approximately linearly with the applied distortion, confirming that the model distortion results in an out-of-plane displacement of the DB. As a result of the displacement, the symmetry is lowered from C_{2v} to C_{1h}, where the vertical mirror plane is preserved. In the singlet excited state, the displacement is more significant than in the ground state, due to the occupation of a p_z state that is more extended in the **z** direction than the ground state of the DB. We also found

that the displacement in the triplet excited state is similar to that of the singlet excited state.

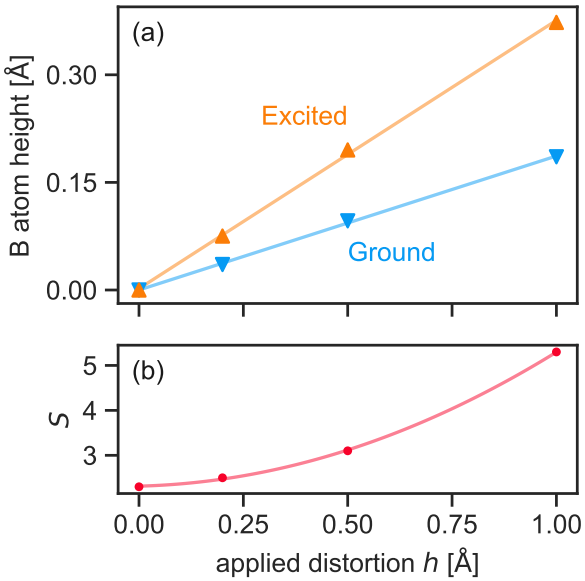

Figure 7.2: (a) Height above the plane of the B atom that hosts the DB as a function of applied distortion h. Results for the ground state are in blue (down triangles), and for the singlet excited state in orange (up triangles). (b) Huang-Rhys factor S that quantifies the electron-phonon coupling for the singlet-singlet optical transition, as a function of h.

We expect that the coupling to phonons will likely be more significant with a greater out-of-plane displacement. We compute the Huang-Rhys factor for the singlet-singlet optical transition by evaluating Eq. 7.1. As shown in Fig. 7.2(b), the Huang-Rhys factor indeed increases as a function of the out-of-plane displacement. Our calculated Huang-Rhys factors are slightly larger than the experimentally observed value [149]. For the in-plane configuration, the Huang-Rhys factor is within the typical computational uncertainty, but deviates more significantly for large out-of-plane displacements. However, it has been suggested that the experimental Huang-Rhys factors are underestimated, due to the difficulty in distinguishing between zero-phonon

photons and those coupled to low-energy acoustic phonons [181].

Turning to the energetics, we calculate the zero-phonon line energy for both the singlet and triplet excited states (Fig. 7.3). The singlet excited state is responsible for the optical emission seen experimentally. We see that the energy depends quadratically on the out-of-plane displacement, as one might expect for a typical potential energy surface. Notably, a shift of up to 200 meV in the zero-phonon line is observed. This large shift results solely from the out-of-plane displacement; additional shifts would occur if one takes into account in-plane strain and changes in the dielectric environment. The magnitude of these shifts renders it very plausible that the DB can give rise to the range of zero-phonon line energies seen experimentally [148].

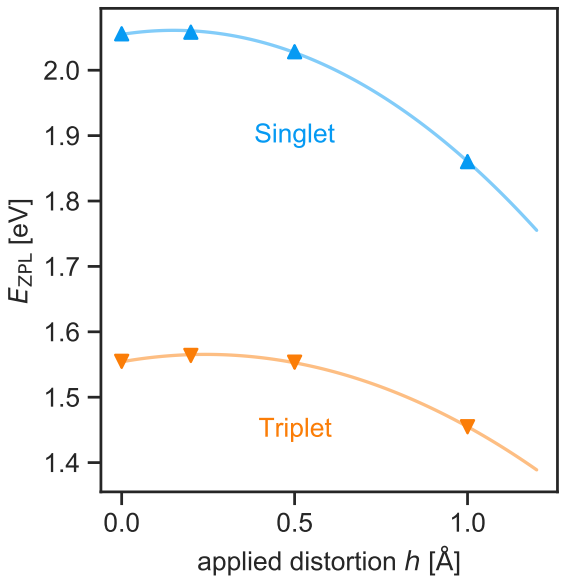

Figure 7.3: Zero-phonon line energy for the singlet (blue, up triangles) and triplet (orange, down triangles) excited states.

The triplet excited state is relevant for the intersystem crossing and therefore, for the observed magnetic-field dependence [88]. For the triplet excited state, the zero-

phonon line also varies quadratically with the out-of-plane displacement. This variation will inevitably influence the intersystem crossing rate. Along with the fact that the intersystem crossing is forbidden for C_{2v} symmetry, these results explain the variations in the magnetic-field dependence seen experimentally. Indeed, Exarhos *et al.* [88] noted that some emitters show no magnetic-field dependence, while other emitters showed a strong dependence, essentially doubling in brightness as a result of the applied magnetic field.

7.3.3 Radiative lifetime

For the 2-eV emitters, an anti-bunching lifetime of 1-10 ns is typically observed [148, 149]. The anti-bunching lifetime describes the characteristic timescale on which the emitted photons exhibit anticorrelation [184]. To understand the relation between the anti-bunching lifetime and the radiative lifetime calculated by Eq. 2.43, we must consider the quantum efficiency. The quantum efficiency η is defined as [87]

$$\eta = \frac{\Gamma_{\text{rad}}}{\Gamma_{\text{rad}} + \Gamma_{\text{nr}}}, \tag{7.2}$$

and Γ_{nr} is the total rate of nonradiative processes. The denominator in Eq. 7.2 is the total decay rate and is equivalent to the inverse of the anti-bunching lifetime, assuming the pump rate in experiments is much less than the decay rate. The 2-eV emitters have been found to have a quantum efficiency as low as 6-12% [185]; the radiative lifetime could therefore be as high as $10/0.06 \approx 167$ ns.

To understand the experimental measurements of the radiative lifetime, we first need to consider the geometry assumed in experiments. Experiments measure the "in-plane" dipole component, where it is assumed that the incoming light propagates along the z axis defined in Fig. 7.1(a); this implies the light is polarized in the x-y

plane. In the following analysis, we take "in-plane" to mean the x-y plane as defined in Fig. 7.1(a). An undistorted boron DB has C_{2v} symmetry and its dipole is out-of-plane. In C_{2v} symmetry, the transition for an in-plane dipole is forbidden; this can be seen from the fact that the ground-state wavefunction of the DB is totally symmetric within C_{2v}, and the excited-state p_z wavefunction is odd with respect to the z axis. Therefore, only a dipole transition along z is allowed. One might think that the boron DB cannot result in optical emission in the performed experiments. However, two additional issues need to be taken into consideration.

First, many experiments have been performed with h-BN flakes [148], which may be randomly oriented with respect to the incoming light. This means that the incoming light may not be aligned perfectly along the z axis, as defined with respect to the h-BN planes. We will refer to this situation as misalignment. When the system is misaligned, the out-of-plane dipole may be excited. We calculate the out-of-plane dipole to be 0.31 eÅ for the undistorted DB, which gives a radiative lifetime Eq. 2.43 of $\approx$ 140 ns, within the range of experimentally observed values.

Emitters have also been found to cluster near wrinkles [186]. The wrinkles also cause misalignment, making it possible for the out-of-plane dipole to be excited.

The second consideration is the fact that an out-of-plane displacement lowers the symmetry from C_{2v} to C_{1h}. In C_{1h} symmetry, the in-plane dipole transition is no longer forbidden; this can be understood as the p_z state tilting off the z axis, picking up an in-plane dipole component. In Fig. 7.4, we plot the radiative lifetime computed from Eq. 2.43 for the in-plane dipole component (as defined above).

Additionally, these two considerations may compound: both out-of-plane displacement and misalignment may be present simultaneously. Therefore, we also consider a 15°, 30°, and 45° misalignment between the incoming light and the h-BN plane

in Fig. 7.4. For these misalignment cases, "in-plane" is defined by rotating the coordinate system about the y axis through the misalignment angle. The combination of displacements and misalignment brings the computed radiative lifetime close to the experimentally observed values. We have also considered larger misalignment angles; as expected, the radiative lifetime is reduced even further.

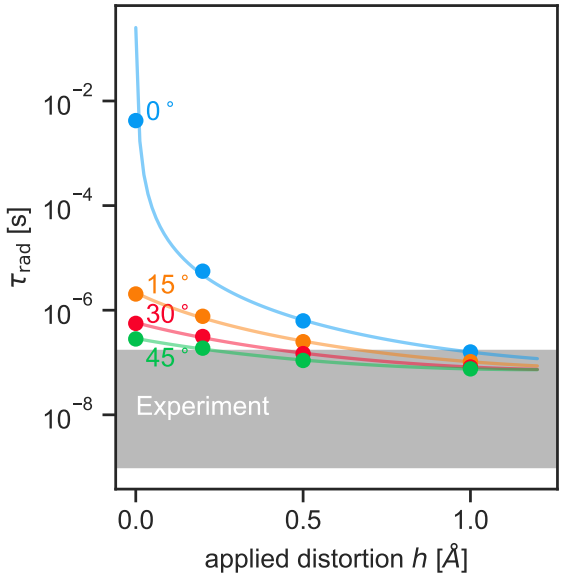

Figure 7.4: Radiative lifetime τ_{rad} computed using Eq. 2.43 for the in-plane (the x-y plane in Fig. 7.1) projection of the dipole (blue). We also consider a misalignment between the incoming light and the h-BN plane of 15° (orange), 30° (red), and 45° (green). For these misalignments, "in-plane" is defined by rotating the coordinate system by the misalignment angle about the y axis. The gray, shaded region is the range of radiative lifetimes observed in experiments, considering the quantum efficiency may be as low as 6% [185].

7.4 Discussion

The boron DB model provides a compelling explanation for the microscopic origin of the 2-eV emitters; its properties are consistent with a number of properties that have

been observed in detailed experimental studies.

The thermodynamic transition level, which determines the Fermi level position at which the defect changes its charge state, was measured to be in the upper-half of the band gap [187]. This is in agreement with the boron DB, where the optical transition is in the negative charge state, and the $(0/-)$ transition level is in the upper-half of the band gap. Indeed, the fact that the ground-state level is high in the gap means that for high enough excitation energies, the electron can be excited into the conduction band. We have proposed that the conduction band is the indirect state that Jungwirth and Fuchs [169] invoked to explain the observed misalignment of the absorptive and emissive dipole. In those experiments, Jungwirth and Fuchs surveyed a range of emitters with different zero-phonon lines and a fixed excitation energy. Recent experiments [188] confirmed our proposal more directly by using different color excitations on a single emitter and identifying a photoionization process.

In our calculations of the boron DB, we use a model in which an isolated DB is located in a small void. This is obviously an idealized situation, allowing us to study the properties of an (approximately) isolated DB within the constraints of our finite-size supercells. The actual geometry of realistic DBs may differ. We emphasize that the presence of hydrogen in the model system is not a relevant component of the boron DB model; the hydrogen atoms are present only to passivate other DBs on the internal surface of the small void. The essential features of the boron DB comprise the boron atom, the DB wavefunction, and the localized p_z state. In reality, there are many ways that a boron DB can be realized; it can be found at a flake edge [150] or it could be part of an extended defect [168].

Boron DBs could also be present in large voids, for which there is experimental evidence. Kozawa *et al.* [189] recently correlated the spread in the 2-eV emitters with

the presence of larger voids they observed with scanning transmission electron microscopy. Kozawa *et al.* [189] proposed specific structures for the voids, the internal surfaces of which are largely terminated with N atoms, as expected for h-BN [165]. However, single boron DBs can occur in the corners of the void. The interaction with nearby DBs on neighboring N atoms will likely increase the spread of emission energies.

Our present study has made clear that careful consideration of out-of-plane displacements is necessary to reconcile specific observations. We have provided concrete calculations demonstrating that DBs are sensitive to their local environment. Specifically, we found that distortions in the local environment produce an out-of-plane distortion, which admits an in-plane dipole component. We note that two separate recent experimental studies [190, 191] showed that the measured dipole has both an in-plane and out-of-plane component.

Lastly, we comment on the suggestion that a carbon-containing defect is responsible for the 2-eV emitters [192]. Mendelson *et al.* [192] showed that carbon incorporation influences the density of observable 2-eV emitters; however, this does not prove that the carbon atoms are part of the emitting defects. These samples have uncharacteristically high concentrations of carbon compared to typical material; it therefore seems odd that the observed density of emitters is still quite low.

We would like to draw attention to an alternate interpretation, under the assumption that dangling bonds are responsible for the single-photon emission: carbon may be indirectly affecting the density of single-photon-emitting dangling bonds, for instance by modifying the Fermi level. It is known that carbon is an electrically active impurity and may inevitably tune the Fermi level [138]. As we saw above, the Fermi level needs to be in the right range for a defect to be in the correct charge state to

give rise to the 2 eV emission. Mendelson *et al.* [192] tried to eliminate Fermi-level effects as the cause by showing that implantation with oxygen or silicon does not produce emitters; however, secondary effects due to oxygen or silicon implantation that suppress emitter formation cannot be excluded. Future studies to understand the interplay between carbon incorporation and emission from dangling bonds are clearly warranted.

7.5 Conclusions

In summary, we have presented a model for the 2-eV single-photon emitters in h-BN based on boron DBs, and demonstrated the effects of out-of-plane displacements. A distortion in a neighboring plane causes the DB to move out of plane and shifts the zero-phonon line towards lower energies. The accompanying increase in the in-plane dipole moment gives rise to radiative lifetimes which are consistent with experiment. We showed that the boron DB model explains several key features observed experimentally. Our work highlights the importance of considering out-of-plane displacements when studying the behavior of defects in 2D materials.

Permissions and Attributions

The content of Chapter 7 follows from work that has previously appeared in 2D Materials (Ref. [33]).

Chapter 8

Probing the Optical Dynamics of Quantum Emitters in Hexagonal Boron Nitride

8.1 Introduction

In Chapter 5, we introduced the 2 eV single-photon emitters in hexagonal boron nitride and what is known about them. One of the outstanding challenges that remains in the field is regarding the emitters' optical dynamics. Optical dynamics arise from the intricate interplay of radiative and nonradiative transitions composing a quantum emitter's electronic structure together. These transitions can arise from distinct processes such as electron-phonon interactions, intersystem crossings between different spin manifolds, and ionization or recombination events (described in Sec. 2.6.2).

In this Chapter we will present calculations on the optical dynamics that can be directly compared with the powerful experimental technique of photon emission cor-

relation spectroscopy (PECS) [89]. The second-order photon autocorrelation function $g^{(2)}(\tau)$, which is widely used to identify single-photon emitters, is the key quantity in PECS. One can distinguish between photon antibunching ($g^{(2)}(\tau) < 1$) as a signature of non-classical light, with single-photon emission as a special case when $g^{(2)}(0) = 0$, and photon bunching ($g^{(2)}(\tau) > 1$ for $\tau \neq 0$) as a signature of dark, metastable states accessed via nonradiative transitions. By probing $g^{(2)}(\tau)$ on long timescales, PECS provides insight into the number of electronic states contributing to the signal and the various transitions between them. The combined power of PECS and first-principles calculations provides strong evidence of the atomic and electronic structure of a given emitter.

In Sec. 8.2 we briefly discuss the PECS measurements performed by our experimental collaborators. The PECS measurements demonstrate that the quantum emitters (QEs) in hexagonal boron nitride possess a rich level structure connected by various radiative and nonradiative transitions. These transitions are associated with timescales spanning five orders of magnitude and hint at the importance of charge and spin dynamics in the optical dynamics. We assess the ability of the existing theoretical proposals for the microscopic origin of the source of the emission to explain these results. We perform quantitative calculations of nonradiative capture in the boron dangling bond and find that it agrees well with experiment. These combined results confirm that photoionization and subsequent re-capture may take place, and more generally, support the attribution of the microscopic origin to the boron dangling bond.

8.2 Experimental Measurements

Our experimental collaborators in the group of Prof. L. Bassett (U. Pennsylvania) performed careful PECS measurements. In this section, I briefly describe the experimental setup and results, which are relevant for a comparison to the computational results. More detailed information on the experiments, including the observation of $g^{(2)}(0) = 0$, can be found in Ref. [34].

8.2.1 Setup

The experimental setup used to probe the QEs in h-BN is shown in Fig. 8.1. Two different color excitation sources [532 nm (green) and 592 nm (orange)] are available, and the power of the excitation can be tuned. This setup enables measurements of wide-field, rastered micro-PL images. The emitted light is collected and passed through optical fibers to be sent to either a spectrometer or a beam splitter. The beam splitter is set up to enable a Hanbury Brown-Twiss interferometer, which allows for the measurement of $g^{(2)}(\tau)$.

8.2.2 Probing the Optical Dynamics

The measured micro-PL images and PL spectra for five QEs, labeled A-E, in h-BN are shown in Fig. 8.2. All of the measured spectra show the characteristic phonon sideband associated with the 2 eV QEs in h-BN. The measured zero-phonon line of the QEs ranges from 1.8 eV to 2.1 eV, and the associated Huang-Rhys factor, which characterizes the strength of coupling to phonons, ranges from 2.1 to 2.8. Also shown in Fig. 8.2 is the $g^{(2)}(\tau)$ on a nanosecond time scale; the characteristic antibunching dip is seen, demonstrating that the emitters are indeed quantum.

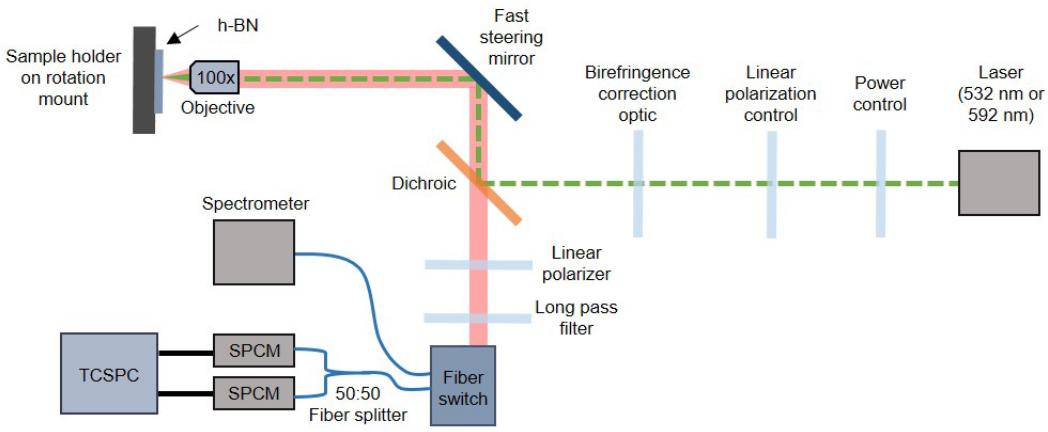

Figure 8.1: A simplified version of the room temperature optical setup showing the essential optical and electronic components used to probe the QEs in h-BN. The green dashed line represents the 532 nm (green) excitation path which can be switched to 592 nm (orange) excitation.

Next, PECS is performed by measuring $g^{(2)}(\tau)$ over long timescales; the timescales of interest for the QEs in h-BN span six orders of magnitude. Our collaborators use an empirical equation to fit $g^{(2)}(\tau)$ and extract the relevant antibunching and bunching rates. This equation is given by

$$g^{(2)}(\tau) = 1 - C_1 e^{-\gamma_1|\tau|} + \sum_{i=2}^{n} C_i e^{-\gamma_i|\tau|} , \tag{8.1}$$

where C_1 is the antibunching amplitude with corresponding rate γ_1, and C_i for $i > 1$ are the bunching amplitude with corresponding rate γ_i. n is the total number of rates extracted from the modeling. The best-fit parameters and corresponding n are determined by considering the Akaike information criterion and comparing the reduced chi-squared statistic (see the Supplemental Material of Ref. [34] for more details).

Figure 8.3 summarizes the results of fitting the empirical model of Eq. 8.1 to the PECS measurements as a function of optical excitation power. The PECS data for QEs B, D, and E are best described by a three-timescale model ($n = 3$), whereas QE A exhibits four resolvable timescales ($n = 4$). For QE C, two or three timescales can be

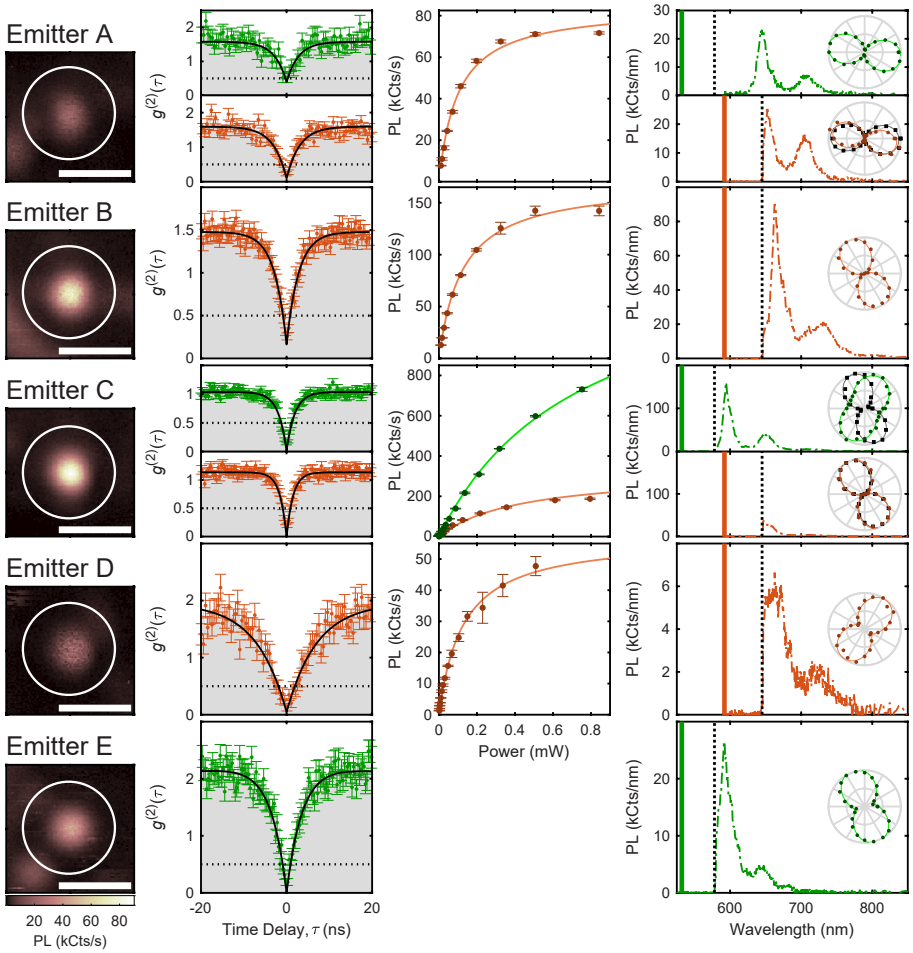

Figure 8.2: In all panels, data plotted in green (orange) were acquired under 532 nm (592 nm) excitation. **(Column 1)** micro-PL images of the QEs (circled), acquired under 592 nm (QEs A-D) or 532 nm (QE E) excitation. Scale bars denote 1 μm. **(Column 2)** Second-order photon autocorrelation function (colored points), fit using Eq. 8.1 as discussed in Ref. [34] (black curve). Error bars represent Poissonian uncertainties based on the photon counts in each bin. **(Column 3)** Steady-state, background-subtracted PL intensity as a function of excitation power (points), fit using an empirical saturation model discussed in Ref. [34] (solid curves). Error bars represent one standard deviation based on three measurement repeats. **(Column 4)** PL spectra and polarization data. Vertical colored lines represent the excitation laser wavelengths, and black dotted lines indicate cut-on wavelengths for long-pass optical filters in the collection path. Insets: PL intensity as a function of linear excitation polarization angle (colored circles) or filtered by linear polarization angle in emission (black squares). Solid curves are fits to the data using an empirical model discussed in Ref. [34].

resolved depending on the excitation power and wavelength. Each of the fitted parameters shows a dependence on the excitation power, with some exhibiting markedly different behavior.

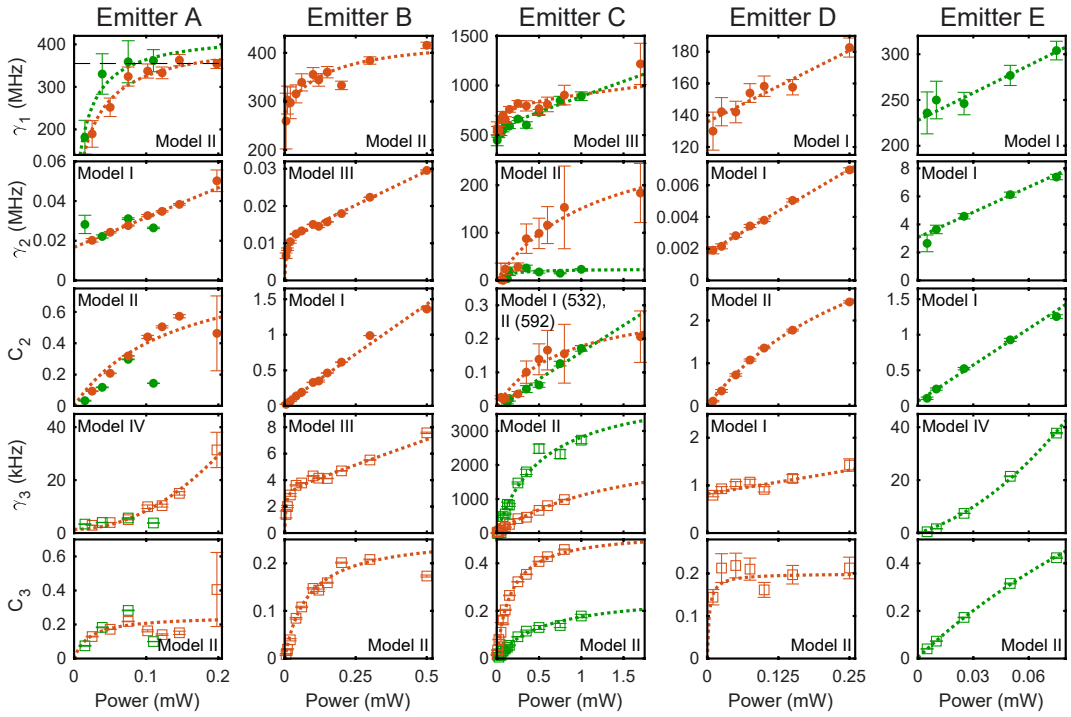

Figure 8.3: Excitation power and wavelength dependence of **(Row 1)** the antibunching rate (γ_1) denoted as circles, **(Row 2)** the bunching rate (γ_2) denoted as circles, **(Row 3)** the bunching amplitude (C_2) denoted as circles, **(Row 4)** the bunching rate (γ_3) denoted as squares, and **(Row 5)** the bunching amplitude (C_3) denoted as squares. The black dashed line (QE A) represents the lifetime extracted from a pulsed measurement. Orange (green) data correspond to excitation at 592 nm (532 nm). The error bars represent one standard deviation. For the purposes of this dissertation, the dotted lines are intended to guide the eye. The dotted lines are fits to empirical models of the excitation-power dependence, as discussed in Ref. [34].

The antibunching rate γ_1 exhibits a markedly nonlinear power dependence for QEs A, B, and C whereas the dependence appears to be linear for QEs D and E. However, the power range in the data for QEs D and E might not be large enough for nonlinearities to emerge. The zero-power antibunching-rate offset (R_0) for QEs B-E is

clearly nonzero, whereas the fit for QE A is poorly constrained, yielding $R_0 = 0 \pm 261$ MHz and $R_0 = 0 \pm 167$ MHz for green and orange excitation, respectively.

The bunching dynamics exhibit significant quantitative and qualitative variations across emitters. The fastest bunching rate γ_2 scales linearly with excitation power and has a non-zero offset for QEs A, D, and E, whereas it exhibits saturation behavior and zero offset for QEs B and C. The magnitudes of γ_2 range from several kilohertz (QEs A, B, and D) up to several megahertz or faster (QEs C and E). The slower bunching rate γ_3 exhibits the largest qualitative variation across emitters, including linear (QE D), quadratic (QEs A and E), and saturation models (QEs B and C). Only QE D exhibits clear evidence for a non-zero offset for γ_3. Quantitatively, the magnitudes of γ_3 are typically in the kilohertz range.

8.2.3 Electronic Model and Optical Dynamics Simulations

To understand the observed complex dynamics, simulations of the optical dynamics were performed by solving Eq. 2.48 as described in Sec. 2.6.2. The simulated $g^{(2)}(\tau)$ is fit with the empirical model of Eq. 8.1 to obtain the antibunching and bunching parameters that can be directly compared with the experiments. The effect of noise and limited timing resolution on the simulated $g^{(2)}(\tau)$ is included (as described in Ref. [34]). A four-level electronic model, shown in Fig. 8.4(a), is sufficient to capture the relevant physics. The four-level model consists of a ground state (level 1), an excited radiative state (level 2), a higher-lying excited state (level 3) and a nonradiative metastable state (level 4).

There are two optical excitation pathways from the ground state to excited states 2 or 3, represented by the rates Γ_{12} and Γ_{13}, respectively. The magnitude of these two rates depends on the corresponding optical cross section for absorption, which

depends on the excitation wavelength (resonance), dipole matrix element, and vibrational coupling. In the simulations, $\Gamma_{12} = 0$ under the assumption that $\Gamma_{12}/\Gamma_{13} \ll 1$, which is motivated by assuming the excitation is on resonance with the higher-lying excited state (level 3). In this way, the simulations emphasize an indirect excitation mechanism ($1 \rightarrow 3 \rightarrow 2$) prior to optical emission ($2 \rightarrow 1$). The validity of this assumption is checked by varying Γ_{12}/Γ_{13}: there is no qualitative difference in the results (discussed in Ref. [34]).

In addition to the indirect excitation mechanism, optical excitation results in population and relaxation of the metastable state 4 *via* nonradiative transitions with rates κ_{24} and κ_{41}. Two types of nonradiative transition mechanisms for the metastable state can be considered: spontaneous and optically pumped. Spontaneous transition rates are independent of the optical excitation rate (in this case, Γ_{13}), whereas optically pumped transition rates scale linearly with Γ_{13}. In this model, the optically pumped transition rates κ_{24} and κ_{41} can approximate more complicated processes; for example, they could involve re-pumping ($2 \rightarrow 3$ or $4 \rightarrow 3$) with subsequent nonradiative relaxation. Alternatively, they could involve transient population of additional levels. Their approximation as individual pumped transitions remains accurate as long as optical pumping remains the rate-limiting step.

Figure 8.4 summarizes the results of optical dynamics simulations for this model. Notably, $n = 2$ is sufficient to fit the simulated data, despite having four levels in the model. This is because the indirect excitation mechanism is obscured by the included, realistic measurement noise; as a result, the fitting procedure results in $n = 2$ and a nonlinear power-scaling of the anti-bunching rate γ_1, which coincides with the behavior of QEs A, B, and C. Obtaining $n = 2$ is also independent of the choice of spontaneous or optically pumped nonradiative transitions. However, the key observ-

able difference manifests in the excitation power dependence of the corresponding bunching rate γ_2 [Fig. 8.4(d)]. γ_2 for spontaneous transitions features a non-zero zero-power offset and saturates at high power, whereas γ_2 for optically pumped transitions has zero offset and scales nearly linearly with power. In both cases, the corresponding bunching amplitude C_2 saturates [Fig. 8.4(e)].

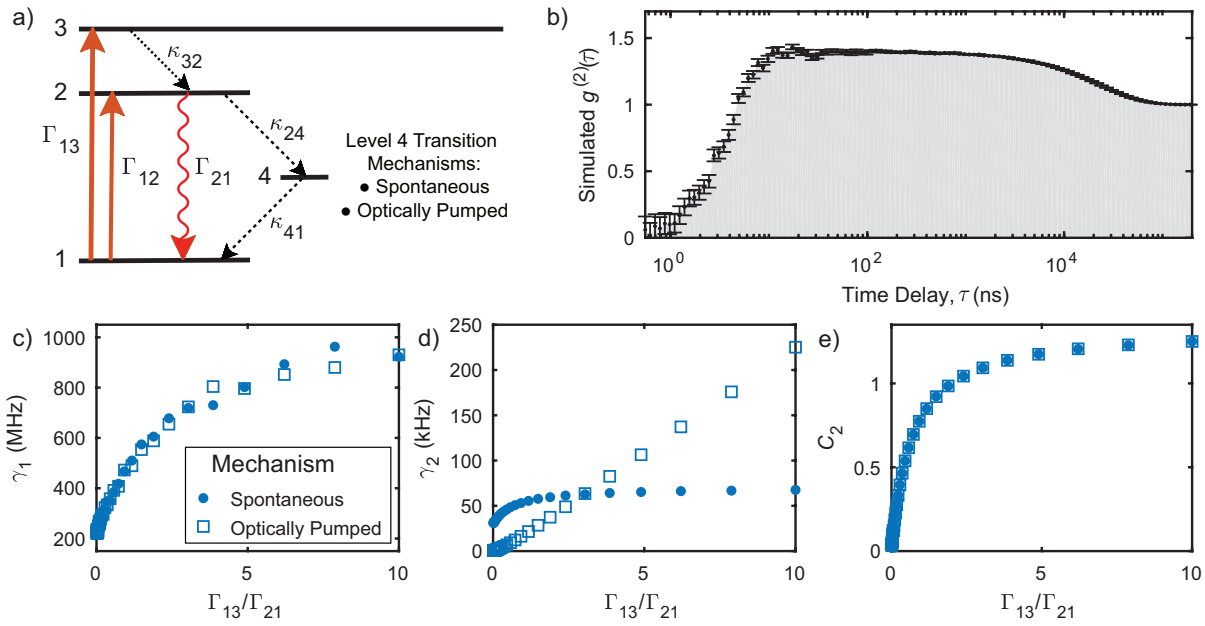

Figure 8.4: **(a)** An investigative four-level electronic model consisting of the ground state (level 1), radiative state (level 2), excited state (level 3), and metastable state (level 4). Orange arrows represent excitation pathways (with rates Γ_{12} and Γ_{13}), the wavy red arrow represents radiative emission (with rate Γ_{21}), and dotted black arrows represent nonradiative transitions (with rates κ_{32}, κ_{24} and κ_{41}). **(b)** Simulated $g^{(2)}(\tau)$ for $\Gamma_{12} = 0$, $\Gamma_{13} = 84$ MHz, $\Gamma_{21} = 300$ MHz, $\kappa_{32} = 600$ MHz, $\kappa_{24} = 60$ kHz, and $\kappa_{41} = 30$ kHz. Error bars represent simulated photon shot noise. **(c-e)** Best-fit parameters γ_1, γ_2, and C_2 determined by fitting simulated $g^{(2)}(\tau)$ data using Eq. 8.1 with $n = 2$. The results are plotted as a function of Γ_{13}/Γ_{21}, where $\Gamma_{21} = 300$ MHz is a fixed parameter.

8.2.4 Implications of the Measurements

The PECS experiments, summarized in Fig. 8.3, reveal key details regarding the nature of the QEs' excited states and optical dynamics. All QEs feature antibunching and two or more bunching timescales in their autocorrelation spectra, which implies that the optical dynamics involve at least four electronic levels. This observation indicates the presence of metastable dark states in the optical dynamics, broadly consistent with previous work [149, 161, 193–196]. Here we discuss two key features of the PECS measurements in the context of the optical dynamics simulations: the nonlinear power dependence of the antibunching rate γ_1 that is clearly observed for QEs A, B, and C; and the diverse power-dependent variation of the bunching rates and amplitudes.

For a direct optical transition between ground state and radiative excited state (i.e., without level 3 in Fig. 8.4), the antibunching rate γ_1 scales linearly as a function of optical excitation power. The zero-power offset would then correspond to the QE's spontaneous emission rate. This is even the case for QEs that feature metastable charge and spin states, such as the NV center in diamond [197], which has been confirmed with explicit measurements (see Supplemental Figure S5 in Ref. [34]). The PECS observations of h-BN's QEs in row 1 of Fig. 8.3 defy this expectation. The power-scaling of γ_1 for QEs A, B, and C is clearly sublinear, exhibiting saturation behavior with a steep slope at low power. Furthermore the zero-power offset for γ_1 in QEs A and B is consistent with zero but poorly constrained due to the steep low-power slope; the offset is non-zero for QEs C, D, and E. In contrast to the other QEs, QEs D and E exhibit linear power-scaling of γ_1, but saturation behavior at higher power cannot be ruled out. Previous studies of QEs in h-BN contain hints of power-independent antibunching [194] and nonlinear power scaling [161, 195] without a satisfactory explanation.

These peculiar observations can be explained with optical dynamics simulations. As discussed in the previous section, the nonlinear dependence of the antibunching rate γ_1 on excitation power is a direct result of the indirect excitation mechanism. In the indirect excitation mechanism, level 3 is first populated and the nonradiative transition to level 2 (κ_{32}) is the rate-limiting step. When $\Gamma_{12}/\Gamma_{13} \ll 1$, the antibunching rate γ_1 saturates to $\kappa_{32} + \Gamma_{21}$ at high excitation power. For $\Gamma_{12}/\Gamma_{13} > 1$, the qualitative conclusion is the same, the dependence is still nonlinear; however, the fast, direct excitation may also populate level 2 but is unresolvable when realistic assumptions on the noise and timing resolution are included. These results rationalize the previous experimental observations and provide insight into the complicated dynamics that are involved in the antibunching rate. Furthermore, it provides new support for the indirect excitation model that was previously proposed [169].

The optical dynamics simulations also provide insight into the behavior of the bunching rates. As discussed in the previous section, two different types of nonradiative transitions, spontaneous and optically pumped, are possible and have qualitatively different results. Spontaneous transitions give rise to a bunching rate with non-zero offset and saturation behavior at high pump power. Intersystem crossing or general nonradiative relaxation would be characterized as a spontaneous transition. Optically pumped transitions have a bunching rate with zero offset and increase quasi-linearly. Ionization and recombination can be characterized as optically pumped transitions. Thus by investigating the power dependence of the bunching rates, one can gain insight into the spin and charge dynamics of the QE. Similar models have been used for QEs in h-BN [161, 195] and the silicon-vacancy center [198] in diamond.

Indeed both bunching behaviors, spontaneous and optically pumped, are present

in Fig. 8.3. Simulations of the four-level model give rise to one bunching component, while in experiments two or more bunching components were observed. Thus a model with more levels would be necessary to reproduce the experimental results; however, the single bunching component can be used to understand the qualitative behavior of each independent bunching component. Interestingly, some emitters (e.g., QEs A, B, D, and E) have a bunching component with non-zero offset but increase linearly with power. This behavior can be reproduced with the simulation if one allows the nonradiative transitions (κ_{24} and κ_{41}) to have both a spontaneous and optically pumped component. In this way, there may be multiple nonradiative pathways to level 4, which may include both spin and charge dynamics. For example, this level 4 could be a different spin configuration that is accessed through intersystem crossing, but is close enough to the conduction band to be photoionized at this excitation energy. These qualitative observations, along with the quantitative values extracted from the simulations, present an opportunity to compare with theoretical predictions.

8.3 First-Principles Calculations

The calculations performed in this study follow the same methodology as Sec. 5.2. To calculate the nonradiative capture coefficient, we utilize the formalism of Ref. [23] implemented in the Nonrad code [22] (discussed in Chapter 3).

We calculate the nonradiative capture coefficient C_n for the capture of an electron from the conduction band into the boron dangling bond. We will focus on the ground state [level 1 in Fig. 8.4(a)] and the optically active excited state [level 2 in Fig. 8.4(a)] of the dangling bond, which are separated by 2.06 eV [31]. In equilibrium, the dangling bond is in the negative charge state and is occupied by two electrons. When the

excitation energy is sufficiently large, an electron can be excited into the conduction band and the dangling bond is photoionized, changing the charge state from negative to neutral [process Γ_{13} in Fig. 8.4(a)]. Subsequent re-capture of this electron returns the dangling bond to the negative charge state. We consider two potential scenarios for this nonradiative process mediated by electron-phonon coupling: (1) The electron is captured directly into the ground state of the dangling bond, with rate κ_{31} [not depicted in Fig. 5(a)], or (2) the electron is captured into the excited state of the dangling bond [κ_{32} in Fig. 8.4(a)]. Process (2) puts the defect in the optically active excited state, from which a photon can then be emitted, with an emissive dipole unaligned with the absorptive dipole.

To evaluate the nonradiative capture coefficients, we extract several parameters from our density functional theory calculations: the transition energy, the phonon frequencies in the initial (i) and final (f) states $\Omega_{i/f}$, the mass-weighted root-mean-square difference in atomic geometries ΔQ, and the electron-phonon coupling matrix element W_{if}. The transition level for capture into excited state, which is used to determine the transition energy, is above the conduction-band minimum, while the single-particle states are in the gap. For the purposes of our capture coefficient evaluation, we shift the transition energy to be consistent with the 200 meV difference observed experimentally [169]; we verified that the conclusions are insensitive to the choice of the energy shift. The degeneracy factor in the nonradiative rate [22] is set to 1 since the dangling bond does not possess any configurational degeneracy. A scaling factor that accounts for charged defect interactions (see Sec. III. E. of Ref. [23]) is not necessary in this case because capture occurs in the neutral charge state and the electron-phonon coupling is evaluated in the neutral charge state.

At room temperature, we calculate C_n for capture into the ground state to be 1.2 $\times$

10^{-12} cm^3 s^{-1} and into the excited state to be 1.2×10^{-7} cm^3 s^{-1}. We can thus safely assume that capture into the excited state will dominate. These capture coefficients are larger than typical radiative capture coefficients, which are on the order of 10^{-13} - 10^{-14} cm^3 s^{-1} [76], justifying our implicit assumption of nonradiative rather than radiative capture.

In Chapter 7, we demonstrated the importance of out-of-plane distortions for understanding the behavior of the dangling bond in realistic hexagonal boron nitride samples. Here we include the effect of out-of-plane distortions on the capture coefficient, following the approach of Chapter 7. The influence of the out-of-plane distortion on the calculated parameters is shown in Fig. 8.5. For comparison purposes, we will use the average at room temperature 4×10^{-7} cm^3 s^{-1} as a representative value for capture into the excited state.

8.4 Consistency with Theoretical Proposals

Several defect structures have been proposed as the origin of visible-wavelength single-photon emission in h-BN, including the boron dangling bond (DB) [31], V_N-N_B [155], V_N-C_B [199], and V_B-C_N [192]. The negatively-charged boron vacancy V_B^- has been suggested to give rise to an optically detected magnetic resonance signal observed for emitter ensembles [154]; however V_B^- has a ZPL of ~1.7 eV and couples more strongly to phonons ($S_{HR} \sim 3.5$) [153], producing a PL band between 800-900 nm that does not overlap with the emitters considered here. Early studies highlighted V_N-N_B as the potential origin of visible QEs [155], but recent calculations show that the coupling to phonons is substantially larger than observations [199]. More recently, V_B-C_N has been proposed based on the observation that carbon is correlated with

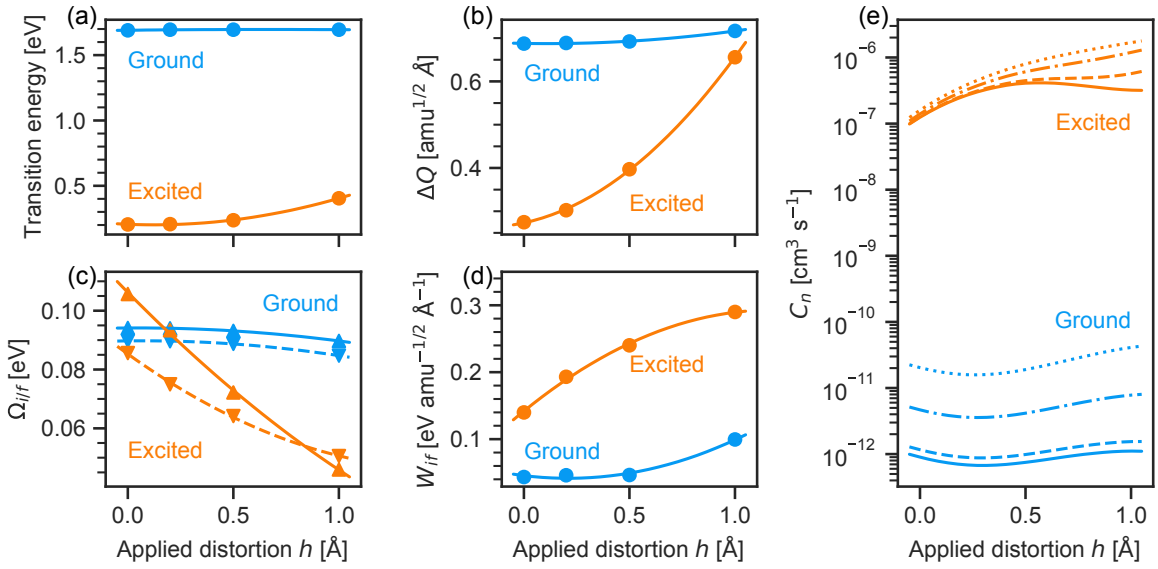

Figure 8.5: Calculated **(a)** transition energy, **(b)** mass-weighted root-mean-square difference in atomic geometries, **(c)** initial (up triangle) and final (down triangle) phonon frequencies, and **(d)** electron-phonon coupling matrix elements as a function of the applied distortion h. The lines are a quadratic fit to the calculated parameters and are intended to guide the eye. The calculated **(e)** electron capture coefficient at 10 K (solid), 300 K (dashed), 600 K (dashed dotted), and 900 K (dotted). The parameters for capture into the ground state are shown in blue and the excited state are shown in orange.

the emission signal, but the calculated PL spectrum [192] does not match the observations. The V_B-C_N calculations also predict a single, linearly-polarized absorption dipole, which is inconsistent with the measurements described in Sec. 8.2. The calculated PL spectrum and strain dependence of V_N-C_B [199] are in reasonable agreement with the observations stated in Sec. 8.2. However, the optical transition for V_N-C_B occurs in the triplet channel, while the calculated ground state is a singlet; the authors did not propose a mechanism through which the triplet channel is populated quickly enough to give rise to the optical emission they considered.

The boron DB is predicted to possess an optical transition at 2.06 eV with a Huang-Rhys factor of 2.3 (discussed in Chapter 5), which is in close agreement with the values

observed in this study. In addition, the variations in ZPL and S_{HR} for the observed emitters can be explained by out-of-plane distortions (discussed in Chapter 7). The ground state of the boron DB is a singlet, and the predicted existence of a triplet excited state can explain the presence of level 4 in Fig. 8.4(a). Another important feature of the boron DB model is the proximity of the states to h-BN's conduction band; this allows electrons to be optically excited directly into the conduction band, depending on the excitation energy, explaining the misalignment of the absorptive and emissive dipole when the excitation energy is increased. Other proposed models do not provide an explanation for the misalignment. For instance, in the case of V_{N}-C_{B} the optical transition occurs in the neutral charge state, and for the excitation energies considered here, photoionization will not occur [159].

Within the boron DB model, we would interpret level 3 in Fig. 8.4(a) as the conduction band and κ_{32} as the nonradiative capture rate. To support this interpretation, we have estimated the relevant capture rate κ_{32} of a photoionized electron from the conduction-band minimum into the DB excited state [level 2 in Fig. 8.4(a)]. This capture rate is a product of a capture coefficient and the density of electrons in the conduction band. A first-principles calculation yields a capture coefficient of 4×10^{-7} cm^3 s^{-1} (see Sec. 8.3). The density of electrons is estimated based on the thermal velocity of the photoionized electron ($\sim 10^5$ m s^{-1}) and a typical electron energy relaxation time of ~ 1 ps [200]. In the time it takes the electron to relax to the conduction-band minimum, it can thus travel ~ 100 nm; this distance corresponds to an effective electron density of 2.4×10^{14} cm^{-3}. Multiplying this value with the calculated capture coefficient gives a rate of $\kappa_{32} \sim 100$ MHz, in compelling agreement with the observed saturation antibunching rates of $\gamma_1 \sim$ 300-800 MHz for QEs A, B, and C. Our calculations also show that capture into the excited state is favored over capture into the

ground state by more than 5 orders of magnitude, justifying the neglect of κ_{31} in the general model of Fig. 8.4(a).

The inclusion of photoionization allows us to further rationalize the heterogeneity in bunching behavior of the observed emitters: the photoionized electron is not necessarily re-captured at the same QE, but may instead be captured by a neighboring defect, leaving the QE in a nonfluorescent, ionized configuration that likely requires optical excitation of additional free electrons to restore emission *via* subsequent electron capture. This process would be represented in Fig. 8.4(a) by an optically pumped transition, where level 4 represents an ionized state of the QE. The emitters may therefore be highly sensitive to the local defect environment. Unlike other proposed defect models, we conclude that the boron DB model is thus capable of explaining numerous aspects of the experimental observations, lending support to this proposed microscopic structure.

8.5 Conclusions

The experimental observations performed by our collaborators at the University of Pennsylvania reveal that h-BN's QEs have intricate electronic level structures and complex optical dynamics. The power dependence of the antibunching rate shows strong evidence of an indirect excitation mechanism, which had been previously invoked to explain the absorptive and emissive dipole misalignment [169]. This behavior is in stark contrast to the behavior of "typical" QEs, like the NV center in diamond. Each QE exhibited two or more bunching components and several distinct motifs for the respective power dependence. The power dependence hinted at the presence of both spontaneous and optically pumped transitions. We rigorously evaluated several

theoretical models in the context of these experimental observations. We conclude that the boron dangling bond is most consistent with these observations and quantitatively compared the calculated electron capture rate with the value extracted from the PECS measurements, finding excellent agreement. Indeed the boron dangling bond can rationalize much of the heterogeneity observed in the experiments, as well as others. These results demonstrate the combined power of PECS and first-principles calculations to resolve complex dynamics and provide microscopic insight into the behavior of QEs.

Permissions and Attributions

The content of Chapter 8 follows from work that has previously appeared as a preprint on the arXiv (Ref. [34]). This work was performed in collaboration with Raj N. Patel, Dr. David A. Hopper, Jordan A. Gusdorff, Tzu-Yung Huang, Rebecca E. K. Fishman, Benjamin Porat, and Prof. Lee C. Bassett; these collaborators performed the experimental measurements and optical dynamics simulations.

Chapter 9

Conclusions and Outlook

In this dissertation, I developed and applied first-principles computational techniques to build a coherent understanding of quantum defects. Quantum defects are a leading platform to power the second quantum revolution; indeed they can be expected to have a transformative impact on the field of quantum information science, which includes quantum computing, quantum communication, and quantum metrology.

We began by reviewing the theory surrounding first-principles calculations and their application to quantum defects in Chapter 2. In Chapter 3, we discussed the development of the `Nonrad` code, which implements a first-principles approach to evaluate the nonradiative transition rate. The approach handles both nonradiative capture and internal transitions via a quantum-mechanical description. We described how to evaluate the electron-phonon coupling matrix elements within the projector augmented wave potential formalism. Furthermore, we demonstrated that the common practice of replacing Dirac delta functions with Gaussians to mimic broadening can introduce errors into the resulting rate; we implemented an alternative approach based on interpolation to overcome this. Lastly, we took a close look at the approx-

imations used in attaining an analytic description of the Sommerfeld parameter. We found that the approximation is not valid at high temperatures and suggest numerical evaluation as an alternative.

We then turned towards applications of the methodology to novel quantum defects. Boron nitride is an appealing host for quantum defects due to its ultrawide band gap, as well as excellent thermal and chemical stability. In Chapter 4, we examined *n*-type dopants and native vacancies in cubic boron nitride. Realizing cubic boron nitride for applications in electronics, optoelectronics, and quantum information science is predicated on controllable dopability. We identified O_N and Si_B as promising *n*-type dopants. However, native vacancies pose a problem for *n*-type conductivity: we suggested control of growth kinetics to overcome this. Lastly, we analyzed the propensity of the investigated defects as potential quantum defects.

Next, we focused on hexagonal boron nitride, which is the two-dimensional polymorph of boron nitride; hexagonal boron nitride is a layered material where the layers are bound by a weak van der Waals interaction. Thus it is possible to obtain quantum defects embedded in a single monolayer of hexagonal boron nitride. This would overcome the issues surrounding utilizing quantum defects near a surface, which is a major source of noise and decoherence. Single-photon emitters in the visible spectrum had been observed in hexagonal boron nitride. In Chapter 5, we proposed boron dangling bonds as the likely microscopic origin of the emission. Boron dangling bonds give rise to an optical transition at 2.06 eV with coupling to phonons characterized by a Huang-Rhys factor of 2.3. The ground state of the dangling bond is a singlet, but a metastable triplet state exists, which would give rise to magnetic-field-dependent emission. These properties are in good agreement with the experimental observations.

In Chapter 6, we investigated the properties of the boron dangling bond in a single

monolayer of hexagonal boron nitride. Such a study is necessary to realize the benefits of a two-dimensional host material for quantum defects. We found that the properties of the dangling bond were largely unchanged; however, the geometry of the metastable triplet state slightly differs and may result in differences in the magnetic-field dependence. It is appealing to idealize two-dimensional materials as infinitely flat plans, but reality is not so kind. Two-dimensional materials exist in three dimensions, and may bend or distort. We studied the effects of an out-of-plane distortion on the boron dangling bond in Chapter 7. The zero-phonon line and coupling to phonons respond to the perturbation, which demonstrates that the dangling bond may be sensitive to the local environment. We also studied the radiative transition rate and found it to be in agreement with experiment.

This work in characterizing the boron dangling bond culminated in a collaborative investigation of the optical dynamics, discussed in Chapter 8. Experimentally, the photon autocorrelation function was measured and used to extract the level structure and transition rates of single-photon emitters in hexagonal boron nitride. The extracted level structure agrees well with that of the dangling bond. We quantitatively evaluated the nonradiative capture rate for the dangling bond. We found that capture into the excited state was favored by several orders of magnitude and the resulting rate agrees well with experiment. This result confirms our prediction on the role of photoionization. By comparing with other theoretical models for the emission, we concluded that boron dangling bonds provide a consistent explanation for the experimental observations.

In total, we have utilized first-principles calculations to address several outstanding issues related to quantum defects. The ability to predict nonradiative transition rates from first principles will be an invaluable tool for computational scientists. Still

there are outstanding challenges to be addressed for a full characterization of quantum defects from first principles. Dangling bonds were once viewed as detrimental defects that needed to be mitigated; this work shines new light on them, as useful defects that can be controlled to achieve feats of quantum information science. Even so, there is a lack of consensus in the community on the origin of the 2 eV single-photon emission in hexagonal boron nitride.

There is more work to be done, however. Regarding the boron dangling bond, several of the transition rates remain to be calculated. The photoionization cross sections for the transition out of the singlet ground state, singlet excited state, and the triplet metastable state should be evaluated. Likewise the absorption cross section for the internal transition in the dangling bond could be calculated and compared to the photoionization cross sections. This comparison would further clarify the power-dependent excitation rates in the optical dynamics of the dangling bond.

The largest remaining computational challenge is regarding the intersystem crossing rates for the dangling bond (and other quantum defects). Evaluating the intersystem crossing rate will require several methodological developments. First and foremost, an approach to evaluate the spin-orbit coupling matrix elements at a consistent level of theory is necessary. Second, it may be necessary to go beyond the single-mode approximation. This is because the Huang-Rhys factors are relatively small for intersystem crossing processes, which is where the single-mode approximation is expected to fail [83]. Furthermore, the first-order intersystem crossing is forbidden by symmetry in many cases; thus the second-order process will need to be addressed, for which the details of coupling to phonons cannot be captured with a single-mode approximation. With the successful development of a formalism to calculate the intersystem crossing rate, a fully first-principles evaluation of the optical dynamics of a

given quantum defect would be possible.

We hope that the complete picture painted in this dissertation will help to bring the community closer to understanding and controlling these quantum defects.

Bibliography

[1] J. P. Dowling and G. J. Milburn, *Quantum technology: The second quantum revolution*, Phil. Trans. R. Soc. A **361**, 1655 (2003).

[2] R. Materese, B. P. Stein, and J. Huergo, The Second Quantum Revolution, https://www.nist.gov/topics/physics/introduction-new-quantum-revolution/second-quantum-revolution (2018).

[3] D. P. DiVincenzo, *The Physical Implementation of Quantum Computation*, Fortschr. Phys. **48**, 771 (2000).

[4] N. Gisin and R. Thew, *Quantum communication*, Nat. Photonics **1**, 165 (2007).

[5] T. E. Northup and R. Blatt, *Quantum information transfer using photons*, Nat. Photonics **8**, 356 (2014).

[6] C. L. Degen, F. Reinhard, and P. Cappellaro, *Quantum sensing*, Rev. Mod. Phys. **89**, 035002 (2017).

[7] J. Preskill, *Quantum computing: Pro and con*, Proc. Royal Soc. Lon. A **454**, 469 (1998).

[8] C. E. Dreyer, A. Alkauskas, J. L. Lyons, A. Janotti, and C. G. Van de Walle, *First-*

Principles Calculations of Point Defects for Quantum Technologies, Annu. Rev. Mater. Res. **48**, 1 (2018).

[9] J. R. Weber, W. F. Koehl, J. B. Varley, A. Janotti, and B. B. Buckley, *Quantum computing with defects*, Proc. Natl. Acad. Sci. U.S.A. **107**, 8513 (2010).

[10] M. E. Turiansky, A. Alkauskas, and C. G. Van de Walle, *Spinning up quantum defects in 2D materials*, Nat. Mater. **19**, 487 (2020).

[11] Á. Gali, *Ab initio theory of the nitrogen-vacancy center in diamond*, P. Soc. Photo-opt. Ins. **8**, 1907 (2019).

[12] M. Pelliccione, A. Jenkins, P. Ovartchaiyapong, C. Reetz, E. Emmanouilidou, N. Ni, and A. C. Bleszynski Jayich, *Scanned probe imaging of nanoscale magnetism at cryogenic temperatures with a single-spin quantum sensor*, Nat. Nanotechnol. **11**, 700 (2016).

[13] A. Jenkins, M. Pelliccione, G. Yu, X. Ma, X. Li, K. L. Wang, and A. C. B. Jayich, *Single-spin sensing of domain-wall structure and dynamics in a thin-film skyrmion host*, Phys. Rev. Mater. **3**, 083801 (2019).

[14] T. R. Eichhorn, C. A. McLellan, and A. C. Bleszynski Jayich, *Optimizing the formation of depth-confined nitrogen vacancy center spin ensembles in diamond for quantum sensing*, Phys. Rev. Mater. **3**, 113802 (2019).

[15] M. Pompili, S. L. N. Hermans, S. Baier, H. K. C. Beukers, P. C. Humphreys, R. N. Schouten, R. F. L. Vermeulen, M. J. Tiggelman, L. dos Santos Martins, B. Dirkse, S. Wehner, and R. Hanson, *Realization of a multinode quantum network of remote solid-state qubits*, Science **372**, 259 (2021).

[16] W. Pfaff, B. J. Hensen, H. Bernien, S. B. van Dam, M. S. Blok, T. H. Taminiau, M. J. Tiggelman, R. N. Schouten, M. Markham, D. J. Twitchen, and R. Hanson, *Unconditional quantum teleportation between distant solid-state quantum bits*, Science **345**, 532 (2014).

[17] H. Bernien, B. Hensen, W. Pfaff, G. Koolstra, M. S. Blok, L. Robledo, T. H. Taminiau, M. Markham, D. J. Twitchen, L. Childress, and R. Hanson, *Heralded entanglement between solid-state qubits separated by three metres*, Nature **497**, 86 (2013).

[18] A. Alkauskas, B. B. Buckley, D. D. Awschalom, and C. G. Van de Walle, *First-principles theory of the luminescence lineshape for the triplet transition in diamond NV centres*, New J. Phys. **16**, 073026 (2014).

[19] L. V. H. Rodgers, L. B. Hughes, M. Xie, P. C. Maurer, S. Kolkowitz, A. C. Bleszynski Jayich, and N. P. de Leon, *Materials challenges for quantum technologies based on color centers in diamond*, MRS Bulletin **46**, 623 (2021).

[20] S. Sangtawesin, B. L. Dwyer, S. Srinivasan, J. J. Allred, L. V. H. Rodgers, K. De Greve, A. Stacey, N. Dontschuk, K. M. O'Donnell, D. Hu, D. A. Evans, C. Jaye, D. A. Fischer, M. L. Markham, D. J. Twitchen, H. Park, M. D. Lukin, and N. P. de Leon, *Origins of diamond surface noise probed by correlating single-spin measurements with surface spectroscopy*, Phys. Rev. X **9**, 031052 (2019).

[21] D. Bluvstein, Z. Zhang, and A. C. B. Jayich, *Identifying and Mitigating Charge Instabilities in Shallow Diamond Nitrogen-Vacancy Centers*, Phys. Rev. Lett. **122**, 076101 (2019).

[22] M. E. Turiansky, A. Alkauskas, M. Engel, G. Kresse, D. Wickramaratne, J.-X. Shen, C. E. Dreyer, and C. G. Van de Walle, *Nonrad: Computing nonradiative capture coefficients from first principles*, Comput. Phys. Commun. **267**, 108056 (2021).

[23] A. Alkauskas, Q. Yan, and C. G. Van de Walle, *First-principles theory of nonradiative carrier capture via multiphonon emission*, Phys. Rev. B **90**, 075202 (2014).

[24] M. E. Turiansky, J.-X. Shen, A. Alkauskas, and C. G. Van de Walle, Nonrad (2020).

[25] X. Zhang, M. E. Turiansky, and C. G. Van de Walle, *All-inorganic halide perovskites as candidates for efficient solar cells*, Cell Rep. Phys. Sci. **2**, 100604 (2021).

[26] X. Zhang, M. E. Turiansky, and C. G. Van de Walle, *Correctly Assessing Defect Tolerance in Halide Perovskites*, J. Phys. Chem. C **124**, 6022 (2020).

[27] X. Zhang, M. E. Turiansky, J.-X. Shen, and C. G. Van de Walle, *Defect tolerance in halide perovskites: A first-principles perspective*, J. Appl. Phys. **131**, 090901 (2022).

[28] X. Zhang, M. E. Turiansky, J.-X. Shen, and C. G. Van de Walle, *Iodine interstitials as a cause of nonradiative recombination in hybrid perovskites*, Phys. Rev. B **101**, 140101 (2020).

[29] X. Zhang, J.-X. Shen, M. E. Turiansky, and C. G. Van de Walle, *Minimizing hydrogen vacancies to enable highly efficient hybrid perovskites*, Nat. Mater. **20**, 971 (2021).

[30] M. E. Turiansky, D. Wickramaratne, J. L. Lyons, and C. G. Van de Walle, *Prospects for n-type conductivity in cubic boron nitride*, Appl. Phys. Lett. **119**, 162105 (2021).

[31] M. E. Turiansky, A. Alkauskas, L. C. Bassett, and C. G. Van de Walle, *Dangling bonds in hexagonal boron nitride as single-photon emitters*, Phys. Rev. Lett. **123**, 127401 (2019).

[32] M. E. Turiansky and C. G. Van de Walle, *Boron dangling bonds in a monolayer of hexagonal boron nitride*, J. Appl. Phys. **129**, 064301 (2021).

[33] M. E. Turiansky and C. G. Van de Walle, *Impact of dangling bonds on properties of h-BN*, 2D Mater. **8**, 024002 (2021).

[34] R. N. Patel, D. A. Hopper, J. A. Gusdorff, M. E. Turiansky, T.-Y. Huang, R. E. K. Fishman, B. Porat, C. G. Van de Walle, and L. C. Bassett, Probing the optical dynamics of quantum emitters in hexagonal boron nitride (2022), arXiv:2201.08881 .

[35] R. M. Martin, *Electronic Structure: Basic Theory and Practical Methods* (Cambridge University Press, Cambridge, UK, 2004).

[36] M. Born and R. Oppenheimer, *Zur Quantentheorie der Molekeln*, Ann. Phys. **389**, 457 (1927).

[37] P. W. Anderson, *Basic Notions of Condensed Matter Physics*, 55 (Benjamin/Cummings Pub. Co., Advanced Book Program, Menlo Park, CA, 1984).

[38] P. W. Anderson, *More Is Different*, Science **177**, 393 (1972).

[39] A. Eddington, *The Mathematical Theory of Relativity*, Marilee E. Thomas and Robert C. Thomas Science and Related Subjects Collection (The University Press, Cambridge, UK, 1923).

[40] W. Kohn and L. J. Sham, *Self-Consistent Equations Including Exchange and Correlation Effects*, Phys. Rev. **140**, A1133 (1965).

[41] P. Hohenberg and W. Kohn, *Inhomogeneous Electron Gas*, Phys. Rev. **136**, B864 (1964).

[42] C. Freysoldt, B. Grabowski, T. Hickel, J. Neugebauer, G. Kresse, A. Janotti, and C. G. Van de Walle, *First-principles calculations for point defects in solids*, Rev. Mod. Phys. **86**, 253 (2014).

[43] X. Zhang and S.-H. Wei, *Origin of Efficiency Enhancement by Lattice Expansion in Hybrid-Perovskite Solar Cells*, Phys. Rev. Lett. **128**, 136401 (2022).

[44] X. Zhang, J.-X. Shen, M. E. Turiansky, and C. G. Van de Walle, *Hidden role of Bi incorporation in nonradiative recombination in methylammonium lead iodide*, J. Mater. Chem. A **8**, 12964 (2020).

[45] M. E. Turiansky, J.-X. Shen, D. Wickramaratne, and C. G. Van de Walle, *First-principles study of bandgap bowing in BGaN alloys*, J. Appl. Phys. **126**, 095706 (2019).

[46] J.-X. Shen, M. E. Turiansky, D. Wickramaratne, and C. G. Van de Walle, *Thermodynamics of boron incorporation in BGaN*, Phys. Rev. Materials **5**, L030401 (2021).

[47] J. P. Perdew, K. Burke, and M. Ernzerhof, *Generalized Gradient Approximation Made Simple*, Phys. Rev. Lett. **77**, 3865 (1996).

[48] J. P. Perdew, in *AIP Conference Proceedings*, Vol. 577 (AIP, Antwerp (Belgium), 2001) pp. 1–20.

[49] V. Fock, *Näherungsmethode zur Lösung des quantenmechanischen Mehrkörperproblems*, Zeitschrift für Physik **61**, 126 (1930).

[50] J. P. Perdew, *Density functional theory and the band gap problem*, Int. J. Quantum Chem. **28**, 497 (1985).

[51] A. Seidl, A. Görling, P. Vogl, J. A. Majewski, and M. Levy, *Generalized Kohn-Sham schemes and the band-gap problem*, Phys. Rev. B **53**, 3764 (1996).

[52] T. M. Henderson, J. Paier, and G. E. Scuseria, *Accurate treatment of solids with the HSE screened hybrid*, Phys. Status Solidi B **248**, 767 (2011).

[53] P. Mori-Sánchez, A. J. Cohen, and W. Yang, *Localization and Delocalization Errors in Density Functional Theory and Implications for Band-Gap Prediction*, Phys. Rev. Lett. **100**, 146401 (2008).

[54] W. Chen, G. Miceli, G.-M. Rignanese, and A. Pasquarello, *Nonempirical dielectric-dependent hybrid functional with range separation for semiconductors and insulators*, Phys. Rev. Materials **2**, 073803 (2018).

[55] A. Alkauskas, P. Broqvist, and A. Pasquarello, *Defect levels through hybrid density functionals: Insights and applications*, Phys. Status Solidi B **248**, 775 (2011).

[56] P. Liu, C. Franchini, M. Marsman, and G. Kresse, *Assessing model-dielectric-dependent hybrid functionals on the antiferromagnetic transition-metal monoxides MnO, FeO, CoO, and NiO*, J. Phys.: Condens. Matter **32**, 015502 (2020).

[57] G. Cappellini, R. Del Sole, L. Reining, and F. Bechstedt, *Model dielectric function for semiconductors*, Phys. Rev. B **47**, 9892 (1993).

[58] J. P. Perdew, M. Ernzerhof, and K. Burke, *Rationale for mixing exact exchange with density functional approximations*, J. Chem. Phys. **105**, 9982 (1996).

[59] J. E. Moussa, P. A. Schultz, and J. R. Chelikowsky, *Analysis of the Heyd-Scuseria-Ernzerhof density functional parameter space*, J. Chem. Phys. **136**, 204117 (2012).

[60] T. Koopmans, *Über die Zuordnung von Wellenfunktionen und Eigenwerten zu den Einzelnen Elektronen Eines Atoms*, Physica **1**, 104 (1934).

[61] G. Miceli, W. Chen, I. Reshetnyak, and A. Pasquarello, *Nonempirical hybrid functionals for band gaps and polaronic distortions in solids*, Phys. Rev. B **97**, 121112(R) (2018).

[62] D. Wing, G. Ohad, J. B. Haber, M. R. Filip, S. E. Gant, J. B. Neaton, and L. Kronik, *Band gaps of crystalline solids from Wannier-localization–based optimal tuning of a screened range-separated hybrid functional*, Proc. Natl. Acad. Sci. U.S.A. **118**, e2104556118 (2021).

[63] J. Heyd, G. E. Scuseria, and M. Ernzerhof, *Hybrid functionals based on a screened Coulomb potential*, J. Chem. Phys. **118**, 8207 (2003).

[64] J. Heyd, G. E. Scuseria, and M. Ernzerhof, *Erratum: "Hybrid functionals based on a screened Coulomb potential" [J. Chem. Phys. 118, 8207 (2003)]*, J. Chem. Phys. **124**, 219906 (2006).

[65] P. E. Blöchl, *Projector augmented-wave method*, Phys. Rev. B **50**, 17953 (1994).

[66] C. Rostgaard, The Projector Augmented-wave Method (2009), arXiv:0910.1921 .

[67] B. Adolph, J. Furthmüller, and F. Bechstedt, *Optical properties of semiconductors using projector-augmented waves*, Phys. Rev. B **63**, 125108 (2001).

[68] S. T. Pantelides, *The electronic structure of impurities and other point defects in semiconductors*, Rev. Mod. Phys. **50**, 797 (1978).

[69] C. G. Van de Walle and J. Neugebauer, *First-principles calculations for defects and impurities: Applications to III-nitrides*, J. Appl. Phys. **95**, 3851 (2004).

[70] C. Freysoldt, J. Neugebauer, and C. G. Van de Walle, *Fully Ab Initio Finite-Size Corrections for Charged-Defect Supercell Calculations*, Phys. Rev. Lett. **102**, 016402 (2009).

[71] C. Freysoldt, J. Neugebauer, and C. G. Van de Walle, *Electrostatic interactions between charged defects in supercells*, Phys. Status Solidi B **248**, 1067 (2011).

[72] R. O. Jones and O. Gunnarsson, *The density functional formalism, its applications and prospects*, Rev. Mod. Phys. **61**, 689 (1989).

[73] P. A. M. Dirac, *The quantum theory of the emission and absorption of radiation*, Proc. R. Soc. London A. **114**, 243 (1927).

[74] E. Fermi, *Nuclear Physics* (Univ. of Chicago Press, Chicago, IL, 1974).

[75] R. Pässler, *Relationships between the nonradiative multiphonon carrier-capture properties of deep charged and neutral centres in semiconductors*, Phys. Status Solidi B **78**, 625 (1976).

[76] C. E. Dreyer, A. Alkauskas, J. L. Lyons, and C. G. Van de Walle, *Radiative capture rates at deep defects from electronic structure calculations*, Phys. Rev. B **102**, 085305 (2020).

[77] B. K. Ridley, *Quantum Processes in Semiconductors*, 4th ed. (Oxford University Press, Oxford, UK, 1999).

[78] L. Razinkovas, M. Maciaszek, F. Reinhard, M. W. Doherty, and A. Alkauskas, *Photoionization of negatively charged NV centers in diamond: Theory and* ab initio *calculations*, Phys. Rev. B **104**, 235301 (2021).

[79] A. M. Stoneham, *Theory of defects in solids: electronic structure of defects in insulators and semiconductors* (Clarendon Press, Oxford, UK, 1975).

[80] D. V. Lang, *Deep-level transient spectroscopy: A new method to characterize traps in semiconductors*, J. Appl. Phys. **45**, 3023 (1974).

[81] D. Wickramaratne, C. E. Dreyer, B. Monserrat, J.-X. Shen, J. L. Lyons, A. Alkauskas, and C. G. Van de Walle, *Defect identification based on first-principles calculations for deep level transient spectroscopy*, Appl. Phys. Lett. **113**, 192106 (2018).

[82] F. Zhao, M. E. Turiansky, and C. G. Van de Walle, *Impurity Auger from first principles* (2022), unpublished.

[83] A. Alkauskas, J. L. Lyons, D. Steiauf, and C. G. Van de Walle, *First-Principles Calculations of Luminescence Spectrum Line Shapes for Defects in Semiconductors: The Example of GaN and ZnO*, Phys. Rev. Lett. **109**, 267401 (2012).

[84] G. Thiering and A. Gali, *Ab initio calculation of spin-orbit coupling for an NV center in diamond exhibiting dynamic Jahn-Teller effect*, Phys. Rev. B **96**, 081115 (2017).

[85] T. J. Smart, K. Li, J. Xu, and Y. Ping, *Intersystem crossing and exciton–defect coupling of spin defects in hexagonal boron nitride*, npj Comput. Mater. **7**, 1 (2021).

[86] D. Manzano, *A short introduction to the Lindblad Master Equation*, AIP Adv. **10**, 025106 (2020).

[87] L. Novotny and B. Hecht, *Principles of nano-optics*, 2nd ed. (Cambridge University Press, Cambridge, UK, 2012).

[88] A. L. Exarhos, D. A. Hopper, R. N. Patel, M. W. Doherty, and L. C. Bassett, *Magnetic-field-dependent quantum emission in hexagonal boron nitride at room temperature*, Nat. Commun. **10**, 222 (2019).

[89] R. E. K. Fishman, R. N. Patel, D. A. Hopper, T.-Y. Huang, and L. C. Bassett, Photon emission correlation spectroscopy as an analytical tool for quantum defects (2021), arXiv:2111.01252 .

[90] V. Abakumov, V. I. Perel, and I. Yassievich, *Nonradiative recombination in semiconductors*, Vol. 33 (Elsevier, Amsterdam, 1991).

[91] K. Huang, A. Rhys, and N. F. Mott, *Theory of light absorption and non-radiative transitions in F-centres*, Proc. Royal Soc. Lon. A **204**, 406 (1950).

[92] R. Kubo and Y. Toyozawa, *Application of the method of generating function to radiative and non-radiative transitions of a trapped electron in a crystal*, Prog. Theor. Phys. **13**, 160 (1955).

[93] R. Pässler, *Calculation of nonradiative multiphonon capture coefficients and ionization rates for neutral centres according to the static coupling scheme: I. Theory*, Phys. Status Solidi B **68**, 69 (1975).

[94] C. H. Henry and D. V. Lang, *Nonradiative capture and recombination by multiphonon emission in GaAs and GaP*, Phys. Rev. B **15**, 989 (1977).

[95] A. M. Stoneham, *Non-radiative transitions in semiconductors*, Rep. Prog. Phys. **44**, 1251 (1981).

[96] D. Wickramaratne, J.-X. Shen, C. E. Dreyer, M. Engel, M. Marsman, G. Kresse, S. Marcinkevičius, A. Alkauskas, and C. G. Van de Walle, *Iron as a source of efficient Shockley-Read-Hall recombination in GaN*, Appl. Phys. Lett. **109**, 162107 (2016).

[97] D. Wickramaratne, J.-X. Shen, A. Alkauskas, and C. G. Van de Walle, *Comment on "Comparative study of ab initio nonradiative recombination rate calculations under different formalisms"*, Phys. Rev. B **97**, 077301 (2018).

[98] L. Shi, K. Xu, and L.-W. Wang, *Comparative study of ab initio nonradiative recombination rate calculations under different formalisms*, Phys. Rev. B **91**, 205315 (2015).

[99] T. E. Oliphant, *A guide to NumPy*, Vol. 1 (Trelgol Publishing USA, 2006).

[100] E. Jones, T. Oliphant, P. Peterson, and others, *SciPy: Open source scientific tools for Python* (2001).

[101] S. P. Ong, W. D. Richards, A. Jain, G. Hautier, M. Kocher, S. Cholia, D. Gunter, V. L. Chevrier, K. A. Persson, and G. Ceder, *Python Materials Genomics (pymatgen): A robust, open-source python library for materials analysis*, Comput. Mater. Sci. **68**, 314 (2013).

[102] B. P. Zapol, *New expressions for the overlap integral of two linear harmonic oscillator wavefunctions*, Chem. Phys. Lett. **93**, 549 (1982).

[103] L. Chaput, A. Togo, and I. Tanaka, *Finite-displacement computation of the electron-phonon interaction within the projector augmented-wave method*, Phys. Rev. B **100**, 174304 (2019).

[104] M. Engel, M. Marsman, C. Franchini, and G. Kresse, *Electron-phonon interactions using the projector augmented-wave method and Wannier functions*, Phys. Rev. B **101**, 184302 (2020).

[105] G. D. Barmparis, Y. S. Puzyrev, X.-G. Zhang, and S. T. Pantelides, *Theory of inelastic multiphonon scattering and carrier capture by defects in semiconductors: application to capture cross sections*, Phys. Rev. B **92**, 214111 (2015).

[106] A. Alkauskas, M. D. McCluskey, and C. G. Van de Walle, *Tutorial: Defects in semiconductors—combining experiment and theory*, J. Appl. Phys. **119**, 181101 (2016).

[107] B. Di Bartolo and X. Chen, eds., *Advances in nonradiative processes in solids*, Vol. 249 (Plenum Press, New York, NY, 1991).

[108] T. Kluyver, B. Ragan-Kelley, F. Pérez, B. Granger, M. Bussonnier, J. Frederic, K. Kelley, J. Hamrick, J. Grout, S. Corlay, P. Ivanov, D. Avila, S. Abdalla, and C. Willing, in *Positioning and Power in Academic Publishing: Players, Agents and Agendas*, edited by F. Loizides and B. Schmidt (IOS Press, 2016) pp. 87–90.

[109] G. Kresse and J. Furthmüller, *Efficient iterative schemes for ab initio total-energy calculations using a plane-wave basis set*, Phys. Rev. B **54**, 11169 (1996).

[110] H. Schulz and K. H. Thiemann, *Crystal structure refinement of AlN and GaN*, Solid State Commun. **23**, 815 (1977).

[111] I. Vurgaftman and J. R. Meyer, *Band parameters for nitrogen-containing semiconductors*, J. Appl. Phys. **94**, 3675 (2003).

[112] A. Baldereschi, *Mean-value point in the Brillouin zone*, Phys. Rev. B **7**, 5212 (1973).

[113] J. Tsao, S. Chowdhury, M. Hollis, D. Jena, N. Johnson, K. Jones, R. Kaplar, S. Rajan, C. G. Van de Walle, E. Bellotti, *et al.*, *Ultrawide-bandgap semiconductors: Research opportunities and challenges*, Adv. Electron. Mater. **4**, 1600501 (2018).

[114] D. Jena, R. Page, J. Casamento, P. Dang, J. Singhal, Z. Zhang, J. Wright, G. Khalsa, Y. Cho, and H. G. Xing, *The new nitrides: Layered, ferroelectric, magnetic, metallic and superconducting nitrides to boost the gan photonics and electronics eco-system*, Jpn. J. Appl. Phys. **58**, SC0801 (2019).

[115] X. W. Zhang, *Doping and electrical properties of cubic boron nitride thin films: A critical review*, Thin Solid Films **544**, 2 (2013).

[116] H. Murata, T. Taniguchi, S. Hishita, T. Yamamoto, F. Oba, and I. Tanaka, *Local environment of silicon in cubic boron nitride*, J. Appl. Phys. **114**, 233502 (2013).

[117] T. Taniguchi, T. Teraji, S. Koizumi, K. Watanabe, and S. Yamaoka, *Appearance of n-type semiconducting properties of cbn single crystals grown at high pressure*, Jpn. J. Appl. Phys. **41**, L109 (2002).

[118] K. Hirama, Y. Taniyasu, H. Yamamoto, and K. Kumakura, *Control of n-type electrical conductivity for cubic boron nitride (c-bn) epitaxial layers by si doping*, Appl. Phys. Lett. **116**, 162104 (2020).

[119] H. Yin, H.-G. Boyen, P. Ziemann, B. Dohuard, L. Houssiau, F. Renaux, M. Hecq, and C. Bittencourt, *Purity of epitaxial cubic boronnitride films on (001) diamond—a prerequisite for their doping*, Diam. Relat. Mater. **17**, 276 (2008).

[120] W. J. Zhang, Y. M. Chong, I. Bello, and S. T. Lee, *Nucleation, growth and characterization of cubic boron nitride (cBN) films*, J. Phys. D: Appl. Phys. **40**, 6159 (2007).

[121] R. H. Wentorf, *Preparation of Semiconducting Cubic Boron Nitride*, J. Chem. Phys. **36**, 1990 (1962).

[122] D. J. Chadi and K. J. Chang, *Theory of the Atomic and Electronic Structure of dx Centers in GaAs and $Al_xGa_{1-x}As$ Alloys*, Phys. Rev. Lett. **61**, 873 (1988).

[123] Y. B. Li, H. X. Jiang, G. Z. Yuan, A. L. Chen, X. Wang, T. G. Dai, and H. S. Yang, *Electronic structure and impurity states of S-doped cBN: A first-principle study*, J. Alloys Compd. **531**, 82 (2012).

[124] T. Mosuang and J. Lowther, *Influence of defects on the h- bn to c- bn transformation*, Phys. Rev. B **66**, 014112 (2002).

[125] V. Gubanov, E. Pentaleri, C. Fong, and B. Klein, *Electronic structure of defects and impurities in iii-v nitrides. ii. be, mg, and si in cubic boron nitride*, Phys. Rev. B **56**, 13077 (1997).

[126] C. Park and D. Chadi, *Stability of deep donor and acceptor centers in gan, aln, and bn*, Phys. Rev. B **55**, 12995 (1997).

[127] W. Orellana and H. Chacham, *Energetics of carbon and oxygen impurities and their interaction with vacancies in cubic boron nitride*, Phys. Rev. B **62**, 10135 (2000).

[128] D. A. Evans, A. G. McGlynn, B. M. Towlson, M. Gunn, D. Jones, T. E. Jenkins, R. Winter, and N. R. J. Poolton, *Determination of the optical band-gap energy of cubic and hexagonal boron nitride using luminescence excitation spectroscopy*, J. Phys.: Condens. Matter **20**, 075233 (2008).

[129] T. Sōma, A. Sawaoka, and S. Saito, *Characterization of wurtzite type boron nitride synthesized by shock compression*, Mater. Res. Bull. **9**, 755 (1974).

[130] C. E. Dreyer, J. L. Lyons, A. Janotti, and C. G. Van de Walle, *Band alignments and polarization properties of BN polymorphs*, Appl. Phys. Express **7**, 031001 (2014).

[131] G. Henkelman, B. P. Uberuaga, and H. Jónsson, *A climbing image nudged elastic band method for finding saddle points and minimum energy paths*, J. Chem. Phys. **113**, 9901 (2000).

[132] C. H. Park and D. J. Chadi, *Orthorhombic symmetry dx centers in s-doped gasb, gaas, and* $al_xga_{1-x}as$, Phys. Rev. B **54**, R14246(R) (1996).

[133] L. Gordon, J. L. Lyons, A. Janotti, and C. G. Van de Walle, *Hybrid functional calculations of dx centers in aln and gan*, Phys. Rev. B **89**, 085204 (2014).

[134] J. S. Harris, B. E. Gaddy, R. Collazo, Z. Sitar, and D. L. Irving, *Oxygen and silicon point defects in Al 0.65 Ga 0.35 N*, Phys. Rev. Mater. **3**, 054604 (2019).

[135] D. J. Chadi and K. J. Chang, *Energetics of DX -center formation in GaAs and* $Al_xGa_{1-x}As$ *alloys*, Phys. Rev. B **39**, 10063 (1989).

[136] M. D. McCluskey and E. E. Haller, *Dopants and defects in semiconductors*, 2nd ed. (CRC Press, Taylor & Francis Group, Boca Raton, FL, 2018).

[137] M. E. Levinshteĭn, S. L. Rumyantsev, and M. Shur, eds., *Properties of advanced semiconductor materials: GaN, AlN, InN, BN, SiC, SiGe* (Wiley, New York, NY, 2001).

[138] L. Weston, D. Wickramaratne, M. Mackoit, A. Alkauskas, and C. G. Van de Walle, *Native point defects and impurities in hexagonal boron nitride*, Phys. Rev. B **97**, 214104 (2018).

[139] W. Orellana and H. Chacham, *Atomic geometry and energetics of native defects in cubic boron nitride*, Braz. J. Phys. **29**, 801 (1999).

[140] G. H. Vineyard, *Frequency factors and isotope effects in solid state rate processes*, J. Phys. Chem. Solids **3**, 121 (1957).

[141] Y. K. Le and H. Oechsner, *On the influence of substrate temperature for cubic boron nitride growth*, Thin Solid Films **437**, 83 (2003).

[142] T. A. Abtew, W. Gao, X. Gao, Y. Y. Sun, S. B. Zhang, and P. Zhang, *Theory of Oxygen-Boron Vacancy Defect in Cubic Boron Nitride: A Diamond nv− Isoelectronic Center*, Phys. Rev. Lett. **113**, 136401 (2014).

[143] G. Cassabois, P. Valvin, and B. Gil, *Hexagonal boron nitride is an indirect bandgap semiconductor*, Nat. Photonics **10**, 262 (2016).

[144] N. Kostoglou, K. Polychronopoulou, and C. Rebholz, *Thermal and chemical stability of hexagonal boron nitride (h-BN) nanoplatelets*, Vacuum **112**, 42 (2015).

[145] Y. Kubota, K. Watanabe, O. Tsuda, and T. Taniguchi, *Deep Ultraviolet Light-Emitting Hexagonal Boron Nitride Synthesized at Atmospheric Pressure*, Science **317**, 932 (2007).

[146] K. Watanabe, T. Taniguchi, T. Niiyama, K. Miya, and M. Taniguchi, *Far-ultraviolet plane-emission handheld device based on hexagonal boron nitride*, Nat. Photonics **3**, 591 (2009).

[147] M. Mackoit-Sinkevičienė, M. Maciaszek, C. G. Van de Walle, and A. Alkauskas, *Carbon dimer defect as a source of the 4.1 eV luminescence in hexagonal boron nitride*, Appl. Phys. Lett. **115**, 212101 (2019).

[148] T. T. Tran, C. Elbadawi, D. Totonjian, C. J. Lobo, G. Grosso, H. Moon, D. R. Englund, M. J. Ford, I. Aharonovich, and M. Toth, *Robust Multicolor Single Photon Emission from Point Defects in Hexagonal Boron Nitride*, ACS Nano **10**, 7331 (2016).

[149] A. L. Exarhos, D. A. Hopper, R. R. Grote, A. Alkauskas, and L. C. Bassett, *Optical Signatures of Quantum Emitters in Suspended Hexagonal Boron Nitride*, ACS Nano **11**, 3328 (2017).

[150] S. Choi, T. T. Tran, C. Elbadawi, C. Lobo, X. Wang, S. Juodkazis, G. Seniutinas, M. Toth, and I. Aharonovich, *Engineering and Localization of Quantum Emitters in Large Hexagonal Boron Nitride Layers*, ACS Appl. Mater. Interfaces **8**, 29642 (2016).

[151] N. Mendelson, Z.-Q. Xu, T. T. Tran, M. Kianinia, J. Scott, C. Bradac, I. Aharonovich, and M. Toth, *Engineering and tuning of quantum emitters in few-layer hexagonal boron nitride*, ACS Nano **13**, 3132 (2019).

[152] M. Abdi, J.-P. Chou, A. Gali, and M. B. Plenio, *Color centers in hexagonal boron nitride monolayers: A group theory and ab-initio analysis*, ACS Photonics **5**, 1967 (2018).

[153] V. Ivády, G. Barcza, G. o. Thiering, S. Li, H. Hamdi, J.-P. Chou, O. Legeza, and A. Gali, *Ab initio theory of the negatively charged boron vacancy qubit in hexagonal boron nitride*, npj Comput. Mater. **6**, 1 (2020).

[154] A. Gottscholl, M. Kianinia, V. Soltamov, S. Orlinskii, G. Mamin, C. Bradac, C. Kasper, K. Krambrock, A. Sperlich, M. Toth, I. Aharonovich, and V. Dyakonov, *Initialization and read-out of intrinsic spin defects in a van der Waals crystal at room temperature*, Nat. Mater. **19**, 540 (2020).

[155] T. T. Tran, K. Bray, M. J. Ford, M. Toth, and I. Aharonovich, *Quantum emission from hexagonal boron nitride monolayers*, Nat. Nanotechnol. **11**, 37 (2016).

[156] S. Li, J.-P. Chou, A. Hu, M. B. Plenio, P. Udvarhelyi, G. Thiering, M. Abdi, and A. Gali, *Giant shift upon strain on the fluorescence spectrum of VNNB color centers in h-BN*, npj Quantum Inf. **6**, 1 (2020).

[157] S. A. Tawfik, S. Ali, M. Fronzi, M. Kianinia, T. T. Tran, C. Stampfl, I. Aharonovich, M. Toth, and M. J. Ford, *First-principles investigation of quantum emission from hBN defects*, Nanoscale **9**, 13575 (2017).

[158] G. D. Cheng, Y. G. Zhang, L. Yan, H. F. Huang, Q. Huang, Y. X. Song, Y. Chen, and Z. Tang, *A paramagnetic neutral CBVN center in hexagonal boron nitride monolayer for spin qubit application*, Comput. Mater. Sci. **129**, 247 (2017).

[159] F. Wu, A. Galatas, R. Sundararaman, D. Rocca, and Y. Ping, *First-principles engineering of charged defects for two-dimensional quantum technologies*, Phys. Rev. Mater. **1**, 071001 (2017).

[160] Z.-Q. Xu, C. Elbadawi, T. T. Tran, M. Kianinia, X. Li, D. Liu, T. B. Hoffman, M. Nguyen, S. Kim, J. H. Edgar, X. Wu, L. Song, S. Ali, M. Ford, M. Toth, and I. Aharonovich, *Single photon emission from plasma treated 2d hexagonal boron nitride*, Nanoscale **10**, 7957 (2018).

[161] N. Chejanovsky, M. Rezai, F. Paolucci, Y. Kim, T. Rendler, W. Rouabeh, F. Fávaro de Oliveira, P. Herlinger, A. Denisenko, S. Yang, I. Gerhardt, A. Finkler, J. H. Smet, and J. Wrachtrup, *Structural Attributes and Photodynamics of Visible Spectrum Quantum Emitters in Hexagonal Boron Nitride*, Nano Lett. **16**, 7037 (2016).

[162] C. R. Helms and E. H. Poindexter, *The silicon-silicon dioxide system: Its microstructure and imperfections*, Rep. Prog. Phys. **57**, 791 (1994).

[163] J. R. Weber, A. Janotti, P. Rinke, and C. G. Van de Walle, *Dangling-bond defects and hydrogen passivation in germanium*, Appl. Phys. Lett. **91**, 142101 (2007).

[164] M. Choi, A. Janotti, and C. G. Van de Walle, *Native point defects and dangling bonds in α-al2o3*, J. Appl. Phys. **113**, 044501 (2013).

[165] C. Jin, F. Lin, K. Suenaga, and S. Iijima, *Fabrication of a Freestanding Boron Nitride Single Layer and Its Defect Assignments*, Phys. Rev. Lett. **102**, 195505 (2009).

[166] N. Alem, R. Erni, C. Kisielowski, M. D. Rossell, W. Gannett, and A. Zettl, *Atomically thin hexagonal boron nitride probed by ultrahigh-resolution transmission electron microscopy*, Phys. Rev. B **80**, 155425 (2009).

[167] J. Kotakoski, C. H. Jin, O. Lehtinen, K. Suenaga, and A. V. Krasheninnikov, *Electron knock-on damage in hexagonal boron nitride monolayers*, Phys. Rev. B **82**, 113404 (2010).

[168] F. Hayee, L. Yu, J. L. Zhang, C. J. Ciccarino, M. Nguyen, A. F. Marshall, I. Aharonovich, J. Vučković, P. Narang, T. F. Heinz, and J. A. Dionne, *Revealing multiple classes of stable quantum emitters in hexagonal boron nitride with correlated optical and electron microscopy*, Nat. Mater. **19**, 534 (2020).

[169] N. R. Jungwirth and G. D. Fuchs, *Optical Absorption and Emission Mechanisms of Single Defects in Hexagonal Boron Nitride*, Phys. Rev. Lett. **119**, 057401 (2017).

[170] S. Grimme, J. Antony, S. Ehrlich, and H. Krieg, *A consistent and accurate ab initio*

parametrization of density functional dispersion correction (DFT-D) for the 94 elements H-Pu, J. Chem. Phys. **132**, 154104 (2010).

[171] D. Wickramaratne, L. Weston, and C. G. Van de Walle, *Monolayer to Bulk Properties of Hexagonal Boron Nitride*, J. Phys. Chem. C **122**, 25524 (2018).

[172] G. Antonius, S. Poncé, E. Lantagne-Hurtubise, G. Auclair, X. Gonze, and M. Côté, *Dynamical and anharmonic effects on the electron-phonon coupling and the zero-point renormalization of the electronic structure*, Phys. Rev. B **92**, 085137 (2015).

[173] R. Tutchton, C. Marchbanks, and Z. Wu, *Structural impact on the eigenenergy renormalization for carbon and silicon allotropes and boron nitride polymorphs*, Phys. Rev. B **97**, 205104 (2018).

[174] Y. Gu, M. Zheng, Y. Liu, and Z. Xu, *Low-Temperature Synthesis and Growth of Hexagonal Boron-Nitride in a Lithium Bromide Melt*, J. Am. Ceram. Soc. **90**, 1589 (2007).

[175] C. G. Van de Walle and R. A. Street, *Structure, energetics, and dissociation of Si-H bonds at dangling bonds in silicon*, Phys. Rev. B **49**, 14766 (1994).

[176] T. Taniguchi and K. Watanabe, *Synthesis of high-purity boron nitride single crystals under high pressure by using Ba–BN solvent*, J. Cryst. Growth **303**, 525 (2007).

[177] G. Noh, D. Choi, J.-H. Kim, D.-G. Im, Y.-H. Kim, H. Seo, and J. Lee, *Stark Tuning of Single-Photon Emitters in Hexagonal Boron Nitride*, Nano Lett. **18**, 4710 (2018).

[178] N. V. Proscia, Z. Shotan, H. Jayakumar, P. Reddy, C. Cohen, M. Dollar, A. Alkauskas, M. Doherty, C. A. Meriles, and V. M. Menon, *Near-deterministic activa-*

tion of room-temperature quantum emitters in hexagonal boron nitride, Optica **5**, 1128 (2018).

[179] T. Brumme, M. Calandra, and F. Mauri, *Electrochemical doping of few-layer ZrNCl from first principles: Electronic and structural properties in field-effect configuration*, Phys. Rev. B **89**, 245406 (2014).

[180] N. A. Richter, S. Sicolo, S. V. Levchenko, J. Sauer, and M. Scheffler, *Concentration of vacancies at metal-oxide surfaces: case study of MgO(100)*, Phys. Rev. Lett. **111**, 045502 (2013).

[181] N. R. Jungwirth, B. Calderon, Y. Ji, M. G. Spencer, M. E. Flatté, and G. D. Fuchs, *Temperature dependence of wavelength selectable zero-phonon emission from single defects in hexagonal boron nitride*, Nano Lett. **16**, 6052 (2016).

[182] G. Cappellini, G. Satta, M. Palummo, and G. Onida, *Optical properties of BN in cubic and layered hexagonal phases*, Phys. Rev. B **64**, 035104 (2001).

[183] W. Liu, Y.-T. Wang, Z.-P. Li, S. Yu, Z.-J. Ke, Y. Meng, J.-S. Tang, C.-F. Li, and G.-C. Guo, *An ultrastable and robust single-photon emitter in hexagonal boron nitride*, Physica E Low Dimens. Sys. Nanostruct. **124**, 114251 (2020).

[184] N. Chandra and H. Prakash, *Anticorrelation in two-photon attenuated laser beam*, Phys. Rev. A **1**, 1696 (1970).

[185] X. Li, R. A. Scully, K. Shayan, Y. Luo, and S. Strauf, *near-unity light collection efficiency from quantum emitters in boron nitride by coupling to metallo-dielectric antennas*, ACS Nano **13**, 6992 (2019).

[186] D. Yim, M. Yu, G. Noh, J. Lee, and H. Seo, *Polarization and localization of single-photon emitters in hexagonal boron nitride wrinkles*, ACS Appl. Mater. Interfaces **12**, 36362 (2020).

[187] Z.-Q. Xu, N. Mendelson, J. A. Scott, C. Li, I. H. Abidi, H. Liu, Z. Luo, I. Aharonovich, and M. Toth, *Charge and energy transfer of quantum emitters in 2D heterostructures*, 2D Mater. **7**, 031001 (2020).

[188] P. Khatri, A. J. Ramsay, R. N. E. Malein, H. M. Chong, and I. J. Luxmoore, *Optical Gating of Photoluminescence from Color Centers in Hexagonal Boron Nitride*, Nano Lett. **20**, 4256 (2020).

[189] D. Kozawa, A. G. Rajan, S. X. Li, T. Ichihara, V. B. Koman, Y. Zeng, M. Kuehne, S. K. Iyemperumal, K. S. Silmore, D. Parviz, P. Liu, A. T. Liu, S. Faucher, Z. Yuan, W. Xu, J. H. Warner, D. Blankschtein, and M. S. Strano, Observation and spectral assignment of a family of hexagonal boron nitride lattice defects (2019), arXiv:1909.11738 .

[190] H. Takashima, H. Maruya, K. Ishihara, T. Tashima, K. Shimazaki, A. W. Schell, T. T. Tran, I. Aharonovich, and S. Takeuchi, *Determination of the dipole orientation of single defects in hexagonal boron nitride*, ACS Photonics **7**, 2056 (2020).

[191] P. K. Jha, H. Akbari, Y. Kim, S. Biswas, and H. A. Atwater, *Nanoscale axial position and orientation measurement of hexagonal boron nitride quantum emitters using a tunable nanophotonic environment*, Nanotechnology **33**, 015001 (2022).

[192] N. Mendelson, D. Chugh, J. R. Reimers, T. S. Cheng, A. Gottscholl, H. Long, C. J. Mellor, A. Zettl, V. Dyakonov, P. H. Beton, S. V. Novikov, C. Jagadish, H. H. Tan, M. J. Ford, M. Toth, C. Bradac, and I. Aharonovich, *Identifying carbon as the*

source of visible single-photon emission from hexagonal boron nitride, Nat. Mater. **20**, 321 (2020).

[193] L. J. Martinez, T. Pelini, V. Waselowski, J. R. Maze, B. Gil, G. Cassabois, and V. Jacques, *Efficient single photon emission from a high-purity hexagonal boron nitride crystal*, Phys. Rev. B **94**, 121405(R) (2016).

[194] B. Sontheimer, M. Braun, N. Nikolay, N. Sadzak, I. Aharonovich, and O. Benson, *Photodynamics of quantum emitters in hexagonal boron nitride revealed by low-temperature spectroscopy*, Phys. Rev. B **96**, 121202(R) (2017).

[195] M. K. Boll, I. P. Radko, A. Huck, and U. L. Andersen, *Photophysics of quantum emitters in hexagonal boron-nitride nano-flakes*, Opt. Express **28**, 7475 (2020).

[196] H. L. Stern, Q. Gu, J. Jarman, S. Eizagirre Barker, N. Mendelson, D. Chugh, S. Schott, H. H. Tan, H. Sirringhaus, I. Aharonovich, and M. Atatüre, *Room-temperature optically detected magnetic resonance of single defects in hexagonal boron nitride*, Nat. Commun. **13**, 618 (2022).

[197] M. W. Doherty, N. B. Manson, P. Delaney, F. Jelezko, J. Wrachtrup, and L. C. L. Hollenberg, *The nitrogen-vacancy colour centre in diamond*, Phys. Rep. **528**, 1 (2013).

[198] E. Neu, M. Agio, and C. Becher, *Photophysics of single silicon vacancycentersin diamond: implications forsingle photon emission*, Opt. Express **20**, 19956 (2012).

[199] A. Sajid and K. S. Thygesen, *VNCB defect as source of single photon emission from hexagonal boron nitride*, 2D Mater. **7**, 031007 (2020).

[200] Q. Yan, E. Kioupakis, D. Jena, and C. G. Van de Walle, *First-principles study of*

high-field-related electronic behavior of group-III nitrides, Phys. Rev. B **90**, 121201(R) (2014).